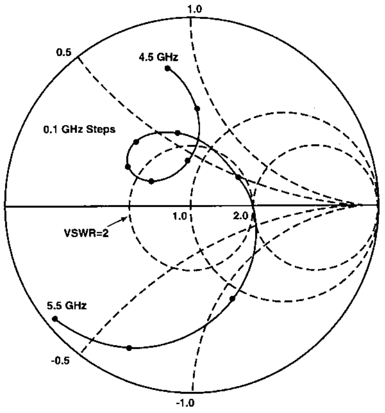

Applied Computational Electromagnetics Society Journal

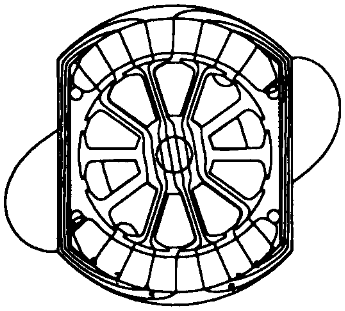

Editor-in-Chief
Atef Z. Elsherbeni

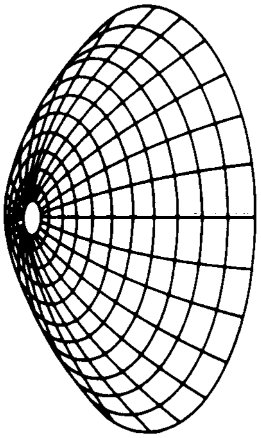

March 2004
Vol. 19 No. 1a
ISSN 1054-4887

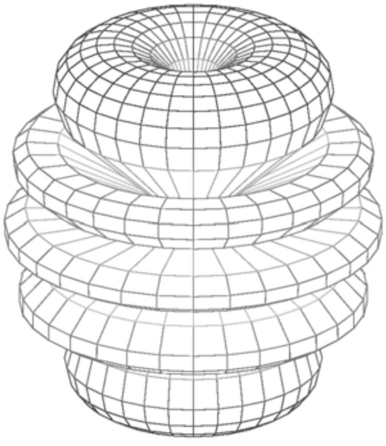

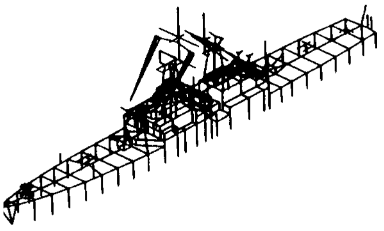

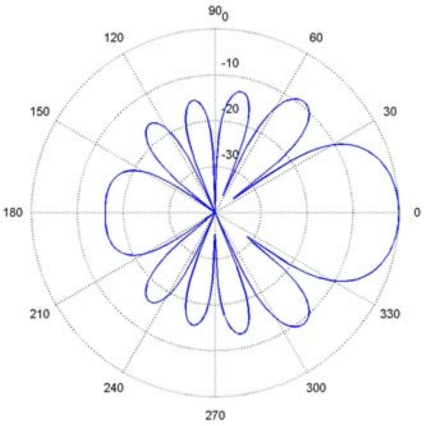

GENERAL PURPOSE AND SCOPE: The Applied Computational Electromagnetics Society ***(ACES)*** Journal hereinafter known as the ***ACES Journal*** is devoted to the exchange of information in computational electromagnetics, to the advancement of the state-of-the art, and the promotion of related technical activities. A primary objective of the information exchange is the elimination of the need to "re-invent the wheel" to solve a previously-solved computational problem in electrical engineering, physics, or related fields of study. The technical activities promoted by this publication include code validation, performance analysis, and input/output standardization; code or technique optimization and error minimization; innovations in solution technique or in data input/output; identification of new applications for electromagnetics modeling codes and techniques; integration of computational electromagnetics techniques with new computer architectures; and correlation of computational parameters with physical mechanisms.

SUBMISSIONS: The ***ACES Journal*** welcomes original, previously unpublished papers, related to applied computational electromagnetics. Typical papers will represent the computational electromagnetics aspects of research in electrical engineering, physics, or related disciplines. However, papers which represent research in applied computational electromagnetics itself are equally acceptable.

Manuscripts are to be submitted through the upload system of ***ACES*** web site http://aces.ee.olemiss.edu See "Information for Authors" on inside of back cover and at ***ACES*** web site. For additional information contact the Editor-in-Chief:

Dr. Atef Elsherbeni
Department of Electrical Engineering
The University of Mississippi
University, MS 386377 USA
Phone: 662-915-5382 Fax: 662-915-7231
Email: atef@olemis.edu

SUBSCRIPTIONS: All members of the Applied Computational Electromagnetics Society who have paid their subscription fees are entitled to receive the ***ACES Journal*** with a minimum of three issues per calendar year and are entitled to download any published journal article available at http://aces.ee.olemiss.edu.

Back issues, when available, are $15 each. Subscriptions to ***ACES*** is through the web site. Orders for back issues of the ***ACES Journal*** and changes of addresses should be sent directly to ***ACES*** Executive Officer:

Dr. Richard W. Adler
ECE Department, Code ECAB
Naval Postgraduate School
833 Dyer Road, Room 437
Monterey, CA 93943-5121 USA
Fax: 831-649-0300
Email: *rwa@attglobal.net*

Allow four week's advance notice for change of address. Claims for missing issues will not be honored because of insufficient notice or address change or loss in mail unless the Executive Officer is notified within 60 days for USA and Canadian subscribers or 90 days for subscribers in other countries, from the last day of the month of publication. For information regarding reprints of individual papers or other materials, see "Information for Authors".

LIABILITY. Neither ***ACES***, nor the ***ACES Journal*** editors, are responsible for any consequence of misinformation or claims, express or implied, in any published material in an ***ACES Journal*** issue. This also applies to advertising, for which only camera-ready copies are accepted. Authors are responsible for information contained in their papers. If any material submitted for publication includes material which has already been published elsewhere, it is the author's responsibility to obtain written permission to reproduce such material.

APPLIED COMPUTATIONAL ELECTROMAGNETICS SOCIETY JOURNAL

Editor-in-Chief
Atef Z. Elsherbeni

March 2004
Vol. 19 No. 1a
ISSN 1054-4887

The ACES Journal is abstracted in INSPEC, in Engineering Index, DTIC, Science Citation Index Expanded, the Research Alert, and to Current Contents/Engineering, Computing & Technology.

The first, fourth, and sixth illustrations on the front cover have been obtained from the Department of Electrical Engineering at the University of Mississippi.

The third and fifth illustrations on the front cover have been obtained from Lawrence Livermore National Laboratory.

The second illustration on the front cover has been obtained from FLUX2D software, CEDRAT S.S. France, MAGSOFT Corporation, New York.

THE APPLIED COMPUTATIONAL ELECTROMAGNETICS SOCIETY
http//:aces.ee.olemiss.edu

ACES JOURNAL EDITORS

EDITOR-IN-CHIEF/ACES/JOURNAL
Atef Elsherbeni
University of Mississippi, EE Dept.
University, MS 38677, USA

ASSOCIATE EDITOR-IN-CHIEF
Alexander Yakovlev
University of Mississippi, EE Dept.
University, MS 38677, USA

MANAGING EDITOR
Richard W. Adler
833 Dyer Rd, Rm 437 EC/AB
NPS, Monterey, CA 93943-5121, USA

EDITORIAL ASSISTANT
Matthew J. Inman
University of Mississippi, EE Dept.
University, MS 38677, USA

EDITOR-IN-CHIEF, EMERITUS
Ducan C. Baker
EE Dept. U. of Pretoria
0002 Pretoria, South Africa

EDITOR-IN-CHIEF, EMERITUS
Robert M. Bevensee
Box 812
Alamo, CA 94507-0516, USA

EDITOR-IN-CHIEF, EMERITUS
David E. Stein
USAF Scientific Advisory Board
Washington, DC 20330, USA

EDITOR-IN-CHIEF, EMERITUS
Allen Glisson
University of Mississippi, EE Dept.
University, MS 38677, USA

EDITOR-IN-CHIEF, EMERITUS
Ahmed Kishk
University of Mississippi, EE Dept.
University, MS 38677, USA

ACES JOURNAL ASSOCIATE EDITORS

Giandomenico Amendola
Universita' della Calabria
Rende , Italy

John Beggs
NASA Langley Research Center
Hampton, VA, USA

John Brauer
Ansoft Corporation
Milwaukee, WI, USA

Magda El-Shenawee
University of Arkansas
Fayetteville AR, USA

Pat Foster
Microwave & Antenna Systems
Gt. Malvern, Worc. UK

Cynthia M. Furse
Utah State University
Logan UT, USA

Christian Hafner
Swiss Federal Inst. of Technology
Zurich, Switzerland

Michael Hamid
University of South Alabama,
Mobile, AL, USA

Andy Harrison
Radiance
Huntsville, AL

Chun-Wen Paul Huang
Anadigics, Inc.
Warren, NJ, USA

Todd H. Hubing
University of Missouri-Rolla
Rolla, MO, USA

Nathan Ida
The University of Akron
Akron, OH, USA

Yasushi Kanai
Niigata Institute of Technology
Kashiwazaki, Japan

Leo C. Kempel
Michigan State University
East Lansing MI, USA

Andrzej Krawczyk
Institute of Electrical Engineering
Warszawa, Poland

Stanley Kubina
Concordia University
Montreal, Quebec, Canada

Samir F. Mahmoud
Kuwait University
Safat, Kuwait

Ronald Marhefka
Ohio State University
Columbus, OH, USA

Edmund K. Miller
LASL
Santa Fe, NM, USA

Krishna Naishadham
Wright State University
Dayton, OH, USA

Giuseppe Pelosi
University of Florence
Florence, Italy

Vicente Rodriguez
ETS-Lindgren
Cedar Park, TX, USA

Harold A. Sabbagh
Sabbagh Associates
Bloomington, IN, USA

John B. Schneider
Washington State University
Pullman, WA, USA

Abdel Razek Sebak
University of Manitoba
Winnipeg, MB, Canada

Amr M. Sharawee
American University
Cairo, Egypt

Norio Takahashi
Okayama University
Tsushima, Japan

THE APPLIED COMPUTATIONAL ELECTROMAGNETICS SOCIETY

JOURNAL

Vol. 19 No. 1a March 2004

TABLE OF CONTENTS

Reflection compensation scheme for the efficient and accurate computation of waveguide discontinuities in photonic crystals

D. Karkashadze, R. Zaridze, A. Bijamov
Laboratory of Applied Electrodynamics, Tbilisi State University
3, Chavchavadze Ave., 380028 Tbilisi, Georgia
e-mail: lae@lae.ictsu.tsu.edu.ge

Ch. Hafner, J. Smajic, D. Erni
Laboratory for Electromagnetic Fields and Microwave Electronics
Swiss Federal Institute of Technology
ETH-Zentrum, Gloriastrasse 35, CH-8092 Zürich, Switzerland
e-mail: christian.hafner@ifh.ee.ethz.ch

***Abstract*—We presented a novel method for the accurate and efficient computation of the reflection and transmission coefficients of waveguide discontinuities within planar photonic crystals (PhCs). This method proposes a novel kind of field source that optimally excites the dominant waveguide mode and mimics procedures that are typically used for the measurement of reflection coefficients. This technique may be applied to arbitrary field simulators working in the frequency domain. The presented reflection compensation scheme is elucidated along the Method of Auxiliary Sources (MAS). In order to verify the results, we compare two test cases with the rigorous connection technique provided by the Multiple Multipole Method (MMP).**

***Indexing Terms*— method of auxiliary sources (MAS), multiple multipole method (MMP), photonic crystals (PhCs), waveguide discontinuities, boundary conditions.**

I. INTRODUCTION

PHOTONIC crystals (PhCs) have first been proposed as an optical counterpart to semiconductor crystals [1], i.e., in PhCs, the photon plays the role of the electron in semiconductors. In nature, PhCs are rarely observed, but nanotechnology allows one to fabricate PhCs as a novel kind of meta-materials. Although it is nice to know that perfect PhCs may exhibit band gaps, i.e., frequency ranges that do not allow electromagnetic waves to penetrate the crystal, this pure meta-material aspect does not sufficiently explain the current interest in PhCs. In fact, doping makes semiconductors attractive and virtually the same holds for PhCs. Despite of this analogy, doping of PhCs is pretty different from the semiconductor doping because the atoms in semiconductors are compared to rather large macroscopic cells of the PhCs. Nanotechnology may allow one to modify any cell of a PhC quite precisely. By introducing linear defects (line of vacancies or substitutional defects with different size or material) into the lattice structure, one can easily obtain waveguide channels in PhCs [2], [3]. One of the main drawbacks of standard waveguides for integrated optics is the fact that the bending radius must be large compared to the wavelength in order to avoid bending loss. This makes standard structures of integrated optics large compared to the wavelength. The PhC concept allows one to obtain sharp waveguide bends virtually without radiation loss and with zero reflection for some distinct frequency [4]-[6] or even for a wide frequency range [7], when some optimization procedure is subsequently added. For the analysis of PhC waveguide bends and PhC waveguide discontinuities, numerical techniques are required that allow one to accurately compute the S-parameters, i.e., the transmission and reflection coefficients at the PhC's waveguide ports. Up to now, a variety of numerical techniques have been proposed [5], [8]-[10].

During the investigation of numerous models for waveguide discontinuities fast and efficient methods are of great interest. This especially holds when the optimization of a whole PhC device is required, such as an achromatic waveguide bend with almost zero reflection over a wide frequency range within the photonic bandgap (PBG) [7]. It has been observed that such optimizations may lead to very critical cells in a PhC [7] that require a highly accurate numerical model. Thus an efficient but highly accurate method is required.

After a short outline of the standard PhC modeling methods and a short introduction to the MMP-connection approach, we present three new procedures 1) for the excitation of the fundamental waveguide modes, 2) for the reflections compensation at the output ports, and 3) for the S-parameters computation. Together with the Method of Auxiliary Sources (MAS) [11] we can apply these procedures to the efficient computation of waveguide discontinuities in PhCs. Comparisons with the rigorous MMP-connection approach demonstrate that the results are sufficiently accurate for being used within optimization procedures.

II. STANDARD PHC MODELING PROCEDURES

In order to obtain a finite-size model for PhC waveguide devices most of the standard procedures truncate the planar PhC structure at some distance *D* from the discontinuity. After this, some fictitious excitation is introduced in order to excite an incident mode at the input port (see Fig. 1). Typically, plane

1054-4887 © 2004 ACES

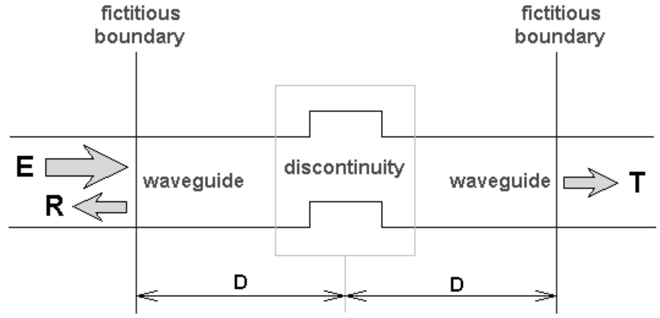

Fig. 1: Schematic treatment of a waveguide discontinuity. The excitation, reflection and transmission of apparent electromagnetic waves are indicated by the corresponding arrows.

waves, monopoles, or dipoles are introduced as fictitious excitations. The proper positioning of the fictitious excitation is crucial because it often happens that a significant amount of the excitation energy does not couple into the desired waveguide mode. Furthermore, the fictitious excitation may also excite higher order or evanescent modes or even additional modes in the output ports. These undesired modes in the output ports can easily be suppressed by using appropriate excitations, i.e. a suitably confined field at the input port. Suppressing the influence of evanescent modes is much more delicate. The distance *D* between the PhC waveguide port and the waveguide discontinuity is limited only by the decay of the evanescent modes produced by the discontinuity itself. Since *D* may extend to large values, the truncated model may also become rather bulky, which leads to long computation times.

An even more difficult problem is imposed by the residual reflections at the output ports. Generally speaking the interface between discrete and continuous translation symmetry (as present in any finite PhC structure) imposes a discontinuity, which causes a bunch of virtually reflected waves that travel back to the discontinuity. Such multiple reflections strongly interfere with a proper estimation of e.g. the S-parameters. The pedestrian way to avoid such undesired reflections at the output ports uses absorbing boundary conditions along the truncation lines (i.e. the fictitious boundary in the Fig. 1). Especially for time-domain methods like FDTD [14], truncation of the infinite space is very straightforward. Thus, many techniques have been developed for absorbing outgoing waves on such boundaries, i.e., at the truncation lines of the finite numerical model. Currently the best technique is PML [15]. Recalling now the special nature of the interface at the PhC boundary where spatial symmetry breaking occurs: Such discontinuity is nearly intractable when using conventional boundary conditions. Therefore, these absorption techniques become very sophisticated, although perfect absorption without any spurious waves is practically impossible.

A laborious way to circumvent the impact of spurious reflections in (time-domain) models relies on time gating, where the distance *D* is increased accordingly to provide a temporal separation between all emergent signal pulses. As a result, such models are either not sufficiently accurate or very time-consuming.

A well-known alternative to the truncated models with fictitious excitation and absorbing boundary conditions is offered by the supercell method that approximates the structure by a periodically continued one [10], [16], [17]. A simple example is given by the W1 defect waveguide (see Fig. 2 for example, where a sequence of point defects is forming the line-defect). The periodic continuation of a waveguide discontinuity is only feasible for relatively simple cases. Furthermore, it is hard to quantify the errors introduced by the periodic continuation, and finally, the supercell method is not efficient at all.

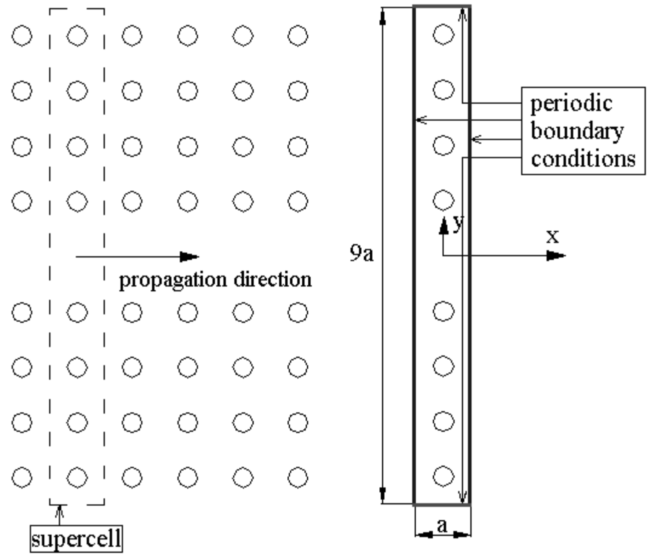

Fig. 2: The supercell approach for a W1 (one line of vacancies) defect waveguide (left). The supercell is defined by its surrounding periodic boundary conditions (right).

III. MMP-CONNECTION PROCEDURE

The most rigorous method for handling waveguide discontinuities in an almost analytic way uses a fictitious separation between the waveguide ports (see Fig. 3) and the area that includes discontinuity [10]. As outlined before along the truncation method, the fictitious separation lines are placed at some distance *D* from the discontinuity. If *D* gets large enough, the evanescent wave amplitude may vanish at the waveguide ports and the fields therein are fully described by the corresponding waveguide's set of guided modes. Along the fictitious separation lines, the modal expansions in the different waveguides are matched with the fields that are excited by the discontinuity region. This is essentially the same procedure as carried out within the standard mode matching technique [18], [19] for the computation of waveguide discontinuities in the microwave regime.

It is worth mentioning that the description of conventional waveguides assumes cylindrical symmetry along the *z*-axis. The longitudinal dependence of the electromagnetic field is then simply described according to

$$\vec{F}\left(\vec{r}_T, z, t\right) = Re\left\{\vec{F}_1\left(\vec{r}_T\right) e^{i\left(\gamma z-\omega t\right)}\right\} \qquad (1)$$

where a harmonic time-dependence of the form

$$e^{-i\cdot\omega\cdot t} \qquad (2)$$

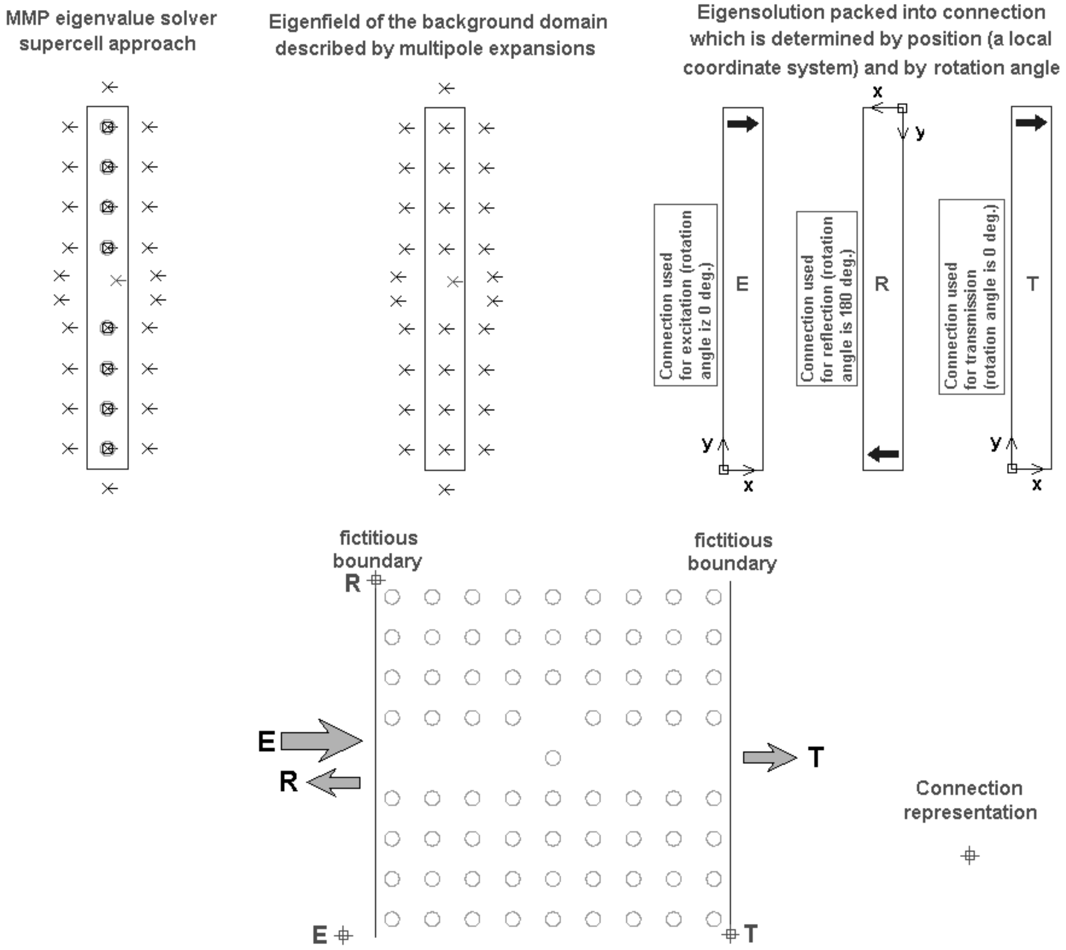

Fig. 3: Schematic description of the MMP-connection procedure: The eigenvalue search is performed as a first step making use of the supercell approach. All information concerning the resulting eigenfield is contained within the set of the waveguide's multipole expansions, which is then packed into a connection. The connection is introduced as a representation of the input (i.e. excitation, E), the reflected (R) and the transmitted (T) electromagnetic wave into the PhC device model.

has been assumed, and the propagation constant γ fully describes the propagation in *z*-direction. Along the direction of propagation, PhC defect waveguides are periodic rather than invariant. Since this is a lower symmetry, the description of the field becomes more complicated. When x is assumed as the direction of the PhC waveguide and d_x stands for the periodicity of the PhC in this direction, we have for each mode

$$\vec{F}(\vec{r}+\vec{e}_x d_x) = \vec{F}(\vec{r})e^{iC_x d_x} \tag{3}$$

where C_x is a complex number that plays the role of the propagation constant. Note that (3) only relates the electromagnetic field at one boundary of the PhC waveguide's unit cell to the field distribution at the opposite boundary (which is separated from the first one by d_x). Thus, C_x does not describe the propagation of the field within the unit cell. Furthermore, if the defect waveguide is confined by two PhC layers that have a finite thickness, in-plane radiation leakage inevitably occurs. This renders C_x to become complex valued even when no material losses are present. The resulting eigenmode analysis gets even more demanding [20], [21], but it does not prevent one from adapting the mode matching technique to PhC waveguides.

The Multiple Multipole Program (MMP) [21] is a very flexible, semi-analytic boundary method that allows one to accurately and efficiently compute not only classical waveguide modes but also the eigenmodes of a PhC waveguide using either the supercell approach or a direct approach that includes radiation leakage as well [20]. In addition the MMP implementation in MaX-1 [22] contains a so-called connection feature. Within this description the data of previously analyzed problem solutions (e.g. the eigenmodes of the PhC waveguide) may be packed into connections that are then introduced as new expansions into the subsequent model of the PhC waveguide discontinuity.

This means that the MMP-connection procedure consists of two different steps: 1) the computation of all relevant modes in the PhC waveguide ports and 2) the computation of the PhC waveguide discontinuity using the modes given by the connections. The former requires the solution of an eigenvalue problem, whereas the latter essentially defines a simple scattering problem.

The main advantages of the MMP-connection scheme are that arbitrary high accuracy and reliability can be reached because of its affinity to mode matching and to analytic procedures. It is important to know that the eigenvalue problem associated with PhC waveguide modes is theoretically demanding, but the resulting matrices set up by the eigenvalue problem are small because only the unit cell of the waveguide must be taken into account. The scattering model for the PhC discontinuity region is theoretically simpler, but numerically much more demanding because it often involves a larger PhC volume than the waveguide's unit cell, leading to a relatively large matrix equation. Referring to the eigensolutions that are provided as connections we are now able to introduce perfect matching conditions for PhC waveguide terminations. This allows us to significantly reduce the size of the simulation domain, i.e., to decrease the distance *D*. Thus, the resulting MMP matrix becomes relatively small. Consequently not only high accuracy but also short computation times are obtained. Therefore, the procedure is very well suited for any kind of optimization scenario such as the successful optimization of achromatic PhC bends [7] and PhC diplexers [23].

The main drawback of the MMP-connection procedure lays in the fact that the computation of guided modes and its embedding into corresponding connections may become quite demanding. Therefore, only experienced users are able to perform such computations. In the following, we present an alternative technique that does not explicitly requires the PhC waveguide's eigenmodes. For the sake of simplicity only the case of single mode PhC defect waveguides are treated hereafter.

IV. IWGA SOURCES

The alternative technique relies on the following procedure: Instead of solving an eigenvalue problem for the PhC waveguide's eigenmodes, we now search for a simple, fictitious excitation that mimics the mode profile at the fictitious boundary which accounts for the waveguide termination. In order to emblematize this approach one has just to envision the reciprocal scenario as depicted in Fig. 4 where a radiation field is excited at the termination of a W1 defect waveguide. Just by time-reversing this radiation field one would already get a beam-like excitation for the corresponding PhC waveguide mode.

Even without knowing the proper radiation field as shown in Fig. 4 one may expect efficient waveguide mode excitation while introducing a fictitious but suitably parameterized beam source. First, Gaussian beams [24] may be applied here, but the implementation of an excitation basis that rests on Gaussian beams is still not very straightforward. Furthermore, using complex-origin multipoles [25] or monopoles becomes more natural in the framework of MMP or MAS whereas for the latter only monopoles (i.e., zero order multipoles) are applied (for TM polarization):

$$E_z = A_0 e^{-\operatorname{Im}\{kR_0\}} H_0^{(1)}\left(kR\right) e^{-i\omega t}, \tag{4}$$

$$R = \sqrt{\left(x-(x_0+i\ell\cos\beta)\right)^2+\left(y-\left(y_0+i\ell\sin\beta\right)\right)^2}, \tag{5}$$

$$R_0 = \sqrt{\left(x_0+i\ell\cos\beta\right)^2+\left(y_0+i\ell\sin\beta\right)^2}, \tag{6}$$

with $H_0^{(1)}(kR)$ being the zero order Hankel function of the first kind, $A_0 e^{-Im\{kR_0\}}$ is a complex normalizing factor, β stands for the angle of maximal radiation direction, x, y is the observation point, whereas x_0, y_0 defines the source location, ℓ the source half-widths, and for the R and R_0 arguments the principal ones are taken. From Fig. 5 we see that e.g. the modulus of the radiation field E_z provided by the complex origin monopole already gives a good approximation of the fundamental mode at the waveguide termination. Even the scattering field (as given in Fig. 4) is well reproduced by E_z. Hence we call this kind of beam excitation the Imitating WaveGuide Apperture (IWGA) source.

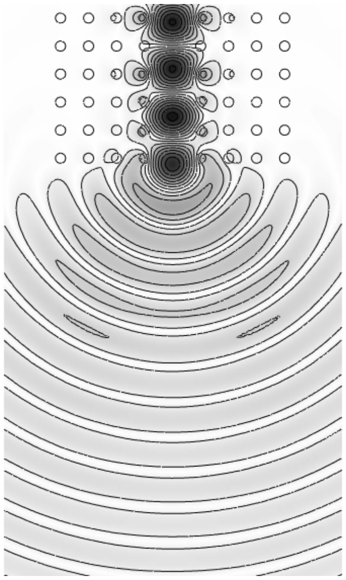

Fig. 4: The E_z-field at a W1 defect waveguide termination.

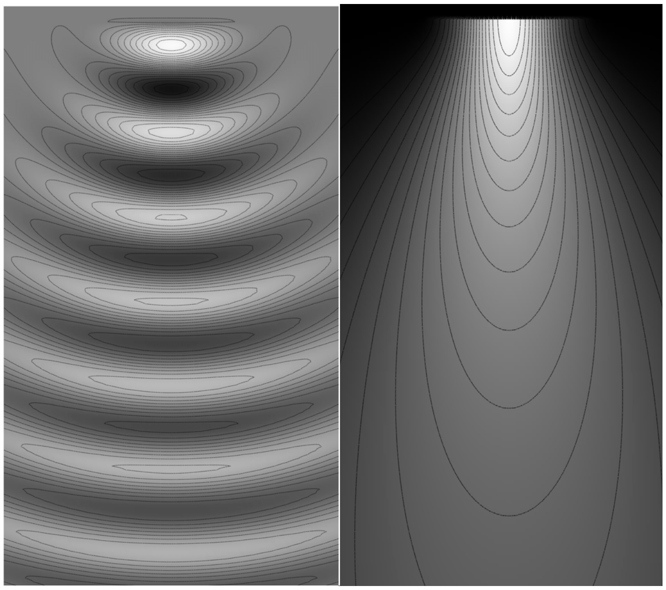

Fig. 5: Intensity plot of E_z (left) and of the modulus of E_z (right) in the *X-Y* plane $x = [-6.0, 6.0]$; $y = [-20.5, 0.5]$; $x_0 = y_0 = 0.0$; $k = 2.0$; $l = 3.0$; $\beta = 270°$.

On one hand, finding an appropriate IWGA source is obviously much easier then finding the waveguide's eigenfields by solving a complex eigenvalue problem. On the other hand as the IWGA source may also excite some undesired evanescent modes, the distance *D* associated to the port must be extended compared to the MMP-connection approach where, in principle, evanescent modes are still tractable. Even if the present version of the proposed technique yet lacks in handling multimode waveguides it is important to see that besides MAS the IWGA source method is also applicable to MMP and all the other frequency domain methods. It should even be possible to develop a time-domain version of this technique.

V. REFLECTION EXTINCTION AT THE OUTPUT PORTS

The IWGA concept essentially handles the excitation problem of the PhC discontinuity in a pragmatic and thus more efficient way than conventional techniques, but it does not solve the problem of the spurious back-reflections at the output ports. This problem is much more demanding. Note that absorbing layers can also be introduced for MMP and MAS but such techniques are difficult and inaccurate for large model sizes. As elucidated earlier the connection concept of MMP removes the reflection problem in a rather rigorous way, but it is difficult to handle. An interesting alternative is obtained from the following consideration.

Given an incident wave, which is transmitted through the waveguide discontinuity and propagates towards one of the output ports. When this mode (which is assumed being fundamental after traveling a sufficient distance in the single-mode defect waveguide) hits the waveguide port (i.e., the boundary of the scattering model associated with the finite PhC structure), it is partially reflected and travels back to the discontinuity (where it is partially reflected again, and so forth). One can now treat the reflected wave at any output port exactly in the same way as the incident wave at the input port. This means one may excite this reflected wave just by setting an IWGA source at the corresponding output port. Assuming a finite PhC structure where a waveguide discontinuity is interconnected to N ports (one input, N–1 outputs), we consider N models consisting of the same scattering model with N different excitations, i.e., N IWGA sources in the N ports. This model is described by a matrix equation with N right hand sides

$$A\,x_{AS} = \left\{ {}^{1}E_z^{inc}\left(x_q, y_q\right),\ {}^{2}E_z^{inc}\left(x_q, y_q\right),\ \dots,\ {}^{N}E_z^{inc}\left(x_q, y_q\right) \right\} \tag{7}$$

where the matrix A is obtained from the numerical method that handles the discontinuity region, $M(x_q, y_q)$ are the collocation points on the interface surface [21], ${}^{n}E_z^{inc}(x_q, y_q)$ denotes the electric field of the n-th IWGA source (with unit amplitude) placed at the corresponding n-th port.

As an illustrative example (that will be scrutinized later) we analyzed the 90° PhC waveguide bend depicted in Fig. 6 using the MAS [11] simulation code. A standard MAS matrix is obtained 1) when approximating the electromagnetic field in each domain by means of auxiliary sources (i.e., monopolar field expansions), 2) by enforcing simple point matching on the domain boundaries, and 3) making use of an appropriate Tikhonov regularization [26]. The MAS matrix equation (7) is then efficiently solved with LU decomposition techniques. Note that the excitation (i.e. the IWGA source) is contained in the right hand side of the MAS matrix equations. Since we have N IWGA sources, we also obtain N right hand sides. Using LU decomposition the system is solved simultaneously for all N right hand sides, i.e. for all waveguide excitations involved.

The outcome of (7) therefore consists of N field solutions according to the N scattering problems (each having an identical geometry but different excitations). Any superposition of these N fields

$$\begin{aligned} E_z^{total}\left(x, y\right) = \left({}^{1}E_z^{scat} + {}^{1}E_z^{inc}\right) + a_2\left({}^{2}E_z^{scat} + {}^{2}E_z^{inc}\right) + \dots \\ + a_N\left({}^{N}E_z^{scat} + {}^{N}E_z^{inc}\right) \end{aligned} \tag{8}$$

is again a solution of the entire problem associated with a linear combination of the corresponding excitations. The linear parameters a_i are then computed in such a way that the amplitude of the incident mode becomes unity whereas the N–1 amplitudes of all reflected waves are forced to vanish. This sets up an additional simple and small system of N–1 equations with regard to the parametrized total field

$$\sum_{n=1}^{N} \int_{L_m^0-\lambda/16}^{L_m^0+\lambda/16} \left(E_z^{total}\left(L_m\right) + i\ E_z^{total}\left(L_m + \lambda/4\right)\right) dL_m = 0 \tag{9}$$

Where $m = 1, 2,\dots,N$ and $2\pi/\lambda = h$ is the propagation constant in the waveguide arm, L_m indicates the centerline of the n-th channel, and L^0_m is its midpoint. In fact (9) defines the matching condition for each PhC waveguide port considering any guided mode involved. Here we just used the spatial shift between real an imaginary part of any traveling wave to be a quarter of a wavelength, which is easily testable by direct substitution of such guided modes into (9). As a result, we obtain the field solution for the waveguide discontinuity but now without any reflections at the output ports

$$\left|E_z^{total}(L_m)\right| = E_m^0 = const\,.$$

The reflection coefficient at the input port and the transmission coefficients for the output ports are computed mimicking the Standing Wave Ratio (SWR) measurement that is well-known from microwave techniques. Thus we define observation lines along the waveguides of the different ports where we compute the total field. Let E^0_m denote the amplitude of the transmitted wave in each output port. The resulting error in fulfilling condition (9) can be determined as follows

$$\frac{1}{L_m}\int_{L_m} \left|\left|E^{total}(L_m)\right| - E_m^0\right|\ dL_m = \Delta_m . \tag{10}$$

The amplitudes of the incident and the reflected waves for the input port are determined according to the following standard procedure (for considerable input reflections)

$$\begin{aligned} E_0^{inc} &= \frac{1}{2}\left(\left|E^{total}\left(L_{in}\right)\right|_{\max} + \left|E^{total}\left(L_{in}\right)\right|_{\min}\right) \\ E_0^{reflect} &= \frac{1}{2}\left(\left|E^{total}\left(L_{in}\right)\right|_{\max} - \left|E^{total}\left(L_{in}\right)\right|_{\min}\right) \\ L_{in} &\in \left[L_{in}^0 - {}^{\lambda}\!/_{2},\ L_{in}^0 + {}^{\lambda}\!/_{2}\right] \end{aligned} \tag{11}$$

where L_{in} stands for the input port's centre line, and L^0_{in} for its midpoint. Later it becomes adequate to normalize the electric field in the finite PhC according to E_0^{inc}. For the output ports where the reflection is significantly lower, it is preferable to determine the transmitted and reflected wave's amplitudes using the relation given below

$$E_{0m}^{transmit} = \frac{1}{L_m}\int_{L_m} \left|E_z^{total}\left(L_m\right)\right| dL_m,$$
$$E_{0m}^{reflected} = \frac{1}{L_m}\int_{L_m} \left|E_{0m}^{transmit} - \left|E_z^{total}\left(L_m\right)\right|\right| dL_m. \tag{12}$$

It should be noted that the evanescent waves being excited at the waveguide discontinuity and at the waveguide ports as well may interfere with the proposed measurement procedure. The waveguide arms must therefore become sufficiently long resulting in a scattering model that is usually larger with respect to the MMP connection approach (but it's still competing well against model sizes required for techniques using imperfect absorbing boundary conditions for the outgoing waves).

In order to illustrate the procedure outlined before, we now consider two simple examples, namely a 90° PhC waveguide bend and a filtering T-junction, which have been previously analyzed along the MMP-connection approach [7], [23].

VI. 90° BEND

Our first test model is a 90° waveguide bend whereas the underlying 2D-PhC consists of dielectric rods arranged in a square lattice and embedded in air. The lattice data are as follows: the radius of each dielectric rod is $r/a = 0.18$ (with $a = 1$ µm being the lattice constant), and the rod's dielectric constant is $\varepsilon = 11.56$. The normalized operation frequency is $a/\lambda = 0.416$. In Fig. 6 the gray rectangle outlines the truncation region of the MAS model. It contains a finite section of 199 rods. Since we know that the PhC structure has a complete band gap only for TM-waves, we only consider *z*-component of the electric field, where *z* is the direction of the cylinder axis. Without lack of generality this considerably simplifies the numerical model.

The electomagnetic field inside each rod is now approximated by a set of *M* auxiliary sources, i.e., monopoles located on auxiliary lines around the rod. Since the rods are circular, it is reasonable to use a concentric circle as auxiliary line for each rod and to distribute the auxiliary sources uniformly on these circles. Similarly, we introduce a circular auxiliary line inside each rod and uniformly distribute *M* auxiliary sources for modeling the field outside the rods. Since we are considering the *TM*-polarization, all auxiliary sources are *E*-type monopoles with unit amplitude. Furthermore, we select $M = 12$ being equal for all rods because the rods have the same shape and size. Thus, we obtain a model with $199 \times 2 \times 12 = 4776$ unknowns. These unknowns are then computed by a simple point matching or collocation method on each rod's $M = 12$ uniformly distributed matching points by enforcing there two boundary conditions, namely the continuity for the longitudinal component of the electric field and for the tangential component of the magnetic respectively. As in conventional scattering problems the structure is illuminated by a well-defined incident wave. In our case the IWGA sources are located in the center of both input and output ports as shown in Fig. 6. Thus, we obtain a linear system of 4776 equations with 4776 unknowns and two right hand sides. The computation time for this problem on an Athlon 1200 PC is approximately 180 seconds when using the LAPACK LU-decomposition routine for the matrix solution.

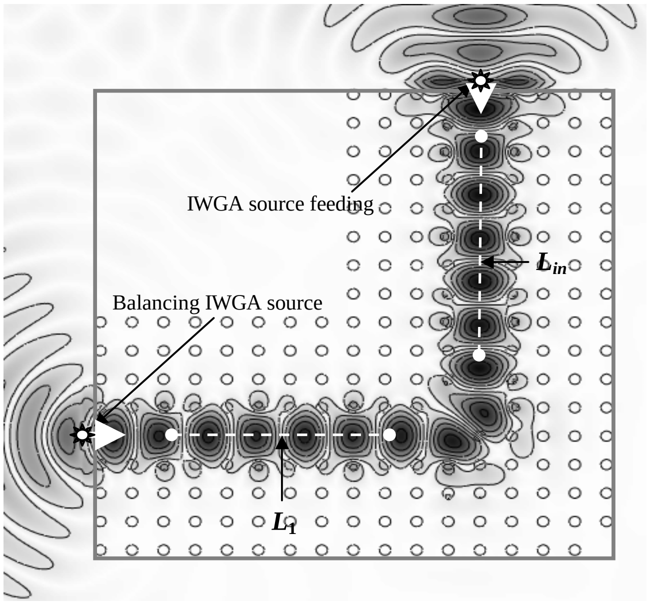

Fig. 6: MAS simulation of the 90° W1 defect waveguide bend. The gray rectangle outlines the truncation boundary of the finite PhC model. The underlying PhC consists of a square lattice with $a/\lambda = 0.416$, $\varepsilon = 11.56$, and $r/a = 0.18$.

(i) MAS simulation; relative error of *E* and *H*: 0.3%; Transmission $T_1 = 91.15\%$; Reflection $R_{in} = 8.58\%$.

(ii) MMP simulation; relative error of *E* and *H*: 0.45%; Transmission $T_1 = 91.26\%$; Reflection $R_{in} = = 8.56\%$.

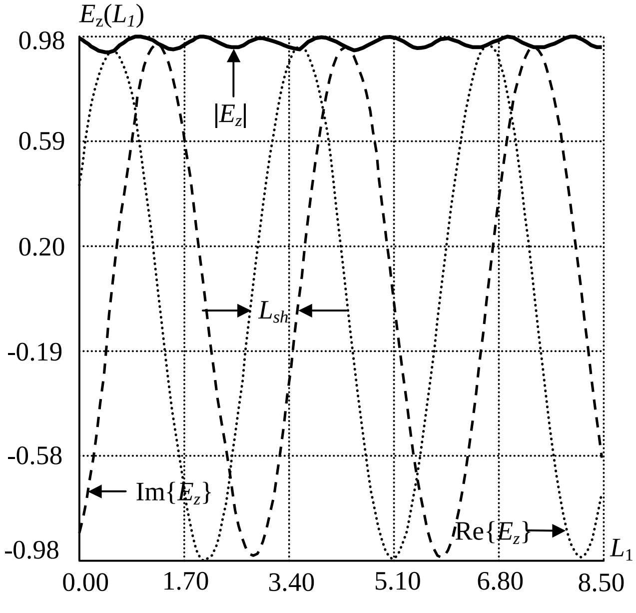

Fig. 7: Electric field E_z along the line L_1. At the low SWR value in the waveguide arm the L_{sh}-value (i.e. the phase-shift between Re{E_z} and Im{E_z}) determine the propagation coefficient: $h = 2\pi/(4L_{sh})$.

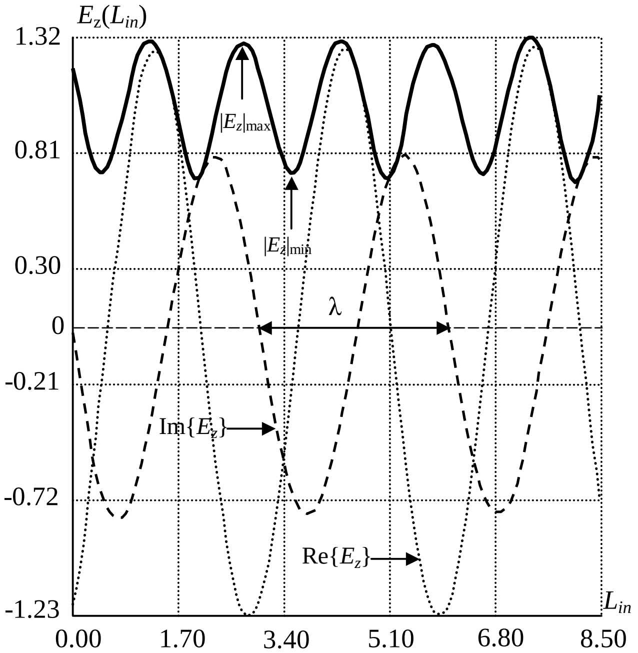

Fig. 8: Electric field along the line L_{in} in input port. The propagation constant is $h = 2\pi/\lambda = 2.068$ and the amplitude of the reflected wave $E_0^{reflect} = \frac{1}{2}(|E_z|_{max} - |E_z|_{min}) = 0.2928$; thus, power reflection becomes $R_{in} = (E_0^{reflect})^2 100\% = 8.58\%$.

As soon as the linear system for the two right hand sides is solved the superposition of the corresponding two solutions is computed in such a way that the reflected wave at e.g. the output port (or the reflected field in the horizontal arm) vanishes.

Fig. 7 shows the resulting dependence of the electric field along the observation line L_1 in the center of the horizontal arm (as defined in Fig. 6). It is clearly visible, that this function shows some oscillatory behavior (instead of being constant) due to inaccuracies in the matching procedure at the output port. It is reasonable to assume that the amplitude of the transmitted wave lays somewhere between the maximum and minimum of the oscillating envelope. We therefore define power transmission according to the mean $|E_z|$ value along L_1:

$$E_{01}^{transmit} = \frac{1}{L_1}\int_{L_m} \left|E_z^{total}(L_1)\right| dL_1 = 0.9547; \tag{13}$$

$$T_1 = \left(E_{01}^{transmit}\right)^2 100\% = 91.15\%,$$

Furthermore, the mean $|E_z|$ deviation form the average value (i.e. the difference between the maximum and minimum value)

$$\Delta_1 = \frac{1}{L_1}\int_{L_m} \left| E_{01}^{transmit} - \left|E_z^{total}(L_1)\right| \right| dL_1 = 0.01 \tag{14}$$

gives us some information about the accuracy of reflection suppression in the output ports with regard to our MAS simulation scenario. Fig. 8 shows the behavior of the electric field in the vertical arm, i.e. near the input port. As one can see this mimics a nice standing wave pattern from which one can not only obtain the reflection coefficient but also an approximation of the propagation constant, or more precisely of the guided mode's characteristic constant C as given e.g. in equation (3). It is easy to understand that C is complex valued due to the inplane radiation leakage [20] of the waveguide but since these losses are usually extremely small C becomes almost real.

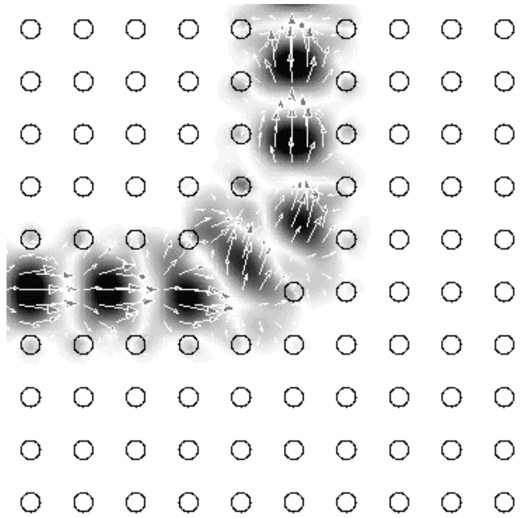

Fig. 9: Poynting vector field distribution within the 90° W1 defect wave-guide bend achieved with MMP. The model data are the same as in Fig. 6.

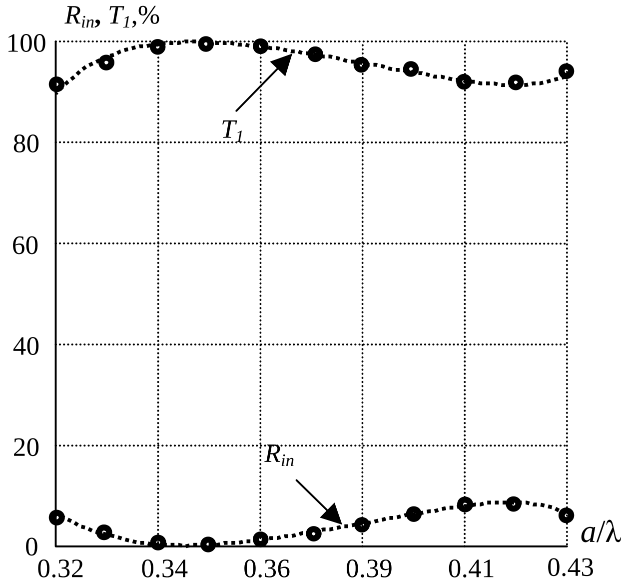

Fig. 10: Comparison of the MAS (circles) and MMP (dashed lines) model for a 90° W1 defect wave-guide bend as a function of the normalized frequency a/λ. The discrepancy is less than 1%.

In addition to the error estimated for the reflection suppression, we can also consider energy conservation. Neglecting radiation leakage we obtain $T_1 + R_{\text{in}} \approx 91.15\% + 8.58\% = 99.73\%$. These internal error checks already show an acceptable accuracy of the proposed MAS model. In order to obtain even more information on the quality, we compare these results with those of a model based on MMP-connections. The comparison is visualized in Fig. 10.

As one can see from e.g. Fig. 6 and Fig. 9, the MMP model is considerably smaller and consists of only 89 rods. Here, the field inside each rod is approximated by a Bessel-type expansion whereas the field outside is represented by a multipole expansion. The total number of unknowns per rod is 22, that is almost the same as in the MAS model. Thus, we only have $22 \times 89 = 1958$ unknowns, i.e., less then half of what we have for the MAS model. But now, the handling of the output ports with connections requires the introduction of a fictitious boundary that separates the region of the PhC discontinuity from the PhC waveguide problem. Along these fictitious boundaries, additional multipoles must be placed together with the connections that describe the waveguide modes. Finding an appropriate set of matching points for the resulting model is rather difficult. In order to overcome these problems, MMP works with a generalized point matching technique that leads to an overdetermined system of equations which is then solved in the least squares sense. In our example, we obtain 2181 unknowns for 8964 matching conditions. The solution of this system involves the QR decomposition routine of LAPACK and takes 177 seconds, i.e., almost the same computation time as the MAS solution. Note that the MMP system of equations is more than four times overdetermined. Usually two times overdetermined systems are still sufficient and in our special case, we could use even no overdetermination for the PhC lattice (i.e. the rods) and an overdetermination factor two for the fictitious boundaries. This would allow us to reduce the computation time of the MMP-connection model by a factor of three. Since this model serves only for comparison purposes and because the minimization of the computation time in the framework of MMP could become quite tricky, we did not optimized the model with regard to speed-up.

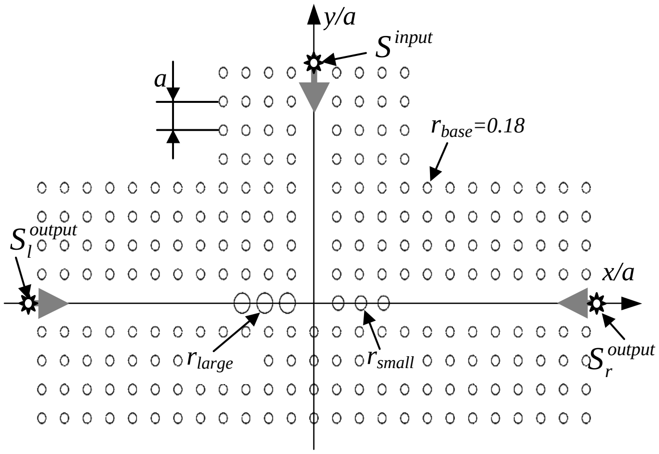

Fig. 11: Geometry of the filtering T-Junction (diplexer).The radii of the rods are given in units of lattice the period *a*. For all of rods: $\mu = 1.0$; $\varepsilon = 11.56$.

Fig. 10 shows the comparison of MAS and MMP results where we can see an excellent agreement between these two results. Furthermore, we observe our error estimation to be quite reliable. In conclusion, the simulation of complicated PhC waveguide discontinuities is now reduced to the solution of a standard scattering problem.

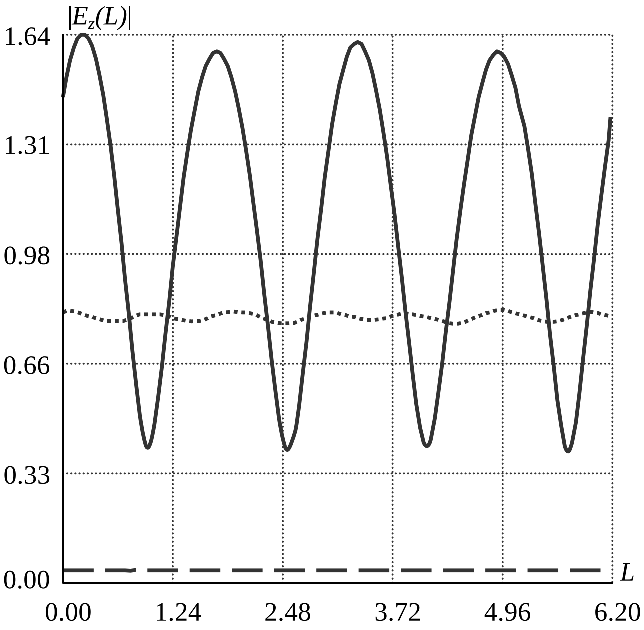

Fig. 12: Distribution of $|E_z|$ along the test lines at $f = 1.23 \cdot 10^{14}$ Hz: —— vertical arm; – – – – left arm; ········ right arm

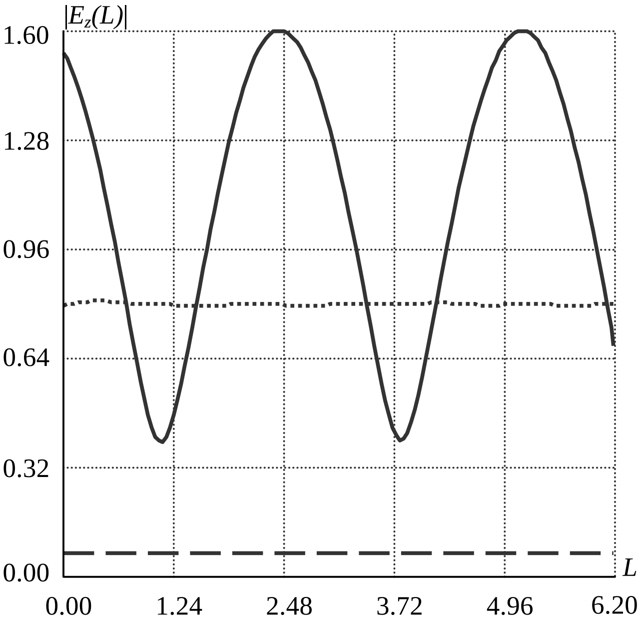

Fig. 13: Distribution of $|E_z|$ along the test lines at $f = 1.038 \cdot 10^{14}$ Hz: —— vertical arm; – – – – right arm; · · · · · · · · left arm

VII. FILTERING T-JUNCTION

The analysis of filtering T-junction as depicted in Fig. 11 is more demanding than the 90° PhC waveguide bend for several reasons. First of all, it has two output ports where the incoming wave is guided to the left output port at an operating frequency of $f = 1.038 \cdot 10^{14}$ Hz and to the right output port for $f = 1.23 \cdot 10^{14}$ Hz. Within our analysis we must evaluate this model at least for two different frequencies, i.e., the computation time is doubled.

Furthermore, wavelength selective power splitting is enabled,

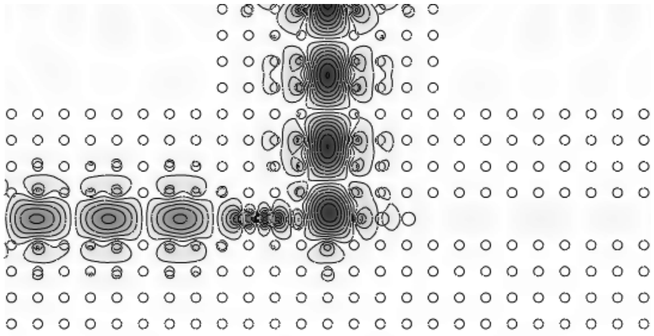

Fig. 14: MAS analysis: E_z-field of the filtering T-junction at $f = 1.038 \cdot 10^{14}$ Hz.

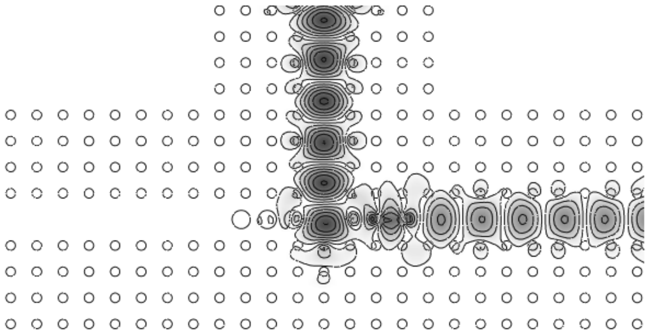

Fig. 15: MAS analysis: E_z-field of the filtering T-junction at $f = 1.23 \cdot 10^{14}$ Hz.

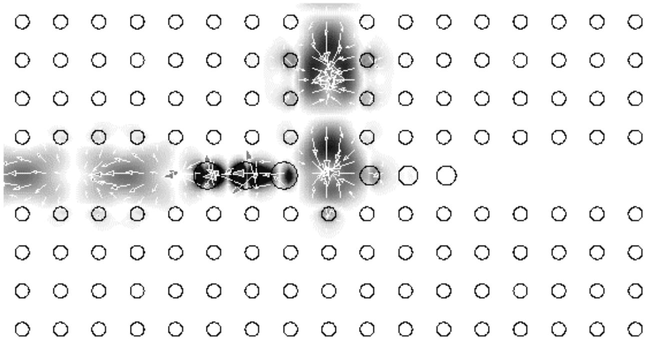

Fig. 16: MMP analysis: Poynting vector field distribution within the filtering T-junction at $f = 1.038 \cdot 10^{14}$ Hz (left diplexer channel).

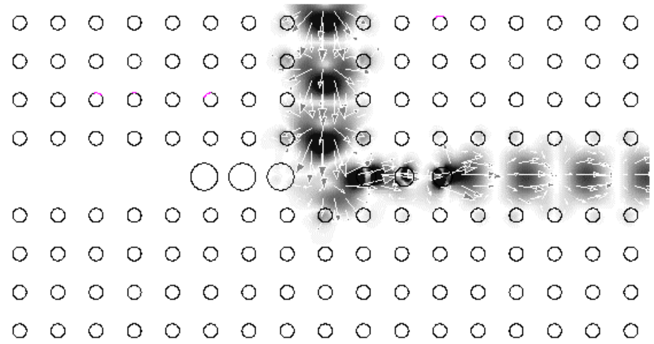

Fig. 17: MMP analysis: Poynting vector field distribution within the filtering T-junction at $f = 1.23 \cdot 10^{14}$ Hz (right diplexer channel).

by introducing corresponding dispersive elements (like e.g. substitutional defects) into the two output waveguides of the T-junction. Such substitutional defects may consist of rods with different sizes compared to those of the underlying PhC lattice

$$r_{base} = 0.18; \quad r_{large} = 0.35; \quad r_{small} = 0.25.$$

The numbers of auxiliary sources and matching points for these rods are slightly higher (we use $M = 14$ for the rods that constitute the PhC lattice and $M_f = 16$ for the substituitional defects).

The MAS model is described here by a matrix equation, which contains 6576 equations with 6576 unknowns and three right hand sides due to the existence of one auxiliary IWGA source per port (see Table 1).

Table 1

Source	x_0	y_0	β	l
Input	0.0	8.5a	270º	3.5a
Left	-12.5a	0.0	0º	3.5a
Right	12.5a	0.0	180º	3.5a

The unknown amplitudes of the IWGA sources are determined according to condition (9), i.e. the reflections suppression condition at the cutoff slice $x_0 = \pm(12 \cdot a + r_{base})$. We shall not care about the matching condition at the input port $y_0 = 8 \cdot a + r_{base}$ because there is always a reflected wave present coming from the discontinuity (i.e. branching region) itself.

Table 2

	$f = 1.038 \cdot 10^{14}$ Hz		$f = 1.23 \cdot 10^{14}$ Hz	
Source	$\|A_0\|$	Phase	$\|A_0\|$	Phase
Input	1.0	0°	1.0	0°
Left	0.2774	-35.4°	0.0058°	-75.0°
Right	0.0232	-22.1°	0.1370°	-20.7°

This wave will impact the incoming field accordingly but its influence is minimized when using the input field amplitude as normalization for all other wave amplitudes involved. In all other respects the procedure is the same as for the 90° PhC waveguide bend. The solution of the excitation problem (7) and the reflection suppression condition (9) for the given T-junction (Fig. 11) provide one with the values for the complex IWGA sources' amplitudes (Table 2). Since we now dispose of the IWGA source amplitudes (and phase values) providing efficient wave matching at the output ports, we obtain almost constant field distributions along the two observation lines in the output arms of the T-Junction for the two different frequencies (see Fig. 12 and 13).

Table 3

$f = 1.038 \cdot 10^{14}$ Hz, $h = 2\pi/\lambda = 1.156$					
Port	$\|E^{trans}\|$	$T(\%)$	$\|E^{reflect}\|$	$R(\%)$	SWR
Input	1.0	100	0. 6031	36.38	2.144
Left	0.7982	63.71	0.0024	0.001	1.000
Right	0.0652	0.42	0.0002	0.000	1.000

Table 4

Case	MMP solution				MAS solutions			
	R (%)	T_l (%)	T_r (%)	Σ (%)	R (%)	T_l (%)	T_r (%)	Σ (%)
Left	35.37	63.38	0.41	99.16	36.38	63.71	0.42	100.51
Right	36.51	0.11	63.24	99.86	36.02	0.11	63.76	99.89

Knowing the field distribution in the two output channels the transmission/reflection coefficients, the propagation constants and a first estimate of the error can be obtained using equations (9)-(12):

a) Propagation constant: $h = 2\pi/\lambda = 2.00$

b) Amplitude of the reflected wave in the output port

$$E_{in}^{reflect} = \frac{1}{2}\left(\left|E_z\left(L_{in}\right)\right|_{\max} - \left|E_z\left(L_{in}\right)\right|_{\min}\right) = 0.6002,$$

the corresponding power reflection coefficient and the SWR

$$R_{in} = \left(E_{in}^{reflect}\right)^2 \cdot 100\% = 36.02\%\,,$$

$$SWR = \frac{1+\left(E_{in}^{reflect}\right)^2}{1-\left(E_{in}^{reflect}\right)^2} = 2.125, \quad E_{in}^{trans} = 1.0;$$

c) Amplitude of the transmitted wave in the right arm

$$E_{right}^{transmit} = \frac{1}{L_{right}} \int_{L_{right}} \left|E_z^{total}\left(L_{right}\right)\right| dL_{right} = 0.7985,$$

and the corresponding transmission coefficient

$$T_{right} = \left(E_{right}^{transmit}\right)^2 100\% = 63.76\%\;;$$

d) Amplitude of the reflected wave from the end of the right arm

$$E_{right}^{reflected} = \frac{1}{L_{right}} \int_{L_{right}} \left|E_{right}^{transmit} - \left|E_z^{total}\left(L_{right}\right)\right|\right| dL_{right} = 0.0075,$$

and the corresponding standing wave ratio $SWR = 1.002$;

e) Amplitude of the transmitted wave in the left arm

$$E_{left}^{transmit} = \frac{1}{L_{left}} \int_{L_{left}} \left|E_z^{total}\left(L_{left}\right)\right| dL_{left} = 0.0335,$$

and the corresponding transmission coefficient

$$T_{left} = \left(E_{0left}^{transmit}\right)^2 100\% = 0.11\%\;;$$

f) Amplitude of the reflected wave from the end of the left arm

$$E_{left}^{reflected} = 0.0003,$$

and corresponding standing wave ratio is $SWR = 1.002$.

g) Energy balance: $\Delta W = T_{in} - (R_{in} + T_{left} + T_{right}) = 0.1\%$

The solution of the initial boundary problem provides the continuity of the *E*- and *H*-field components along the boundary with the error of less than 0.1% Having such high precision of the calculation allows detailed investigation of the wave propagation characteristics in complicated finite PhC. For example Fig. 14 and Fig. 15 show the contour plot of the electromagnetic field component E_z for the given diplexer geometry. The calculated amplitude of the electric field along the each waveguide channel for a frequency of $f = 1.038 \cdot 10^{14}$ Hz is depicted in Fig. 13 whereas the transmission/reflection coefficients are listed in Table 3.

The overall simulation procedure and the degree of accuracy is comparable to the analyis of the 90° PhC waveguide bend. As shown in Fig. 14 and Fig. 15 accurate calculations allow a very detailed description of the complicated fields in finite PhC devices. In order to compare the results with MMP, we use a MMP-connection model (see Fig 16 and 17) that sets up an over-determined 2974 × 9126 matrix and requires almost the same computation time as the corresponding MAS-model. Comparable figures that result from the two methods are listed in Table 4. As one can see, there is an excellent agreement between both methods.

VIII. CONCLUSIONS

We have presented a new powerful method for the accurate and efficient computation of PhC waveguide discontinuities. The method essentially proposes (i) the introduction of special IWGA sources that excite the guided modes in the PhC waveguides and (ii) it provides also a very straightforward technique for suppressing reflected waves at the waveguide ports. Together with such excitation and matching conditions the method delivers an additional technique for the computation of the S-parameters in PhC devices. This rather intuitive way (i.e. when relying on the minimization of the SWR) will gain recognition especially when complicated waveguide structures in e.g. planar 3D-PhCs are involved and thus proper eigenmode calculation becomes too cumbersome. Even if the proposed technique was developed for the method of auxiliary sources (MAS) it will easily apply for any other frequency domain method.

IX. ACKNOWLEDGEMENT

This work was supported by the Swiss National Science Foundation in the framework of project NFP-SCOPES-7GEPJ065551 and the research initiative NCCR Quantum Photonic.

REFERENCES

[1] E. Yablanovich, “Inhibited spontaneous emission in solid-state physics and electronics”, *Phys. Rev. Lett.*, 58, pp. 2059-2062, 1987.

[2] E. Centeno, D. Felbacq, “Guiding waves with photonic crystals,” *Opt. Commun.* 160, pp. 57-60, 1999.

[3] H. Benisty, “Modal analysis of optical guides with two-dimensional photonic band-gap boundaries,” *J. Appl. Phys.* 79, pp.7483-7492, 1996.

[4] R. D. Meade, A. Devenyi, J. D. Joannopoulos, O. L. Alerhand, D. A. Smith, K. Kash, “Novel applications of photonic band gap materials: Low-loss bends and high Q cavities,” *J. Appl. Phys.* 75, pp. 4753-4755, 1994.

[5] A. Mekis, J. C. Chen, I. Kurland, S. Fan, P. R. Villeneuve, J. D. Joannopoulos, “High transmission through sharp

bends in photonic crystal waveguides," *Phys. Rev. Lett.* 77, pp. 3787-3790, 1996.

[6] A. Chutinan, M. Okano, S. Noda, "Wider bandwidth with high transmission through waveguide bends in two-dimensional photonic crystal slabs," *Appl. Phys. Lett.* 80, pp. 1698-1700, 2002.

[7] J. Smajic, Ch. Hafner, D. Erni, "Design and optimization of an achromatic photonic crystal bend", *Opt. Express* 11, 1378-1384,2003, http://www.opticsexpress.org/abstract.cfm?URI=OPEX-11-12-1378 .

[8] M. Koshiba, Y. Tsui, M. Hikari, "Time-domain beam propagation method and its application to photonic crystal circuits," *J. Lightwave Technol.* LT18, pp. 102-110, 2000.

[9] J. Yonekura, M. Ikeda, T. Baba, "Analysis of finite 2-D photonic crystals of columns and lightwave devices using the scattering matrix method," *J. Lightwave Technol.* LT17, pp. 1500-1508, 1999.

[10] E. Moreno, D. Erni, Ch. Hafner, "Modeling of discontinuities in photonic crystal waveguides with the multiple multipole method," *Phys. Rev. E* 66, 036618, 2002.

[11] F. G. Bogdanov, D. D. Karkashadze, and R. S. Zaridze, in "Generalized Multipole Techniques for Electromagnetic and Light Scattering", edited by T. Wriedt, pp. 143-172, Elsevier, Amsterdam, 1999.

[12] A. Bijamov, I. Paroshina, D. Karkashadze, Simulation of optical control devices based on photonic band structures. Proceedings of the Seminar/ Workshop "Numerical Solution of Direct and Inverse Problems of the Electromagnetic and Acoustic Waves Theory, DIPED-2003, 2003.

[13] D.D.Karkashadze, F.G.Bogdanov, R.S.Zaridze, A.Y.Bijamov, C.Hafner, and D.Erni. "Simulation of Finite Photonic Crystals Made of Biisotropic or Chiral Material. Using the Method of Auxiliary Sources". Advances in Electromagnetics of Complex Media and Metamaterials. Edited by Said Zouhdi, Ari Sihvola and Mohamed Arsalane, NATO Science Series. II Mathematics, Physics and Chemistry - Vol. 89, pp. 175-193, 2003.

[14] K. S. Yee, "Numerical solution of initial boundary value problems involving Maxwell's equations in isotropic media," *IEEE Trans. Antennas Propagat.*, vol. AP-14, pp. 302-307, 1966.

[15] J. P. Berenger, "A perfectly matched layer for the absorption of electro-magnetic waves, " *J. Comp. Phy.* 114, pp. 185-200, 1994.

[16] K. Sakoda, *Optical Properties of Photonic Crystals*, Springer, Berlin, 2001.

[17] J. D. Joannopoulos, R. D. Meade, J. N. Winn, *Molding the Flow of Light*, Princeton University Press, 1995.

[18] A. Wexler, "Solution of waveguide discontinuities by modal analysis," *IEEE Trans. On Microwave Theory and Techniques*, Vol. MTT-15, pp. 508-517, 1967.

[19] R. Sorrentino, *Numerical methods for passive microwave and milimeter-wave structures*, IEEE Press, Ch. 8, New York, 1989.

[20] K. Rauscher, J. Smajic, D. Erni, and Ch. Hafner "The open-supercell approach for the eigenmode analysis of 2-D photonic crystal defect waveguides," submitted to *Phys. Rev. E.*, 2003.

[21] Ch. Hafner, *Post-modern Electromagnetics Using Intelligent MaXwell Solvers*, John Wiley & Sons, 1999.

[22] Ch. Hafner, MaX-*1: A visual electromagnetics platform*, John Wiley & Sons, 1998.

[23] J. Smajic, Ch. Hafner, D. Erni, "On the design of photonic crystal multi-plexers", *Opt. Express* 11, pp. 566-571, 2003, http://www.opticsexpress.org/abstract.cfm?URI=OPEX-11-6-566 .

[24] G. A. Deschamps, "Gaussian Beams as a Bundle of Complex Rays", *Electron. Lett.* 7, pp. 684-685, 1971.

[25] A. Boag, R. Mittra, "Complex Multipole Beam Approach to 3D Electro-magnetic Scattering Problems", *J. Opt. Soc. Am. A*, Vol. 11, pp. 1505-1512, 1994.

[26] A. Tikhonov, V. Arsenin, *Solutions of ill-posed problems*, Winston and Sons., Washington DC, 1977.

Christian Hafner was born in Zurich, Switzerland, in 1952. He received a Dipl. El.-Ing. Degree, Doctoral Degree, and Venia Legendi from Swiss Federal Institute of Technology (ETH), Zürich in 1975, 1980, and 1987 respectively. In 1999 he was given the title of Professor.

Since 1976 he has been working at the ETH on the development of methods for computational electromagnetics and for optimization problems. He has developed the Multiple Multipole Program (MMP), the MaX-1 package, the Generalized Genetic Programming (GGP) code, and various optimization codes. He worked on various applications (electrostatics, EM scattering, antenna, waveguides and waveguide discontinuities, gratings, chiral media, etc.). His current focus is on photonic crystals, microstructured optical fibers, and Scanning Nearfield Optical Microscoes (SNOM). In 1990 he obtained the second prize of the Seymour Cray avard for scientific computing and in 2001 he has been awarded the 2000 Outstanding Journal Paper Award by the Applied Computational Electromagnetics Society. He is member of the Electromagnetics Academy.

Jasmin Smajic was born in Tuzla, Bosnia and Herzegovina, in 1971. He received a Dipl. El.-Ing. degree from Faculty of Electrical Engineering, Tuzla in 1996. Since 1996 he has been working at the Faculty of Electrical Engineering in Tuzla on numerical calculation of electromagnetic field, numerical mathematics and optimization. He got a M.Sc. degree in 1998 from the Faculty of Electrical Engineering and Computing in Zagreb, Croatia, for the analysis of magnetic field in non-linear material. He received a Ph.D. in 2001 from Faculty of Electrical Engineering and Computing in Zagreb, Croatia, for numerical calculation of time-varying field in non-linear material and electrical machine design optimization. Since 2002 he is a postdoctoral research fellow in the Computational Optics group of the Laboratory for Electromagnetic Fields and Microwave Electronics at the ETH Zurich. His current research interest includes numerical field calculation and design optimization of photonic crystal devices.

Daniel Erni was born in Lugano, Switzerland, in 1961. He received an El.-Ing. HTL degree from Interkantonales Technikum Rapperswil HTL in 1986, and a Dipl. El.-Ing. degree from Swiss Federal Institute of Technology (ETH), Zürich in 1990, both in electrical engineering. Since 1990 he has been working at the Laboratory for Electromagnetic Fields and Microwave Electronics (ETH) on nonlinear wave propagation, laser diode modeling (multi-section DFB and DBR lasers, VCSELs), computational electromagnetics and on the design of non-periodic optical waveguide gratings e.g. by means of evolutionary algorithms. He got a Ph.D. degree in 1996 for the investigation of non-periodic waveguide gratings and non-periodic coupled cavity laser concepts. His current research interests includes highly multimode optical signal transmission in optical interconnects (i.e. in optical backplanes with extremely large waveguide cross sections) as well as alternative waveguiding concepts for dense integrated optical devices like e.g. photonic crystal devices, couplers and WDM filter structures. In 2001 he has been awarded the 2000 Outstanding Journal Paper Award by the Applied Computational Electromagnetics Society for a contribution on the application of evolutionary optimization algorithms in computational optics. Dr. Erni is the head of the Communication Photonics Group at ETH Zurich (www.photonics.ee.ethz.ch). He is also a member of the Swiss Physical Society (SPS), of the German Physical Society (DPG), of the Optical Society of America (OSA), and of the IEEE

David Karkashadze was born in Tbilisi, Georgia in 1949. He received Master Science in Radio-physics and Quantum Electronics and Candidate of Science Degrees in Radio-physics and Quantum Electronics from Tbilisi State University (TSU), Georgia in 1971 and 1981 respectively.

Since 1971 he has been working at the Department of Physics as a teacher, since 1985 to present General Physics Associate Professor (TSU).

His current research interests include: numerical methods for solution diffraction and wave propagation problems; theoretical and experimental investigation, computer simulation of electrodynamics phenomena; ESD and Transient field calculation; theory and application of wave scattering and propagation in complex (Chiral and Bi-anisotropic) media; development of EM software for engineering.

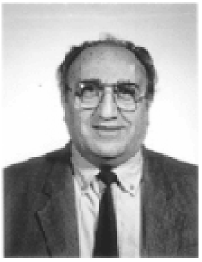

Revaz Zaridze was born in May 8, 1938, in Georgia, USSR. He received the M.S. and Candidate of Science degrees in radio engineering from Tbilisi State University (TSU), Georgia, in 1962 and 1973, respectively, and the Doctor degree from the Radio-Engineering Institute of the USSR Academy of Sciences, Moscow, USSR, in 1986.

Since 1964, he has taught General Physics course in the Department of Physics, currently is a General Physics Professor. Since 1973 he is Head of the Laboratory of Applied Electrodynamics, TSU, leading the group in researching problems in diffraction and propagation of electromagnetic waves. He developed the numerical method of auxiliary sources for solving the applied problems. 1995 – Member of Management Committee of European Society - COST 243, 261 in area of EMC, Member of IEEE, Chapter Organizer and Chapter Chairman of IEEE Division in Republic of Georgia. His research interests have been in numerical methods for solution diffraction and wave propagation problems, theoretical and experimental investigation of electrodynamics problems, computer simulation of electrodynamics phenomena in multipurpose systems, scattering of EM and acoustic fields from bodies with complex shapes and various surface, field reconstruction and visualization. Also, ESD and transient field calculation, wave propagation in chiral and bianizotropic media, influence of the electromagnetic field on biological object, imaging, tomography, holography, and EMC analysis.

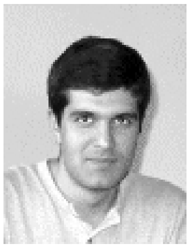

Alexander Bijamov was born in Tbilisi, Georgia in 1978. He received his Bachelor of Physics and Master of Physics degree on the investigation and software creation for the e mobile phones antennas development from the Faculty of Physics at the Tbilisi State University in 1999 and in 2001 correspondingly. Since 1997 he has been working in the Laboratory of Applied Electrodynamics ant the Department of Physics, TSU. He worked on various applications in the field of Applied Electrodynamics and EMC problems, mainly on mobile antenna design. His current research interests include Antenna-with–head interaction modeling and development and simulation of the FPC-based devices. Currently he works on his PhD thesis on Photonic Crystals

GENERALIZED DESIGN OF MULTI-RESONANT DIPOLE ANTENNAS USING KOCH CURVES

K.J. Vinoy, Jose K. Abraham, and V.K. Varadan
Center for the Engineering of Electronic and Acoustic Materials and Devices
The Pennsylvania State University, 212 EES Building, University Park, PA 16802

Abstract: Generalizations of fractal Koch curves and their use in designing multi-resonant antennas are presented in this paper. Both recursive and non-recursive generalizations of the curve are examined. Variation of the indentation angle is used for this approach. Although this variation has a direct bearing on the unfolded length of the curve, this should be considered as a primary variable since several geometries with the same unfolded length can be constructed with different permutations of indentation angles. Antenna input characteristics such as the primary resonant frequency, the input resistance at this resonance, and ratios of the first few resonant frequencies have been studied by numerical simulations. This study shows that it is possible to design multi-resonant antennas using Koch curves with various indentation angles. Identifying similar parameters with other known fractal geometries would offer a viable route for designing multiband and multifunctional antennas for modern wireless applications using them.

Keywords: Fractals, Multifrequency antennas, Wire antennas.

1. INTRODUCTION

Fractal geometries have found numerous applications in several fields of science and engineering in the past few decades, ever since the term fractal was coined by Mandelbrott for a class of seemingly irregular geometries [1]-[5]. Disciplines such as geology, atmospheric sciences, forest sciences, physiology have all benefited significantly by fractal modeling of several naturally occurring phenomena. In electromagnetics, fractal geometries have been studied in the context of various wave propagation scenarios. Scattering and diffraction from fractal screens have been studied extensively [6]-[7]. More recently fractal geometries have also been used in frequency selective screens [8]-[10]. Similarly, fractal concepts have also been used in antenna engineering. The primary motivation for the use of fractals in this area has been to extend antenna design and synthesis concepts beyond Euclidean geometry [11]-[12]. Obtaining special antenna characteristics using a fractal distribution of elements is the main objective of the study on fractal antenna arrays. Self-similar arrays have frequency independent multi-band characteristics [13].

Antenna elements with fractal shapes have also been investigated in recent years. It is the irregular nature of these geometries that has caught the attention of antenna designers - primarily as a past-time. Over the past decade or so, several antenna properties have been qualitatively linked to the nature of these geometries. With the deepening of such an understanding of relationships between geometric properties and antenna features, a new class of antennas, called fractal shaped antennas is becoming popular. Initial investigations with fractal geometries for antenna applications have been experimental. Fractal geometries such as Koch curves, Minkowski curves, Sierpinski carpets were investigated by Cohen for various types of antennas [14]. Fractal trees were also explored and found to have multiband characteristics [15]. Self-similarity of these fractal geometries has since been qualitatively associated with multiband characteristics of antennas using them. Several self-similar geometries have therefore been explored to obtain multiband antenna characteristics [16]-[19]. For example, Sierpinski gaskets have been studied extensively for monopole and dipole antenna configurations [20]. The self-similar current distribution on these antennas is expected to cause its multi-band characteristics [21]. Yet another fractal geometry pursued by many antenna researchers is the Koch curve. Several variants of this geometry have been used as dipole, monopole, loop and patch antennas with equally diverse performance [14], [22]-[28]. Historically, Koch monopoles are among the first antennas based on a fractal geometry designed as small sized antennas. In addition to being small,

1054-4887 © 2004 ACES

these geometries can potentially lead to multiband antenna characteristics [22].

Fractal shaped antennas for numerous wireless applications have been commercialized recently. The advantages of using fractal shaped antenna elements are manifold. These geometries can lead to antennas with multiband characteristics, often with similar radiation characteristics in these bands. However, it may be pointed out that the ordered nature of fractals introduces a substantial advantage over an antenna geometry obtained by arbitrarily shrinking the geometry, and this could be exploited in novel antenna design and analysis approaches. However, thus far the research on using these geometries, has more or less concentrated on introducing them into the realm of antenna design, without seriously getting into novel design ideas. There are few exceptions including the works by Werner et. al. [28]-[29] where antenna properties were optimized by modifying the geometry using a genetic algorithm. The present authors have reported a design approach for Hilbert curve and Koch cure dipole antennas making use of its fractal features [30]-[33].

In this paper however, it is attempted to make a parametric study of dipole antennas using Koch curves, with the indentation angle as the design parameter. If this angle is kept a constant for various iterations, the resultant geometry is self-similar. A variation in the indentation angle of these self-similar geometries can be used to obtain a parametric correlation between the antenna characteristics and a mathematically expressible feature (e.g., fractal dimension) of the fractal geometry [32]-[33]. However a convenient means for designing such antennas can be obtained if the indentation angles for all iterations are chosen independently. The resultant geometry is non-recursive and may not be truly called fractal.

The geometries studied here may be considered as a special case of those presented in [28] and [29], since the initiator in the present case has one line segment less. The approach for generalization of the geometry is described in the next section. Results of numerical simulations using NEC for antennas with these geometries are described in Section 3. It has been found that the indentation angle of each Koch iteration may be varied to design multi-resonant antennas with variable frequency intervals. A brief summary of the new findings in this paper are presented in Section 4. It is expected that the use of these ideas would significantly reduce the computational intensity of optimization approaches for design of antennas using fractal geometries, and would help antenna designers approach the problem with due merit.

2. GENERALIZATION OF KOCH CURVES

The antenna geometry used in this paper is based on a fractal curve originally introduced by Swedish mathematician Helge von Koch in 1904 [34]. Several generalizations of the original geometry exist. The recursive construction of the basic fractal curve is shown in Fig. 1. To distinguish this from generalizations introduced later, this geometry will be referred to as the *standard Koch curve* for the rest of the discussions.

The geometric construction of the standard Koch curve is fairly simple. One starts with a straight line, called the initiator. This is partitioned into three equal parts, and the segment at the middle is replaced with two others of the same length. This is the first iterated version of the geometry and is called the generator. The process is reused in the generation of higher iterations.

It may be recalled that each segment in the first iterated curve is $^1/_3$ the length of the initiator. There are four such segments. Thus for n^{th} iterated curve the unfolded (or stretched out) length of the curve is $(^4/_3)^n$. This is an important property useful in the design of antennas using them.

2.1. IFS for the Standard Koch Curve

An iterative function system (IFS) can be effectively used to generate the standard Koch curve. A set of affine transformations forms the IFS for its generation. Let us suppose that the initiator (unit length) is placed along the *x*-axis, with its left end at the origin. The transformations to obtain the segments of the generator are

$$W_1\begin{pmatrix} x' \\ y' \end{pmatrix} = \begin{bmatrix} \frac{1}{3} & 0 \\ 0 & \frac{1}{3} \end{bmatrix}\begin{pmatrix} x \\ y \end{pmatrix}, \tag{1}$$

$$W_2\begin{pmatrix} x' \\ y' \end{pmatrix} = \begin{bmatrix} \frac{1}{3}\cos 60° & -\frac{1}{3}\sin 60° \\ \frac{1}{3}\sin 60° & \frac{1}{3}\cos 60° \end{bmatrix}\begin{pmatrix} x \\ y \end{pmatrix} + \begin{pmatrix} \frac{1}{3} \\ 0 \end{pmatrix}, \tag{2}$$

$$W_3\begin{pmatrix} x' \\ y' \end{pmatrix} = \begin{bmatrix} \frac{1}{3}\cos 60° & \frac{1}{3}\sin 60° \\ -\frac{1}{3}\sin 60° & \frac{1}{3}\cos 60° \end{bmatrix}\begin{pmatrix} x \\ y \end{pmatrix} + \begin{pmatrix} \frac{1}{2} \\ \frac{1}{2}\sin 60° \end{pmatrix}, \tag{3}$$

$$W_4\begin{pmatrix} x' \\ y' \end{pmatrix} = \begin{bmatrix} \frac{1}{3} & 0 \\ 0 & \frac{1}{3} \end{bmatrix}\begin{pmatrix} x \\ y \end{pmatrix} + \begin{pmatrix} \frac{2}{3} \\ 0 \end{pmatrix}. \tag{4}$$

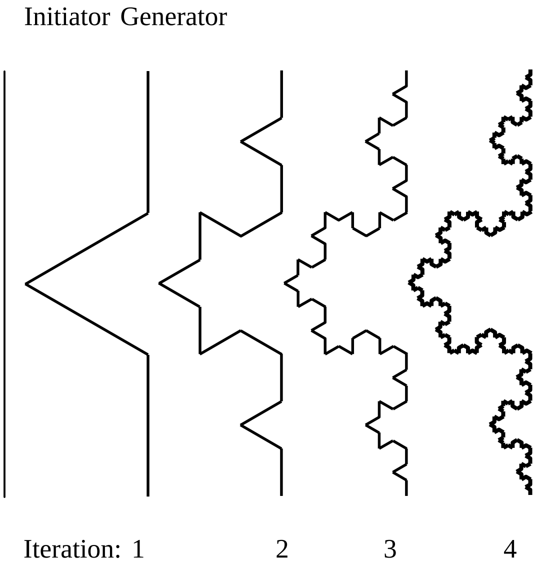

Fig. 1. Geometrical construction of standard Koch curve (indentation angle=60°).

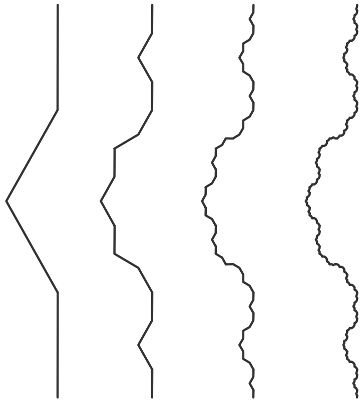

Fig. 2. A recursive generalization based on fractal Koch curves of first four iterations with an identical indentation angle of 30° for various stages.

The generator is then obtained as

$$A_1 = W(A) = W_1(A) \cup W_2(A) \cup W_3(A) \cup W_4(A). \tag{5}$$

This process can be repeated for all higher iterations of the geometry. It may be observed that the (straight line) distance between the start and end points of curves of all iterations is the same. Various iterations of the geometry obtained with this IFS are shown in Fig. 1.

2.2. Recursive Generalizations

In the proposed generalizations studied as part of this work, the rotation (indentation) angle is made a variable. This leads to generalization of IFS with the following transformations

$$W_1\begin{pmatrix} x' \\ y' \end{pmatrix} = \begin{bmatrix} \frac{1}{s} & 0 \\ 0 & \frac{1}{s} \end{bmatrix}\begin{pmatrix} x \\ y \end{pmatrix}, \tag{6}$$

$$W_2\begin{pmatrix} x' \\ y' \end{pmatrix} = \begin{bmatrix} \frac{1}{s}\cos\theta & -\frac{1}{s}\sin\theta \\ \frac{1}{s}\sin\theta & \frac{1}{s}\cos\theta \end{bmatrix}\begin{pmatrix} x \\ y \end{pmatrix} + \begin{pmatrix} \frac{1}{s} \\ 0 \end{pmatrix}, \tag{7}$$

$$W_3\begin{pmatrix} x' \\ y' \end{pmatrix} = \begin{bmatrix} \frac{1}{s}\cos\theta & \frac{1}{s}\sin\theta \\ -\frac{1}{s}\sin\theta & \frac{1}{s}\cos\theta \end{bmatrix}\begin{pmatrix} x \\ y \end{pmatrix} + \begin{pmatrix} \frac{1}{2} \\ \frac{1}{s}\sin\theta \end{pmatrix}, \tag{8}$$

$$W_4\begin{pmatrix} x' \\ y' \end{pmatrix} = \begin{bmatrix} \frac{1}{s} & 0 \\ 0 & \frac{1}{s} \end{bmatrix}\begin{pmatrix} x \\ y \end{pmatrix} + \begin{pmatrix} \frac{s-1}{s} \\ 0 \end{pmatrix}, \tag{9}$$

where the scale factor *s* is angle dependent and is given by

$$\frac{1}{s} = \frac{1}{2(1+\cos\theta)}. \tag{10}$$

This ensures the distance between the start and end points for all iterations is the same. It may be easily verified that this formulation degenerates to the standard Koch curve for θ=60°.

The generator for the geometry can be obtained as in eq. (5). These affine transformations in the generalized case also lead to a self-similar fractal geometry. As an example, self-similar geometries of various iterations obtained by recursively applying the above transformations have been shown in Fig. 2. The indentation angle in these cases is 30°, as compared to 60° used for the standard Koch curve geometry. In fact this variation in indentation angle causes a corresponding variation in the fractal dimension of the geometry. The fractal similarity dimension of this generalization of the geometry is obtained as

$$D = \frac{\log 4}{\log[2(1+\cos\theta)]}. \tag{11}$$

Similar geometries with varying fractal similarity dimensions can be obtained for different indentation angles with this recursive generalization. The indentation angle may vary between 0 and 90°. For the indentation angle θ=0, the curve is linear (dimension=1) while for θ=90°, a geometry of sufficiently large iteration tends to fill a triangular area (dimension=2).

2.3. Non-recursive Generalizations

The indentation angle and the scale factor for all stages of iteration are kept the same in the recursive generalization described above. Further generalized curves can be obtained by removing this restriction and are used in the study presented in this paper. In order to ensure that the approach is systematic, all sub-sections of the curve are kept identical. Thus all line segments of the final geometry have the same length, and indentation angles for subsections of the geometry at individual iteration are identical. Such generalizations of a third iterated Koch curve are shown in Fig. 3. The indentation angle for iteration stages are 20°, 40°, and 60°, with the last angle used in the outermost generator for case (c) and vice versa for case (d). For a given end-to-end distance l, the length of individual line segments m constituting an n^{th} iterated geometry is given by

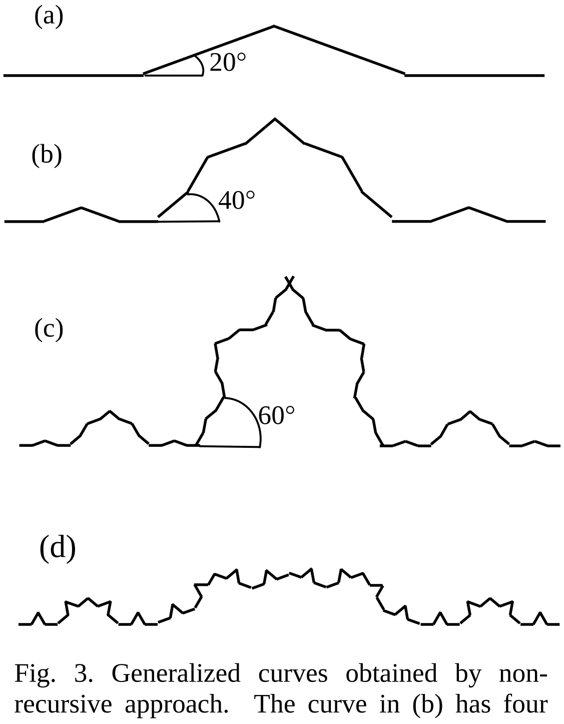

Fig. 3. Generalized curves obtained by non-recursive approach. The curve in (b) has four copies of the one in (a), but with a different indentation angle. Similarly the curves in (c) is obtained from (b). Two such 3rd iterated curvs are compared in (c) and (d). Indentation angles are: (c) 20°-40°-60° (d) 60°-40°-20°. The angle for the first generator listed first.

$$m = \frac{l}{2^n \prod_{i=1}^{n} \left(1 + \cos\theta_i\right)} . \qquad (12)$$

Likewise, the total unfolded length of the curve is given by

$$L = \frac{2^n l}{\prod_{i=1}^{n} \left(1 + \cos\theta_i\right)} . \qquad (13)$$

It may be observed that for a given l, various permutations of angles can result in the same unfolded length. Thus this generalization offers a possibility of studying the effects of indentation angles, as opposed to unfolded length.

3. MODELING STUDIES ON THE ANTENNA

3.1. Dipole Antenna Model

Dipole antennas with arms consisting of Koch curves of different indentation angles and fractal iterations are simulated using a moment method based software G-NEC. A typical dipole antenna using 4th order iteration curves with an indentation angle of 60° and with the feed located at the center of the geometry is shown in Fig. 4. Similar geometries with various fractal iterations and indentation angles have been extensively studied by numerical simulations [33]. This model consists of wire elements only. The radius of wire segments constituting the antenna model is consistently kept at 0.1 mm. It may be noted that this values is much smaller than the wavelength (~60 mm) at the highest frequency considered in the present study. The segmentation length used in the NEC model is taken as approximately 0.5 mm, uniform in all cases. Each dipole arm has an end-to-end distance of 10 cm.

3.2. Numerical Simulations of Antennas with Self-Similar Geometry

Characteristics of antennas using the standard Koch curve of this type have been studied previously by experiments as well as numerical

Table 1. Primary (first) resonant frequencies for dipole antennas with self-similar Koch curves (with recursive IFS) for various iterations obtained by numerical simulations. The end-to-end distance of these arms are kept constant at 0.1 m.

Indentation Angle (Deg.)	Unfolded arm length (m) for various iterations				Resonant frequencies (MHz) for various iterations			
	1	2	3	4	1	2	3	4
10	0.101	0.102	0.102	0.103	710.1	713.5	711.7	710.1
20	0.103	0.106	0.116	0.113	685.8	693.9	687.8	685.8
30	0.107	0.115	0.123	0.132	643.2	662.4	649.6	643.2
40	0.113	0.128	0.145	0.164	589.1	618.8	595.1	589.1
50	0.122	0.148	0.18	0.22	512.5	565.6	528.6	512.5
60	0.133	0.178	0.237	0.316	427.9	505.1	453.8	427.9
70	0.149	0.222	0.331	0.493	337.2	441.2	376	337.2
80	0.170	0.290	0.495	0.843	256.6	381.3	304.6	256.6

simulations [22]-[27]. Since these antennas are small in terms of operational wavelength, their radiation performance is not expected to change significantly. Hence only the input characteristics of these antennas are examined in the following discussions.

Resonant frequencies for antennas with various iterations of self-similar geometry have been listed in Table 1. This indicates that by changing the indentation angle or fractal iteration, the resonant frequency can be reduced. However this reduction in resonant frequency may as well be attributed to the increase in the unfolded length of the curve. In contrast to previous designs using a genetic algorithm [28]-[29], the present approach strives to generate a knowledge base using geometrical features and hence is expected to be less computation intensive.

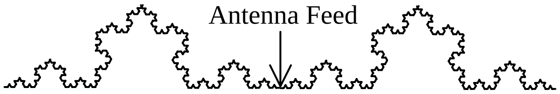

Fig. 4. Configuration of Koch dipole antenna. Arms of the antenna have 4th iteration Koch curves with indentation angle=60°.

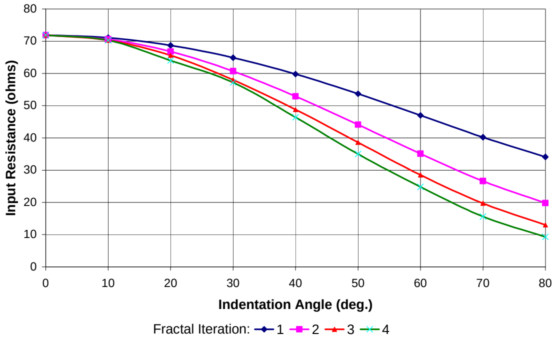

Fig. 5. Variation of input resistance of the dipole antennas with generalized Koch curves (self-similar) of various fractal iterations.

The input resistance at the resonant frequency also changes by these modifications to the standard geometry. In Fig. 5, these variations are plotted for various iterations of the fractal. For angle θ=0, these antennas all degenerate to identical linear dipoles with a resonant input resistance of about 72Ω. As the angle or the fractal iteration is increased, this value is reduced significantly. It may be observed that it is always preferable to match the antenna impedance to a standard value (50Ω). Although not attempted in this paper, this approach of generalization may be used to design antennas with the required input characteristics at a specified frequency. In other words, the indentation angle may be used as a design parameter.

The antenna input characteristics at higher resonant frequencies are also altered by the change in angles. To compare these, the variations of first four resonant frequencies are plotted in Fig. 6 for the first four iterations of the geometry. It may be noticed that for very small indentation angles, these antennas behave similar to linear dipoles. However as the angle is increased, the periodicity of these multiple resonances is changed. It may be argued that the indentation angle of the self-similar antenna can be changed for appropriate positioning of its resonant frequencies.

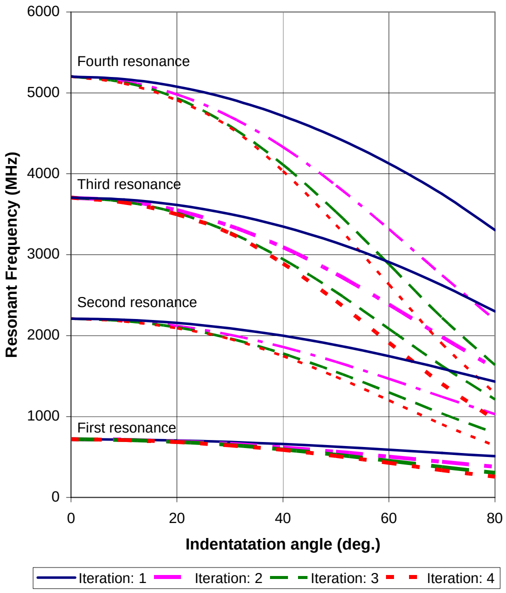

Fig. 6. Variation of resonant frequencies of dipole antennas with generalized self-similar Koch curves of various fractal iterations. The resonant frequencies for each resonance of all cases converge to that of linear dipole when the indentation angle approaches zero.

3.3. Numerical Simulations of Antennas with Non-Recursive Geometry

The geometries used thus far were all generated recursively by using an IFS. If one were to break this rule, antenna properties may be tailored with better flexibility. Although the resulting antenna structure may not be called truly fractal, this offers the possibility of studying curves with the same unfolded length, but with different sets of angles for various iterations. Extensive numerical simulation studies have been performed on antennas using such non-recursive geometries to explore the usefulness of indentation angle, contrary to the unfolded length, as the primary parameter. A few representative cases are presented here.

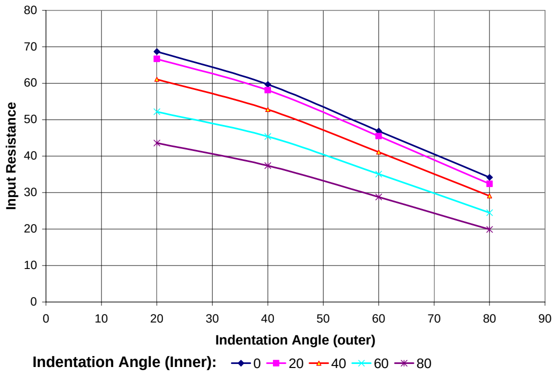

Fig. 7. Input resistance at the first (primary) resonance of dipole antennas based on generalized Koch curves. In all antennas, end-to-end distance of their arms are kept constant at 0.1 m, and have 2nd generation non-recursive Koch curve. The angle at the inner iteration is the parametric variation while the x-axis is for the angle of the outer stage.

In Table 2 the unfolded length of arms of the dipole and the resulting primary resonant frequency are listed. As mentioned earlier, permutations of indentation angles, such as (20°, 40°) and (40°, 20°) lead to the same unfolded length, but different resonant frequencies. This shows that having identical unfolded length does not guarantee similar input characteristics of the antenna. Furthermore a consistent variation in the input resistance of the antenna at its primary resonance is also observed. These are plotted for various indentation angles in Fig. 7. Similarly, the variation in the periodicity of distribution of first four resonant frequencies of various antenna geometries can be observed from Table 3. Thus if one has the flexibility of arbitrarily choosing the indentation angle at each stage of generation of the

Table 2. Unfolded curve length and resonant frequencies for various indentation angles of the non-recursive generalization of the 2nd iterated Koch curve. The end-to-end distance of its arms are kept constant at 0.1 m.

Indentation angle (inner)	Unfolded Curve-Length (m) for various (outer) Indentation angles				Resonant Frequencies (MHz) for (outer) Indentation angles			
	20°	40°	60°	80°	20°	40°	60°	80°
20°	0.106	0.117	0.137	0.176	694	662	610	554
40°	0.117	0.128	0.151	0.193	650	619	570	515
60°	0.137	0.151	0.178	0.227	580	550	505	455
80°	0.176	0.193	0.227	0.290	497	469	427	382

Table 3. Resonant frequencies of dipole antennas with 2nd generation generalized non-recursive Koch curves. The indentation angle in each generation stage is different. The end-to-end distance of these arms are kept constant at 0.1 m.

Indentation Angles		Input Resistance at f_{r1}	Resonant Frequencies (MHz)				Ratios of Resonant Frequencies		
Inner	Outer		f_{r1}	f_{r2}	f_{r3}	f_{r4}	f_{r2}/f_{r1}	f_{r3}/f_{r2}	f_{r4}/f_{r3}
0	20	68.7	705	2157	3615	5078	3.060	1.676	1.405
	40	59.7	660	1999	3348	4716	3.029	1.675	1.409
	60	46.9	590	1748	2910	4130	2.963	1.665	1.419
	80	34.2	511	1432	2300	3311	2.802	1.606	1.440
20	20	66.7	694	2121	3549	4981	3.056	1.673	1.403
	40	58.1	650	1964	3284	4621	3.022	1.672	1.407
	60	45.5	580	1714	2847	4035	2.955	1.661	1.417
	80	32.4	497	1395	2247	3236	2.807	1.611	1.440
40	20	61.1	662	2012	3354	4690	3.039	1.667	1.398
	40	52.8	619	1861	3093	4332	3.006	1.662	1.401
	60	41.1	550	1619	2666	3748	2.944	1.647	1.406
	80	29.1	469	1308	2093	2991	2.789	1.600	1.429
60	20	52.2	610	1839	3043	4221	3.015	1.655	1.387
	40	45.4	570	1696	2792	3870	2.975	1.646	1.386
	60	35.1	505	1468	2386	3317	2.907	1.625	1.390
	80	24.5	427	1177	1858	2619	2.756	1.579	1.410
80	20	43.6	554	1648	2689	3663	2.975	1.632	1.362
	40	37.4	515	1513	2451	3336	2.938	1.620	1.361
	60	28.8	455	1299	2075	2828	2.855	1.597	1.363
	80	19.9	382	1031	1599	2194	2.699	1.551	1.372

curve, antennas with varied input characteristics can be obtained.

Similar variations in input characteristics are also obtained for antennas with 3rd iteration geometries. Resonant frequencies of antenna geometries with various permutations of indentation angles, with the innermost angle kept constant at 60° are listed in Table 4.

Following this approach one can have several curves with the same length, but with a different set of resonant frequencies. These differences in resonant frequencies are found to be more pronounced as the order of iteration is increased. Hence this approach offers a scheme of designing antennas based on Koch curves suiting the requirements in terms of both the input resistance and the resonant frequency. It is concluded from this study one can design multi-resonant antennas with considerable flexibility by choosing their indentation angles arbitrarily for each iteration while generating the geometry.

4. CONCLUSIONS

In this paper, the variation in the input characteristics of multi-resonant antennas based on generalizations of fractal Koch curves is presented. Geometries considered here include both recursive and non-recursive curves. Schemes for such generalization of these geometries are introduced. In this study, the indentation angle in the transformations of the iterated function system is varied to obtain a set of geometries. Although this variation has a direct bearing on the unfolded length of the curve, the indentation angle should be considered a primary variable since several geometries with the same unfolded length can be constructed with different permutations of indentation angles. Antenna parameters such as the primary resonant frequency, the input resistance at this resonance, and ratios of the first few resonant frequencies have been studied by numerical simulations. This study shows that it is possible to design multi-resonant antennas using Koch curves by individually choosing an optimum indentation angle for various iteration stages of the

Table 4. Resonant frequencies of 3rd iterated non-recursive geometry. The innermost angle is kept $\theta_1 = 60°$. The other angles are varied as listed.

θ_2	θ_3	Input resistance at f_{r1}	Resonant Frequencies (MHz)				Ratios of Resonant Frequencies		
			f_{r1}	f_{r2}	f_{r3}	f_{r4}	f_{r2}/f_{r1}	f_{r3}/f_{r2}	f_{r4}/f_{r3}
0	20	57.5	649	1968	3281	4589	3.032	1.667	1.399
	40	49.6	605	1815	3017	4223	3.000	1.662	1.400
	60	38.6	537	1571	2582	3632	2.926	1.644	1.407
	80	27.2	456	1261	1995	2848	2.765	1.582	1.428
20	20	55.7	638	1932	3215	4491	3.028	1.664	1.397
	40	48.2	595	1780	2952	4129	2.992	1.658	1.399
	60	37.1	526	1539	2523	3547	2.926	1.639	1.406
	80	25.7	443	1229	1952	2798	2.774	1.588	1.433
40	20	50.4	605	1822	3018	4194	3.012	1.656	1.390
	40	43.4	563	1677	2762	3841	2.979	1.647	1.391
	60	33.3	497	1445	2349	3285	2.907	1.626	1.398
	80	23.1	417	1150	1816	2586	2.758	1.579	1.424
60	20	42.6	553	1646	2697	3709	2.976	1.639	1.375
	40	36.4	513	1509	2457	3380	2.942	1.628	1.376
	60	27.8	451	1294	2077	2870	2.869	1.605	1.382
	80	19	376	1023	1598	2234	2.721	1.562	1.398
80	20	33.7	489	1428	2295	3099	2.920	1.607	1.350
	40	29.1	454	1307	2087	2818	2.879	1.597	1.350
	60	22	397	1113	1753	2369	2.804	1.575	1.351
	80	14.8	328	871	1335	1820	2.655	1.533	1.363

underlying fractal geometry. Identifying similar parameters for other known fractal geometries would ease the complexity in designing multiband and multifunctional antennas for modern wireless applications.

REFERENCES

[1] B.B. Madelbrot, *The Fractal Geometry of Nature*, New York: W.H. Freeman, 1983.

[2] H.-O. Peitgen, J.M. Henriques, L.F. Penedo (Eds.), *Fractals in the Fundamental and Applied Sciences*, Amsterdam: North Holland, 1991.

[3] G.P. Cherepanov, A.S. Balankin, and V.S. Ivanova, “Fractal fracture mechanics,” *Engineering Fracture Mechanics*, vol. 51, pp. 997-1033, 1995.

[4] J.H. Jeng, V.V. Varadan, and V.K. Varadan, “Fractal finite element mesh generation for vibration problems,” *J. Acous. Soc. Amer.*, vol. 82, pp. 1829-1833, 1987.

[5] A.E. Jacquin, “Fractal image coding: A review,” *Proc. IEEE*, vol. 81, pp. 1451-1465, 1993.

[6] A. Lakhtakia, N.S. Holter, V.K. Varadan, and V.V. Varadan, “Self-similarity in diffraction by a self-similar fractal screen,” *IEEE Trans. Ant. Propagat.*, vol. 35, pp. 236-239, 1987.

[7] D.L. Jaggard, “Fractal electrodynamics: From super antennas to superlattices,” in *Fractals in Engineering*, Springer, pp. 204-221, 1997.

[8] J. Romeu and Y. Rahmat-Samii, “Dual band FSS with fractal elements,” *Electron. Lett.*, vol. 35, pp. 702-703, 1999.

[9] D.H. Werner and D. Lee, “Design of dual-polarised multiband frequency selective surfaces using fractal elements,” *Electron. Lett.*, vol. 36, pp. 487-488, 2000.

[10] J. Romeu and Y. Rahmat-Samii, “Fractal FSS: a novel dual-band frequency selective surface,” *IEEE Trans. Ant. Propagat.*, vol. 48, pp. 1097-1105, 2000.

[11] D.H. Werner, R.L. Haupt, and P.L. Werner, “Fractal antenna engineering: The theory and design of fractal antenna arrays,” *IEEE Ant. Propagat. Mag.*, vol. 41, no. 5, pp. 37-59, 1999.

[12] D.H. Werner, P.L. Werner, D.L. Jaggard, A.D. Jaggard, C.Puente, and R.L. Haupt, "The theory and design of fractal antenna arrays," in *Frontiers in Electromagnetics*, D.H. Werner and R. Mittra (Eds.), New York: IEEE Press, pp. 94-203, 1999.

[13] D.H. Werner, P.L. Werner, and A.J. Ferraro, "Frequency independent features of self-similar fractal antennas," IEEE AP-S Inter. Symp. 1996, pp. 2050-2053, 1996.

[14] N. Cohen, "Fractal antenna applications in wireless telecommunications," in Professional Program Proc. of Electronics Industries Forum of New England, 1997, IEEE, pp. 43-49, 1997.

[15] C. Puente, J. Claret, F. Sagues, J. Romeu, M.Q. Lopez-Salvans and R Pous, "Multiband properties of a fractal tree antenna generated by electrochemical deposition," *Electron. Lett.*, vol. 32, pp. 2298-2299, 1996.

[16] C. Puente, J. Romeu, R. Bartoleme, and R. Pous, "Fractal multiband antenna based on Sierpinski gasket," *Electron. Lett.*, vol. 32, pp. 1-2, 1996.

[17] D.H. Werner, A. Rubio Bretones, and B.R. Long, "Radiation characteristics of thin-wire ternary fractal trees," *Electron. Lett.*, vol. 35, pp. 609-610, 1999.

[18] M. Sindou, G. Ablart and C. Sourdois, "Multiband and wideband properties of printed fractal branched antennas," *Electron. Lett.*, vol. 35, pp. 181-182, 1999.

[19] X. Liang and. M.Y.W. Chia, "Multiband characteristics of two fractal antennas," *Microw. Opt. Technol. Lett.*, vol. 23, pp. 242-245, 1999.

[20] C. Puente, M. Navarro, J. Romeu, and R. Pous, "Variations on the fractal Sierpinski antenna flare angle," IEEE AP-S Inter. Symp., pp. 2340-2343, 1998.

[21] M. Navarro, J.M. Gonzalez, C. Puente, J. Romeu, and A. Aguasca, "Self-similar surface current distribution on fractal Sierpinski antenna verified with infra-red thermograms," IEEE AP-S Inter. Symp., pp. 1566-1569, 1999.

[22] C. Puente-Baliarda, J. Romeu, R. Pous, J. Ramis, and A. Hijazo, "Small but long Koch fractal monopole," *Electron. Lett.*, vol. 34, pp. 9-10, 1998.

[23] C.P. Baliarda, J. Romeu, and A. Cardama, "The Koch monopole: A small fractal antenna," *IEEE Trans. Ant. Propagat.*, vol. 48 pp. 1773-1781, 2000.

[24] J.P. Glanvittorio and Y. Rahmaat-Samii, "Fractal element antennas: A compilations of configurations with novel characteristics," IEEE AP-S Inter. Symp. 2000, pp. 1688-1691, 2000.

[25] S.R. Best, "On the resonant behavior of the small Koch fractal monopole antenna," *Microw. Opt. Technol. Lett.*, vol. 35, pp. 311-315, 2002.

[26] S.R. Best, "On the multiband behavior of the Koch fractal monopole antenna," *Microw. Opt. Technol. Lett.*, vol. 35, pp. 371-374, 2002.

[27] S.R. Best, "On the performance of the Koch fractal and other bent wire monopoles as electrically small antennas," IEEE AP-S Inter. Symp. 2002, vol. 4, pp. 534-537, 2002.

[28] D.H. Werner, P.L. Werner and K.H. Church, "Genetically engineered multiband fractal antennas," *Electron. Lett.*, vol. 37, pp. 1150-1151, 2001.

[29] D.H. Werner, P.L. Werner K.H. Church, J.W. Culver, and S.D. Eason, "Genetically engineered dual-band fractal antennas," IEEE AP-S Inter. Symp. 2001, Vol. 3, pp. 628-631, 2001.

[30] K.J. Vinoy, K.A. Jose, V.K. Varadan, and V.V. Varadan, "Resonant frequency of Hilbert curve fractal antennas," in: IEEE AP-S Inter. Symp., vol. 3, pp. 648-651, 2001.

[31] K.J. Vinoy, K.A. Jose, and V.K. Varadan, "On the relationship between fractal dimension and the performance of multi-resonant dipole antennas using Koch curves," *IEEE Trans. Antennas Propagat.* Accepted for publication (Oct 2003).

[32] K.J. Vinoy, K.A. Jose, and V.K. Varadan, "Multiband characteristics and fractal dimension of dipole antennas with Koch curve geometry," IEEE AP-S Inter. Symp., 2002.

[33] K.J. Vinoy, "Fractal shaped antenna elements for wide- and multi-band wireless applications," Ph.D. Dissertation. Pennsylvania State University, 2002.

[34] H.O. Peitgen, H. Jurgens, and D. Saupe, *Chaos and Fractals: New Frontiers of Science*, New York: Springer-Verlag, 1992.

K.J. Vinoy received Bachelors degree from the University of Kerala, India, Masters degree from Cochin University of Science and Technology, India and Ph.D. degree from the Pennsylvania State University in 1990, 1993, and 2002, respectively. From 1994 to1998 he worked in the computational electromagnetics group at National Aerospace Laboratories, Bangalore, India. He was a research assistant at the Center for the Engineering of Electronic and Acoustic Materials and Devices (CEEAMD) at the Pennsylvania State University, from 1999 to 2002. Presently he is continuing there for Post Doctoral research. His research interests include fractal shaped antennas, RF-MEMS, micromachined antennas, and computational electromagnetics. He has published over 30 papers in technical journals and conferences. His publications include two books: *Radar Absorbing Materials: From Theory to Design and Characterization*, (Boston: Kluwer, 1996) and *RF MEMS and their Applications* (London: John Wiley, 2002). He also holds one US patent.

Jose K. Abraham received Ph.D. degree from Cochin University of Science and Technology, India in 1989. From 1990 to 1997 he worked as a Lecturer at Cochin University of Science and Technology, India and was involved with the development of superconducting antennas, radar absorbing materials and wideband microstrip antennas. He joined theCenter for the Engineering of Electronic and Acoustic Materials at Pennsylvania State University in 1997. Currently he is an Assistant Professor of Engineering Science and Mechanics Department. He has published 100 papers in technical Journals and conferences and published a book. He holds two patents. His current research interests include RF MEMS, microwave material characterization, RF wireless sensors and smart antennas.

Vijay K. Varadan received his Ph.D. degree from Northwestern University in 1974. After serving on the faculty of Cornell University and Ohio State University, he joined the Pennsylvania State University in 1983 where he is currently an alumni distinguished professor of engineering science and electrical engineering. He is involved in all aspects of wave-material interaction, optoelectronics, microelectro-nics, microelectromechanical systems (MEMS), smart materials and structures, sonar-, radar-, microwave-, and optically absorbing composite media, FSS, Nanotechnology, Carbon nanotubes, Fuel cells and button cell batteries, EMI shielding materials and piezoelectric, chiral, ferrite, and polymer composites, tunable ceramics materials, and electronically steerable antennas. He is also interested in microwave and ultrasonic experiments to measure the dielectric, magnetic, mechanical and optical properties of composites. He is an Editor of the journal of the Wave-Material Interaction and the Editor-in-Chief of the Journal of Smart Materials and Structures. He has published more than 400 Journal and 300 Proceedings papers and 9 books. He has 10 patents awarded and two pending. He is the Director of the Center for the Engineering of Electronic and Acoustic Materials and Devices. The Center is supported by industries around the world and Government Agencies.

Iterative Solution to the Multiple Scattering by A System of Two Infinitely Long Conducting Strips

A-K. Hamid
Department of Electrical and Computer Eng.
University of Sharjah
P.O. Box 27272, Sharjah, U.A.E
email: akhamid@Sharjah.ac.ae

M. I. Hussein
Department of Electrical Engineering
United Arab Emirates University
P.O. Box 17555, Al-Ain, United Arab Emirates
email: MIHussein@uaeu.ac.ae

Abstract

An analytic solution to the problem of a plane electromagnetic wave scattering by two infinitely long conducting strips is presented using an iterative procedure to account for the multiple scattered field between the strips. To compute the higher order terms of the scattered fields, the translation addition theorem for Mathieu functions is implemented to express the field scattered by one strip in terms of the elliptic coordinate system of the other strip in order to impose the boundary conditions. Scattered field coefficients of high order fields are obtained and written in matrix form. Numerical results are plotted for the scattered in far zone for different strip widths, electrical separations and angles of incidence.

1. Introduction

The multiple scattering of a plane electromagnetic wave by a system of infinitely long conducting strips is important in a variety of practical applications. For example, the solution may be used to study the scattering by complex bodies modeled by a collection of strips, prediction of radiation from elliptical reflector antennas, and to check the accuracy of the results of numerical and approximate methods [1].
Exact analytic solution of the problem of scattering by a system of *N* conducting strips has been formulated using the translation addition theorem for Mathieu functions to enforce the boundary condition [1]. The required computer time and memory to invert the resulting system of matrix increase rapidly with the number of strips. In addition, numerical results for certain strips dimensions, electrical separations and angles of incidence are difficult to obtain by this analytical method may be due to the associated ill-condition system matrices.
In the present paper an iterative procedure is proposed to the scattering by an arbitrary oriented two infinitely long conducting strips. This approach requires the solution of the scattered field by each strip, assumed to be alone in the incident field that acts as an incident field on the other strip. Therefore, the first order scattered field results from the excitation of each strip by the incident field only, while the second order scattered field results from the excitation of each strip by the first order scattered field. Hence, this iterative procedure continues until the solution convergence. One of the advantages of the iterative procedure is that the proposed solution does not require matrix inversion and therefore the desired scattered field coefficients are obtained after each iteration and used in the subsequent iteration.
The solution of the electromagnetic scattering by a system of *N* infinitely long conducting strips has received little attention in the literature due to the complexity of computing Mathieu functions of higher orders and its associated translation addition theorem. Recently, there have been many studies on the multiple scattering by strips [1], circular or elliptic cylinders [2]-[6], spheres [7], and spheroids [8], [9] using different techniques.
Numerical results showing the number of scattered fields are plotted for the normalized echo pattern width with various electrical separations, widths, angles of incidence, and also compared with published results to demonstrate the efficiency of the method [1].

2. Formulation of the problem

Fig. 1 shows the scattering geometry of two infinitely long conducting strips with different widths and arbitrary orientation. The center axes of the two strips are assumed to be parallel to the z-axes. The first strip is located at the origin o_1 while the second strip is located at the polar coordinate point (d, γ) with respect to the global coordinate system (x,y,z). The width of the strips are a_1 and a_2 respectively, and each strip's local coordinate system makes angle α_1 for the first strip and α_2 for the second strip with its global coordinate system. Consider elliptic coordinate systems *u, v,* and *z* such that

$$x = F\cosh u \cos v, \quad y = F\sinh u \sin v, \quad z = z \tag{1}$$

where F is the semifocal length, $0 \le u < \infty$, $0 \le v < 2\pi$, and $-\infty \le z < \infty$. It is usually convenient to introduce

$$\xi = \cosh u \quad , \quad \eta = \cos v \tag{2}$$

1054-4887 © 2004 ACES

with $1 \le \xi \le \infty$ and $-1 \le \eta \le 1$.

Consider the case of a linearly polarized electromagnetic plane wave incident on the two infinitely long conducting strips at an angle ϕ_i with respect to the positive x axis, as shown in Fig. 1, with e^{jwt} time dependence. The electric field component of the TM polarized plane wave of amplitude E_0 is given by

$$E_z^i = E_0 e^{jk\rho\cos(\phi-\phi_i)} \tag{3}$$

where k is the wave number in free space. The incident electric field may be expressed in terms of Mathieu functions about the origins o_1 and o_2 and as follows [10]

$$E_{1z}^i = \sum_{m=0}^{\infty} A_{1em} R_{em}^{(1)}(c_1,\xi_1) S_{em}(c_1,\eta_1) + \sum_{m=1}^{\infty} A_{1om} R_{om}^{(1)}(c_1,\xi_1) S_{om}(c_1,\eta_1) \tag{4}$$

$$E_{2z}^i = \sum_{m=0}^{\infty} A_{2em} R_{em}^{(1)}(c_2,\xi_2) S_{em}(c_2,\eta_2) + \sum_{m=1}^{\infty} A_{2om} R_{om}^{(1)}(c_2,\xi_2) S_{om}(c_2,\eta_2) \tag{5}$$

where

$$A_{1\substack{em\\om}} = E_0 j^m \frac{\sqrt{8\pi}}{N_{\substack{em\\om}}(c_1)} S_{\substack{em\\om}}(c_1, \cos\phi_i^1) \tag{6}$$

$$A_{2\substack{em\\om}} = E_0 j^m \frac{\sqrt{8\pi}}{N_{\substack{em\\om}}(c_2)} S_{\substack{em\\om}}(c_2, \cos\phi_i^2)\, e^{jkd\cos(\gamma-\phi_i)} \tag{7}$$

$$N_{\substack{em\\om}}(c_1) = \int_0^{2\pi} [S_{\substack{em\\om}}(c_1,\eta_1)]^2\, dv \tag{8}$$

$$N_{\substack{em\\om}}(c_2) = \int_0^{2\pi} [S_{\substack{em\\om}}(c_2,\eta_2)]^2\, dv \tag{9}$$

$$\phi_i^1 = \phi_i - \alpha_1, \quad \phi_i^2 = \phi_i - \alpha_2 \tag{10}$$

and $c_1 = k\,F_1$, $c_2 = k\,F_2$, S_{em} and S_{om} are the even and odd angular Mathieu functions of order *m*, respectively, $R_{em}^{(1)}$ and $R_{om}^{(1)}$ are the even and odd radial Mathieu functions of the first kind, and N_{em} and N_{om} are the even and odd normalized functions.

The scattered electric field from the conducting strips can be expressed in terms of Mathieu functions as

$$E_{1z}^S = \sum_{m=0}^{\infty} B_{em} R_{em}^{(4)}(c_1,\xi_1) S_{em}(c_1,\eta_1) + \sum_{m=1}^{\infty} B_{om} R_{om}^{(4)}(c_1,\xi_1) S_{om}(c_1,\eta_1) \tag{11}$$

$$E_{2z}^S = \sum_{m=0}^{\infty} C_{em} R_{em}^{(4)}(c_2,\xi_2) S_{em}(c_2,\eta_2) + \sum_{m=1}^{\infty} C_{om} R_{om}^{(4)}(c_2,\xi_2) S_{om}(c_2,\eta_2) \tag{12}$$

where B_{em}, C_{em}, B_{om}, and C_{om} are the unknown even and odd scattered field expansion coefficients, and $R_{em}^{(4)}$ and $R_{om}^{(4)}$ are the even and odd Mathieu functions of the fourth kind.

3. First Order Scattered Field by Strips

The first order scattered field results from the separate excitation of each strip by the incident plane wave alone. The boundary condition at the surface of first strip requires the tangential components of the total electric field to be zero, i.e.,

$$\begin{aligned}
&\sum_{m=0}^{\infty} A_{1em} R_{em}^{(1)}(c_1,1) S_{em}(c_1,\eta_1) + \sum_{m=1}^{\infty} A_{1om} R_{om}^{(1)}(c_1,1) S_{om}(c_1,\eta_1) \\
&+ \sum_{m=0}^{\infty} B_{em}^1 R_{em}^{(4)}(c_1,1) S_{em}(c_1,\eta_1) + \sum_{m=1}^{\infty} B_{om}^1 R_{om}^{(4)}(c_1,1) S_{om}(c_1,\eta_1) = 0
\end{aligned} \tag{13}$$

where B_{em}^1 and B_{om}^1 are the first order scattered field expansion coefficients. A similar equation may be written corresponds to the second strip. Using the orthogonality properties of the angular Mathieu function yields the first order scattered field coefficients, which may be written for each strip in matrix form as

$$\begin{bmatrix} B_{em}^1 \\ B_{om}^1 \end{bmatrix} = \begin{bmatrix} Q_{enm}^{11} & 0 \\ 0 & Q_{onm}^{11} \end{bmatrix} \begin{bmatrix} A_{1em} \\ A_{1om} \end{bmatrix} \tag{14}$$

$$\begin{bmatrix} C_{em}^1 \\ C_{om}^1 \end{bmatrix} = \begin{bmatrix} Q_{enm}^{22} & 0 \\ 0 & Q_{onm}^{22} \end{bmatrix} \begin{bmatrix} A_{2em} \\ A_{2om} \end{bmatrix} \tag{15}$$

where C^1_{em} and C^1_{om} are the first order scattered field coefficients of the strip, and

$$Q^{11}_{enm} = \frac{R^{(1)}_{en}(c_1,1)}{R^{(4)}_{en}(c_1,1)} \quad , \quad Q^{11}_{onm} = \frac{R^{(1)}_{on}(c_1,1)}{R^{(4)}_{on}(c_1,1)} \tag{16}$$
$$= 0\ ,\ n \neq m \qquad , \qquad = 0\ ,\ n \neq m$$

Similar equations may be written correspond to Q^{22}_{enm} and Q^{22}_{onm}.

4. Higher Order Scattered Field by Strips

The second order field results from the excitation of each strip by the scattered field from the other strip due to the initial incident field. The boundary condition at the surface of first strip requires the tangential components of the total electric field to be zero, i.e,

$$\begin{aligned}
&\sum_{m=0}^{\infty} C^1_{enm}\ R^{(4)}_{em}(c_2,1\ )S_{em}(c_2,\eta_2) \\
&+ \sum_{m=1}^{\infty} C^1_{onm}\ R^{(4)}_{om}(c_2,1)S_{om}(c_2,\eta_2) \\
&+ \sum_{m=0}^{\infty} B^2_{em} R^{(4)}_{em}(c_1,1)S_{em}(c_1,\eta_1) \\
&+ \sum_{m=1}^{\infty} B^2_{om}\ R^{(4)}_{om}(c_1,1)S_{om}(c_1,\eta_1) = 0
\end{aligned} \tag{17}$$

where B^2_{em} and B^2_{om} are the second order scattered field expansion coefficients of the first strip. To enforce the boundary condition, the first order scattered field from the second strip must be expressed in terms of the coordinate systems of the first strip by using the addition theorem for the Mathieu functions [11], i.e.,

$$\begin{aligned}
R^{(4)}_{\substack{em\\om}}(c_2,\xi_2)S_{\substack{em\\om}}(c_2,\eta_2) &= \sum_{l=0}^{\infty} WE^{2\rightarrow 1}_{\substack{elm\\olm}} R^{(1)}_{el}(c_1,\xi_1)S_{el}(c_1,\eta_1) \\
&+ \sum_{l=1}^{\infty} WO^{2\rightarrow 1}_{\substack{elm\\olm}} R^{(1)}_{ol}(c_1,\xi_1)S_{ol}(c_1,\eta_1)
\end{aligned} \tag{18}$$

where

$$WE^{2\rightarrow 1}_{\substack{elm\\olm}} = \frac{\pi\ j^{l-m}}{N_{e_1}(c_1)} = \sum_{i=0}^{\infty}\ \sum_{p=0}^{\infty} (-j)^{i+p} D^m_{\substack{ei\\oi}}(c_2) D^l_{ep}(c_1) \mathrm{X}^{2\rightarrow 1}_{\substack{eip\\oip}} \tag{19}$$

$$WO^{2\rightarrow 1}_{\substack{elm\\olm}} = \mp \frac{\pi\ j^{l-m}}{N_{o1}(c_1)} = \sum_{i=0}^{\infty}\ \sum_{p=0}^{\infty} (-j)^{i+p} D^m_{\substack{ei\\oi}}(c_2) D^l_{op}(c_1) Y^{2\rightarrow 1}_{\substack{eip\\oip}} \tag{20}$$

and

$$\mathrm{X}^{2\rightarrow 1}_{\substack{eip\\oip}} = H^{(2)}_{p-i}(kd)\begin{bmatrix}\cos\Psi^-\\ \sin\Psi^-\end{bmatrix} + (-1)^i H^{(2)}_{p+i}(kd)\begin{bmatrix}\cos\Psi^+\\ \sin\Psi^+\end{bmatrix} \tag{21}$$

$$Y^{2\rightarrow 1}_{\substack{eip\\oip}} = H^{(2)}_{p-i}(kd)\begin{bmatrix}\sin\Psi^-\\ \cos\Psi^-\end{bmatrix} - (-1)^i H^{(2)}_{p+i}(kd)\begin{bmatrix}\sin\Psi^+\\ \cos\Psi^+\end{bmatrix} \tag{22}$$

with

$$\Psi^+ = i\Psi_{21} + p\Psi_{12}\ ,\ \Psi^- = i\Psi_{21} - p\Psi_{12}\quad . \tag{23}$$

In the above equations, Ψ_{12} and Ψ_{21} are measured from the local positive x axis of each strip to the separation distance between the strips, $H^{(2)}_{p+i}(kd)$ is the Hankel function of the second kind with argument kd, and D^n_{ej} and D^n_{oj} are the Fourier coefficients of the Mathieu functions [10]. The sum is over only even or odd values of *i(p)* depending whether m(*l*) is even or odd in equations (19) and (20). Substituting equation (18) into (17) and using the orthogonality properties of the angular Mathieu functions yields the second order scattered field coefficients, which may be written for each strip in matrix form as

$$\begin{bmatrix}B^2_{em}\\ B^2_{om}\end{bmatrix} = \begin{bmatrix}Q^{11}_{enm} & 0\\ 0 & Q^{11}_{onm}\end{bmatrix}\begin{bmatrix}Q^{12}_{eenm} & Q^{12}_{eonm}\\ Q^{12}_{oenm} & Q^{12}_{oonm}\end{bmatrix}\begin{bmatrix}C^1_{em}\\ C^1_{om}\end{bmatrix} \tag{24}$$

$$\begin{bmatrix}C^2_{em}\\ C^2_{om}\end{bmatrix} = \begin{bmatrix}Q^{22}_{enm} & 0\\ 0 & Q^{22}_{onm}\end{bmatrix}\begin{bmatrix}Q^{21}_{eenm} & Q^{21}_{eonm}\\ Q^{21}_{oenm} & Q^{21}_{oonm}\end{bmatrix}\begin{bmatrix}B^1_{em}\\ B^1_{om}\end{bmatrix} \tag{25}$$

where C^2_{em} and C^2_{om} are the second order scattered field expansion coefficients of the second strip, and

$$Q^{12}_{eenm} = WE^{2\rightarrow 1}_{enm}\ ,\ Q^{12}_{eonm} = WE^{2\rightarrow 1}_{onm}\ ,\ Q^{12}_{oenm} = WO^{2\rightarrow 1}_{enm}\ ,$$
$$\text{and}\ \ Q^{12}_{oonm} = WO^{2\rightarrow 1}_{onm} \tag{26}$$

Similar equations may be written correspond to Q^{21}_{eenm}, Q^{21}_{eonm}, Q^{21}_{oenm}, and Q^{21}_{oonm}.

To obtain a general solution, we solve similarly for the higher order scattered fields which are sensitive to the electrical widths, separation between the strips and angles of incidence. This means if the strips are located very close to one another, then the higher order scattered fields are significant and therefore should be included in the solution. The significance of the higher order scattered fields will be verified numerically by comparison with published data.

The general expression for the *k*th order scattered field coefficients may be written as

$$\begin{bmatrix}B^k_{em}\\ B^k_{om}\end{bmatrix} = \begin{bmatrix}Q^{11}_{enm} & 0\\ 0 & Q^{11}_{onm}\end{bmatrix}\begin{bmatrix}Q^{12}_{eenm} & Q^{12}_{eonm}\\ Q^{12}_{oenm} & Q^{12}_{oonm}\end{bmatrix}\begin{bmatrix}C^{k-1}_{em}\\ C^{k-1}_{om}\end{bmatrix} \tag{27}$$

$$\begin{bmatrix} C_{em}^{k} \\ C_{om}^{k} \end{bmatrix} = \begin{bmatrix} Q_{enm}^{22} & 0 \\ 0 & Q_{onm}^{22} \end{bmatrix} \begin{bmatrix} Q_{eenm}^{21} & Q_{eonm}^{21} \\ Q_{oenm}^{21} & Q_{oonm}^{21} \end{bmatrix} \begin{bmatrix} B_{em}^{k-1} \\ B_{om}^{k-1} \end{bmatrix}. \qquad (28)$$

It should be noted that the matrices in equations (27) and (28) are computed once (i.e., *k*=2) for the electrical sizes and separation considered and used for the subsequent iterations (i.e., *k*=3,4,…).

Once the scattered field coefficients are determined, the total far field from the strips due to the *k*th order scattered field can be determined [1]-[5].

5. Numerical Results

In order to solve for the unknown scattered field coefficients, the infinite series are first truncated to include only the first *N* terms, where *N* in general, is a suitable truncation number proportional to the strips electrical width. In the computation, the value of *N* has been chosen to impose a convergence condition that provides solution accuracy with at least four significant figures [14], [15]. It is found that increasing the electrical width of the scatterers will increase the total truncation number of *N* terms [16].

To check the accuracy of our computer program, we recomputed first the results given in references [2], [12] for large electrical separation when it is compared with the electrical sizes of the scatteres and we obtained complete agreement between methods by only implementing the first order scattered field using the iterative solution. Fig. 2 shows the numerical result of the normalized echo width pattern $\sqrt{\sigma / \lambda}$ versus the scattering angle ϕ for two identical strips with electrical width ka=3.14. The electrical separation between the center of the strips is assumed to be kd=12.5 and at an angle of incidence $\phi_i = 90^o$ (broadside incidence). It can be seen that the results of the first scattered order (*k*=1) presented by solid line is satisfactory at all backscattering angles because the electrical separation between the strips is large compared to their width. To set a criterion for terminating the iteration process, the scattered field after each iteration is calculated and divided by the total field scattered from the pervious iterations, and the process is terminated when the ratio is smaller than 10^{-4} [7]. Fig. 3 has the same electrical parameters except the electrical separation is reduced to 7. It can be seen that the numerical results of the first order scattered field is satisfactory except at resonance scattering angles. This is because the first order scattered field does not take into account the interaction between the strips and hence k=1 represents the sum of the scattered field due to the incident field only. The significance of the multiple scattered fields can be seen in the second scattered order term (*k=2*) which includes the scattered fields due to the plane wave incidence plus the scattered fields due to the first order scattered field due to the incident field on each strip. However, the results show that four scattered field orders are needed to obtain convergent solution at the resonance scattering angles. Fig. 4 is similar to Fig. 2 except the width of the second strip is reduced from 3.14 to 2.0 and kd=5.5. We can see that the number of scattered fields needed is four to obtain convergent solution. Fig. 5 shows the normalized echo width pattern for two identical strips of width ka=5.0, kd=13, and at angle of incidence of zero degree (endfire). Three iterations are needed to obtain convergent solution. Fig. 6 is similar to Fig. 5 except that the incident angle is 90 degrees and kd=11.

Fig. 7 shows the numerical results of the normalized backscattering echo width pattern versus the electrical separation (*k*d) for two identical strips of width ka=5.0 and at angle of incidence of zero degree. The electrical separation is taken between 11 and 23. The results show that the behavior of the backscattering cross section is sinusoidally and with k=4 a convergent solution is obtained at all electrical separations. Fig. 8 is similar to Fig. 7 except the incident angle is 90 degrees. Again, the backscattering cross section is behaving sinusoidally and four scattered field orders is needed to obtain convergent solution.

6. Conclusions

We have investigated the problem of multiply field scattered due to a plane electromagnetic wave incident on arbitrary oriented two perfectly conducting strips. The boundary conditions were implemented using the translation addition theorem. The numerical results indicated that the number of multiple scattered fields depends on the electrical width of the strips, electrical separations and incident angles. We have seen that the iterative solution gives insight to the nature of the multiple scattered fields where it is sometime strong (more terms needed, Fig. 3 at ϕ 88^o) or weak (less terms needed, Fig. 3 at ϕ 200^o) at some specific scattering angles. A potential advantage of using the iterative solution is that of saving computer time and memory by avoiding the inversion of system matrix.

ACKNOWLEDGEMENT

The authors wish to acknowledge the support provided by the University of Sharjah and United Arab Emirates University, U.A.E.

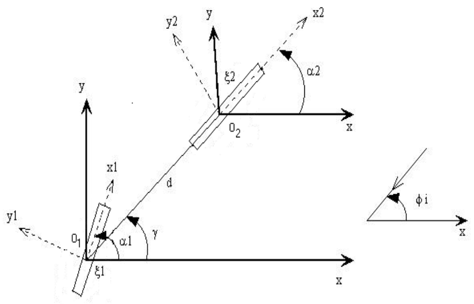

Figure 1: Scattering geometry of two conducting strips.

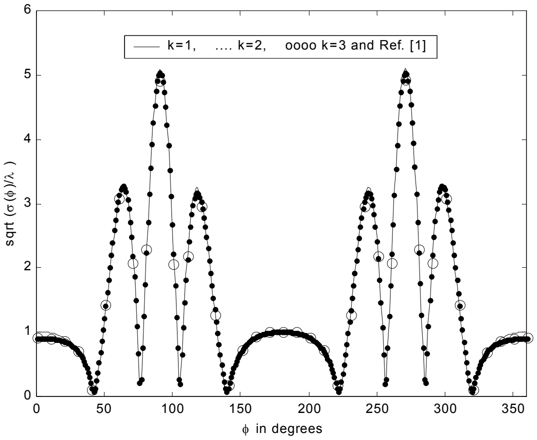

Figure 2: Normalized echo pattern width versus the scattering angle ϕ for two identical conducting strips with ka$_1$=ka$_2$=3.14, kd=12.5, $\alpha_1 = \alpha_2 = 0^o$, $\phi_i = 90^o$, $\gamma = 0^o$.

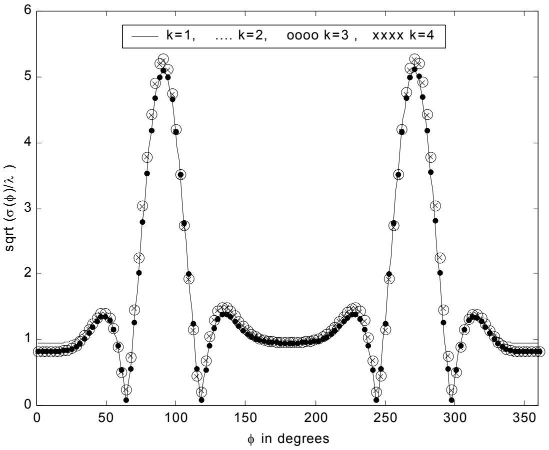

Figure 3: Normalized echo pattern width versus the scattering angle ϕ for two identical conducting strips with ka$_1$=ka$_2$=3.14, kd=7, $\alpha_1 = \alpha_2 = 0^o$, $\phi_i = 90^o$, $\gamma = 0^o$.

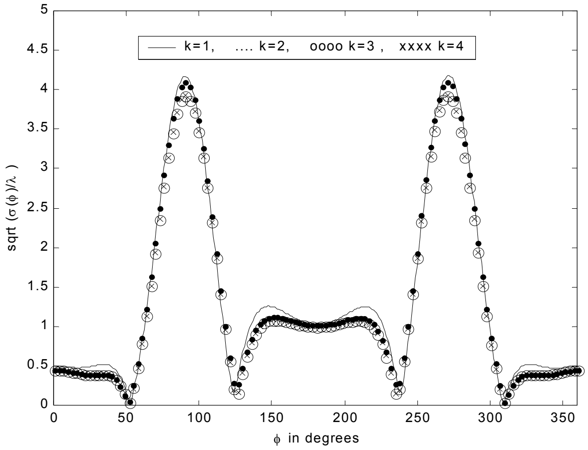

Figure 4: Normalized echo pattern width versus the scattering angle ϕ for two conducting strips with ka$_1$=3.14 , ka$_2$=2.0, kd=5.5, $\alpha_1 = \alpha_2 = 0^o$, $\phi_i = 90^o$, $\gamma = 0^o$.

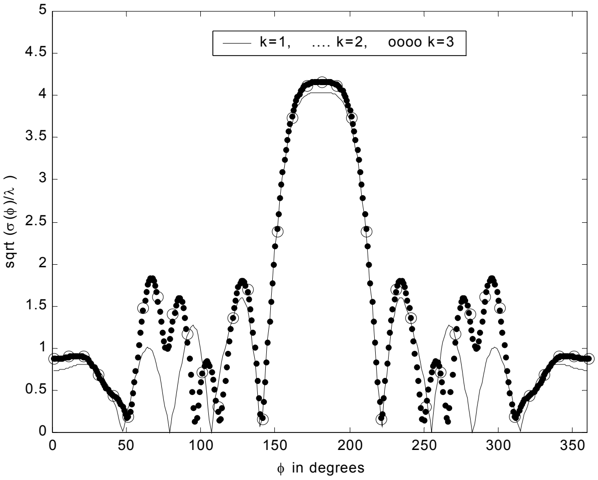

Figure 5: Normalized echo pattern width versus the scattering angle ϕ for two conducting strips with ka$_1$=ka$_2$=5.0, kd=13, $\alpha_1 = \alpha_2 = 0^o$, $\phi_i = 0^o$, $\gamma = 0^o$.

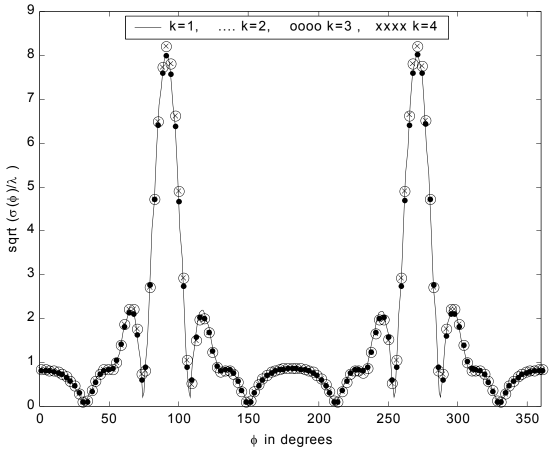

Figure 6: Normalized echo pattern width versus the scattering angle ϕ for two conducting strips with $ka_1=ka_2=5.0$, $kd=11$, $\alpha_1=\alpha_2=90^o$, $\phi_i=0^o$, $\gamma=0^o$.

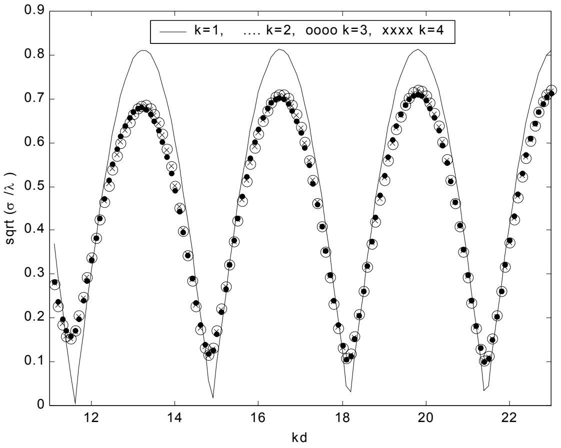

Figure 7: Normalized backscattering cross section versus the electrical separation kd for conducting strips with $ka_1=ka_2=5$, $\alpha_1=\alpha_2=0^o$, $\phi_i=0^o$, $\gamma=0^o$.

References

[1] H. A. Ragheb and M. Hamid, "Simulation of cylindrical scattering surfaces by conducting strips, " *Int. J. Electronics*, vol. 64, pp. 521-535, 1988.

[2] A. Sebak, "Transverse magnetic scattering by parallel conducting elliptic cylinders," *Can. J. Phys*., vol. 69, pp. 1233-1241, 1991.

[3] Sebak, "Electromagnetic scattering by two parallel dielectric elliptic cylinders," *IEEE Trans. Antennas and Propagat*., vol. AP-42, pp. 1521-1527, 1994.

[4] K. Hongo, "Multiple scattering by two conducting circular cylinders," *IEEE Trans. Antennas and Propagat.*, vol. AP-26, pp. 784-751, 1978.

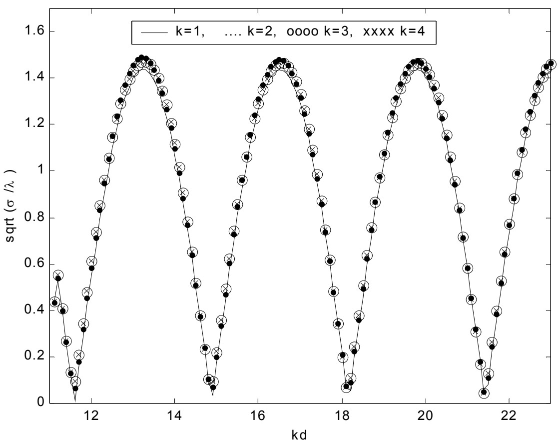

Figure 8: Normalized backscattering cross section versus the electrical separation kd for conducting strips with $ka_1=ka_2=5$, $\alpha_1=\alpha_2=0^o$, $\phi_i=90^o$, $\gamma=0^o$.

[5] H. Ragheb and M. Hamid, "Scattering by *N* parallel conducting circular cylinders," *Int. J. of Electronics,* vol. 59, pp. 407-421, 1985.

[6] A.Z. Elsherbeni and M. Hamid, "Scattering by parallel conducting circular cylinders," *IEEE Trans. Antennas and Propagat.*, vol. AP-35, pp. 335-358, 1987.

[7] A-K. Hamid, I.R. Ciric, and M. Hamid, "Iterative solution of the scattering by an arbitrary configuration of conducting or dielectric spheres," *IEE Proc. Part H*, vol. 138, pp. 565-572, 1991.

[8] P. Sinha and R. H. MacPhie," Electromagnetic plane wave scattering by a system of two parallel conducting prolate spheroids," *IEEE Trans. Antennas and Propagat.*, vol. AP-31, pp. 294-304, 1983.

[9] M. Cooray and I.R. Ciric," Electromagnetic wave scattering by a system of two spheroids of arbitrary orientation," *IEEE Trans. Antennas and Propagat.*, vol. No. 37, pp. 608-618, 1983.

[10] P. M. Morse and H. Feshach, Methods of theoretical physics, pp. 1407-1420. New York: McGraw-Hill, 1953.

[11] K. Saemark," A note on addition theorems for Mathieu functions," *Z. Math. Phys*., vol. 10, pp. 426-428, 1959.

[12] M. G. Andreasen," Scattering from parallel metallic cylinders with arbitrary cross sections," *IEEE Trans. Antennas and Propagat.*, vol. AP-12, pp. 746-754, 1964.

[13] M. Ouda, M. Hussein, A. Sebak, and Y. Antar,"Multiple scattering by dielectric cylinders using a multifilament current model," *J. of electromagnetic waves and applications (JEWA)*, vol. 7, pp. 215-234, 1993.

[14] Toyama, N., and Shogen, K., "Computation of the value of the even and odd Mathieu functions of order N for a given parameter S and argument X," *IEEE Trans. Antennas and Propagat.*, vol. AP-32, pp. 537-539, 1984.

[15] A-K. Hamid, M.I. Hussein, H. Ragheb, and M. Hamid, “Mathieu Functions of Complex Arguments and Their Applications to the Scattering by Lossy elliptic Cylinders,” *Appl. Comput. Electromagnetics Soc.*, Vol. 17, no. 3, pp. 209-217, 2002.

[16] M.I. Hussien, and A-K. Hamid, "Electromagnetic Scattering by a Lossy Dielectric Cylinder", *J. of electromagnetic waves and applications (JEWA)*, vol. 15, no. 11, pp. 1469-1482, 2001.

A.-K. Hamid was born in Tulkarm, West Bank, on Sept. 9, 1963. He received the B.Sc. degree in Electrical Engineering from West Virginia Tech, West Virginia, U.S.A. in 1985. He received the M.Sc. and Ph.D. degrees from the university of Manitoba, Winnipeg, Manitoba, Canada in 1988 and 1991, respectively, both in Electrical Engineering. From 1991-1993, he was with Quantic Laboratories Inc., Winnipeg, Manitoba, Canada, developing two and three dimensional electromagnetic field solvers using boundary integral method. From 1994-2000 he was with the faculty of electrical engineering at King Fahd University of Petroleum and Minerals, Dhahran, Saudi Arabia. Since Sept. 2000 he has been an associate Prof. in the electrical\electronics and computer engineering department at the University of Sharjah, Sharjah, United Arab Emirates. His research interest includes EM wave scattering from two and three dimensional bodies, propagation along waveguides with discontinuities, FDTD simulation of cellular phones, and inverse scattering usingneural networks.

Mousa I. Hussein received the B.Sc. degree in electrical engineering from West Virginia Tech, USA, 1985,M.Sc. and Ph.D. degrees from University of Manitoba, Winnipeg, MB, Canada, in 1992 and 1995, respectively, both in electrical engineering. From 1995 to 1997, he was with research and development group at Integrated Engineering Software Inc., Winnipeg, Canada, working on developing EM specialized software based on the Boundary Element method. In 1997 he joined the faculty of engineering at Amman University, Amman, Jordan, as an Assistant Professor. He is currently with the Electrical Engineering Dept. at the United Arab Emirates University. Dr. Hussein current research interests includes, computational electromagnetics, electromagnetic scattering, antenna analysis and design, EMI and signal integrity. microstrip antennas, phased arrays, slot and open ended waveguide antennas.

Numerical Analysis of Impedance of Asymmetric TEM Cell Filled With Inhomogeneous, Isotropic Dielectric

K. Malathi
School of Electronics and Communication Engineering,
Anna University, Chennai-600 025 INDIA

Annapurna Das
School of Electronics and Communication Engineering,
Anna University, Chennai-600 025 INDIA

Abstract–**This paper investigates the effect of vertically offset septum on characteristic impedance (Z_0) of transverse electromagnetic (TEM) cell. The Septum is considered to be of finite thickness for the analysis. Impedance analysis is done initially for symmetric TEM cell with homogenous dielectric using Finite Element Method (FEM) and the numerical results included are compared with results obtained by other authors. A good agreement is established. Numerical analysis using FEM is also done for Z_0 of Asymmetric TEM cell with septum of finite thickness filled with inhomogeneous dielectric. The effect of inhomogenity and offset of septum on Z_0 is discussed. Variation of Z_0 with width of the septum is represented graphically.**

Key Words: TEM cell, FEM, effective dielectric constant

1. INTRODUCTION

The TEM cell is similar in structure to a rectangular coaxial transmission line (RCTL), except for the fact that width of the inner conductor of TEM cell is comparatively larger (Figure 1). These cells are used in the generation of standard electromagnetic fields and to study the effects of electromagnetic radiation on biological objects and electronic systems [1].

The common configuration of TEM cell is, rectangular shaped metallic shielded outer conductors and a flat septum with air dielectric inside the cell. The septum may be located arbitrarily inside the enclosure, parallel to the top and bottom outer conductors. Both the inner and outer conductors are tapered at the ends for impedance matching with the standard 50 ohms coaxial connectors. The central section of the Cell is termed as uniform cross section that propagates uniform TEM fields. A plane wave field environment inside the cell is simulated for electromagnetic interference (EMI) testing of equipments placed between septum and outer conductor.

Some of the problems concerning the design of such cells are the maximization of

- Usable test space.
- Transmitted power through the cells.

Optimum dimensions of these cells are to be determined to solve the above problems specified.

Offseting the inner conductor from the center in vertical direction creates two chambers of unequal sizes that allow the testing of both larger equipment and smaller probes without increasing the overall size of the cell.

Some of the asymmetric configurations are available commercially. GTEM cell is a class of asymmetric cell that can be used for the Electromagnetic Susceptibility measurements in the Ghz range. Rohde and Schwarz have fabricated S-Line that is used in the measurement of Electromagnetic interference and Susceptibility. Its operating range spans from 150 KHz to GHz. It offers test volume comparable to that of anechoic chambers. This S line is characterized by high field strength and field uniformity. These lines have a compact design.

Another type of compact test cell which Rohde and Schwarz presents is an M-line which can be used in the frequency range of 800 MHz to 40 GHz which can be used for measurements in the RF and microwave range.

The TEM cell and the tapered transitions should have Z_0 that matches with the coaxial connectors connected at the end. This ensures minimum standing wave ratio (SWR) and hence maximum power transfer to the cell from the feeder line.

Therefore, for accurate design of such cells and to interpret RF measurements made, Z_0 has to be determined considering finite thickness of septum for its different vertical positions in the cross section.

Rectangular Coaxial Transmission Line was analyzed by [5]-[8] for symmetrically placed inner conductor of finite thickness. A set of design curves for Z_0 of RCTL was given by [6], [7]. Guckel [9] used conformal mapping to find Z_0 of rectangular transmission lines of asymmetrically placed inner conductor with air dielectric inside. Pantic and Mittra [10] performed Quasi TEM analysis on thick transmission lines with multidielectric layers to find Z_0 neglecting the influence of sidewalls. However in TEM cells the effect of sidewalls on Z_0 cannot be neglected, as it influences the RF measurements made inside the cell.

1054-4887 © 2004 ACES

In the light of above observations this paper analyses the effect of finite thickness septum placed in different vertical off set positions, on the characteristic impedance (Z_0) of the TEM cell. In this analysis, inhomogeneous dielectric in the cell is considered. The region above the septum is considered to have air dielectric ($\varepsilon_{r1} = 1$) and the region below the septum is considered to have a dielectric with ($\varepsilon = \varepsilon_{r2}\varepsilon_0$) (Figure 1). The dielectric placed below the septum lends a good mechanical support to the EUT placed inside for RF measurements. The effect of this inhomogenity on the characteristic impedance is also studied. The analysis helps in the design of such cells and to interpret the RF measurements made inside the cell.

Classical method of approaches may fail if the medium is inhomogeneous or anisotropic [12]. So Finite Element Method (FEM) is used to solve the laplace equation to obtain the potential distribution inside the cell. Then Gauss's law is applied to find the charge around the septum, which, in turn, is used to find the capacitance and hence the impedance of the cell.

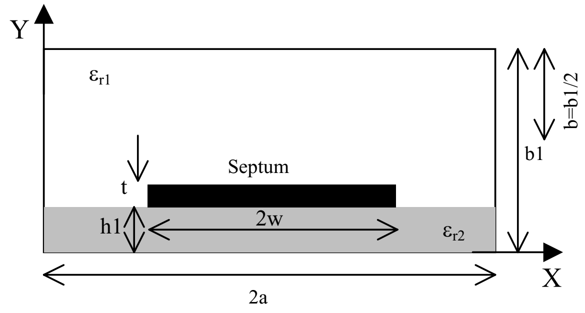

Figure 1. Cross section of asymmetric TEM cell with inhomogeneous dielectric.

2. FEM FORMULATION

To find the potential distribution, Laplace equation

$$\nabla^2 V = 0 \qquad (1)$$

is solved, where V is the potential at (x,y) (Figure 1). The boundary conditions are

$$\left.\begin{array}{l} V(x, 0) = 0 = V(x, b1) \;;\; \text{for } 0 \le x \le 2a \\ V(0,y) = 0 = V(2a, y) \;;\; \text{for } 0 \le y \le b1 \\ \text{and } V = V_0 \text{ at } \left\}\begin{array}{l} D - W \le x \le D + W \text{ at } y = h1 \\ \text{for zero thickness septum.} \end{array}\right. \\ \qquad\qquad \left.\begin{array}{l} D - W \le x \le D + W \text{ at } h1 \\ h1 - t/2 \le y \le h1 + t/2 \end{array}\right\} \end{array}\right\} \qquad (2)$$

for septum of finite thickness.

2.1 Discretisation

Due to uniaxial symmetry of the domain, only one half of the cross section ($0 \le x \le a$, $0 \le y \le b1$) of the TEM cell is considered for the analysis. The domain is subdivided into a set of triangular subdomains called finite elements as shown in Figure 2, with local nodes (1, 2,3) and global node numbering 1,2,3 … (nx + 1), (nx + 1)(ny + 1).

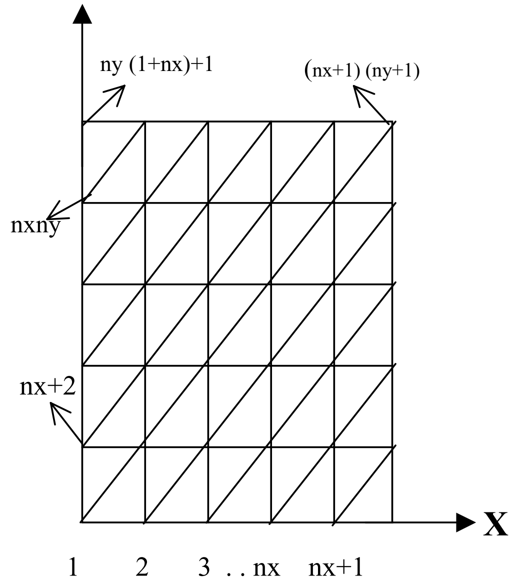

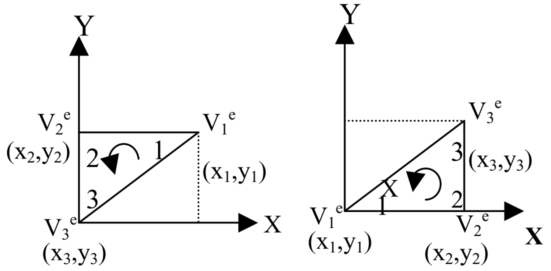

Typical triangular elements: 1,2,3 are local node numbers.

Figure 2. Finite Element Mesh.

2.2 Element Equation

The approximate solution to equation (1) within a typical finite element in the domain is of the form

$$V_{(x,y)} = \sum_{j=1}^{n} V_j^e \, \tau_j^e \, (x, y) \qquad (3)$$

where V_j^e is the value of the potential at the jth node (x_j, y_j) of the element and τ_j^e are the lagrange interpolation functions [2]. The polynomial approximation for V within an element is chosen as

$$V^e_{(x,y)} = g_1 + g_2 x + g_3 y \;, \qquad (4)$$

where g_1, g_2, g_3 are constants pertaining to local nodes (Figure 2) equation (4) contains three linearly independent terms and it is linear in both x and y considering a typical triangular element the potential V_1^e, V_2^e, V_3^e are obtained using equation (4) as

$$\begin{bmatrix} V_1^e \\ V_2^e \\ V_3^e \end{bmatrix} = \begin{bmatrix} 1 & x_1 & y_1 \\ 1 & x_2 & y_2 \\ 1 & x_3 & y_3 \end{bmatrix} \begin{bmatrix} g_1 \\ g_2 \\ g_3 \end{bmatrix}. \qquad (5)$$

The coefficients g_1, g_2, and g_3 are determined from (5) and substituted in (4) to obtain,

$$V^e = \sum_{j=1}^{3} V_j^e \, \tau_j^e \, (x, y) \qquad (6)$$

where

$$\tau_j^e = \frac{1}{2A^e} \left(\alpha_i^e + \beta_i^e \, x + \gamma_i^e \, y \right) \; (i = 1, 2, 3), \qquad (7)$$

α_i, β_i and γ_i are geometric constants given by

$\alpha_i = x_j \, y_k - x_k \, y_j$

$\beta_i = y_j - y_k$ (8)

$\gamma_I = -(x_j - x_k)$

$i \neq j \neq k$ and i, j, and k permute in natural order,

and A^e is the area of the triangle [2] given by

$$A^e = \frac{\alpha_1 + \alpha_2 + \alpha_3}{2}. \qquad (9)$$

The value of A is positive if the nodes are numbered counter clockwise [3]. Equation (6) gives the potential at any point (x, y) within the element. The calculus of variations, an extension of ordinary calculus, is concerned with the theory of maxima and minima [3]. In this problem we are concerned with seeking the minima of an integral expression involving a function of functions or functionals. Moreover we are interested in the necessary condition for a functional to achieve a stationary value. This necessary condition on the functional is generally in the form of a differential equation with boundary conditions on the required function.

In the problem considered, the minimum potential energy requires the potential distribution, which will minimize the stored field energy per unit length. Minimization of the energy then determines the coefficients and thereby implicitly determines an approximation to the potential distribution.

The functional corresponding to Laplace equation is [4]

$$F_e = \frac{1}{2} \int \varepsilon \, |E|^2 \, dS = \frac{1}{2} \int \varepsilon \, | \nabla V^e |^2 \, dS \qquad (10)$$

where Fe is the energy / unit length associated with the element e; E is the electric field strength over the surface dS; ε is the permittivity of the medium.

$$\text{From (6), } \nabla V^e = \sum_{i=1}^{3} V_i^e \, \nabla T_i \qquad (11)$$

Substitute equation (11) in (10)

$$F_e = \frac{1}{2} \sum_{i=1}^{3} \sum_{j=1}^{3} \varepsilon \, V_i^e \left[\int \nabla \tau_i \, . \, \nabla \tau_j . dS \right] V_j^e . \qquad (12)$$

The term in the brackets of (12) is defined as

$$K_{ij}^e = \int \nabla \tau_i \, . \, \nabla \tau_j \, dS . \qquad (13)$$

Writing (12) in Matrix form

$$F_e = \frac{1}{2} \, \varepsilon \, \left[V^e \right]^t \left[K^e \right] \left[V^e \right] \qquad (14)$$

where the subscript t denotes the transpose of the matrix,

$$\left[V^e \right] = \begin{bmatrix} V_1^e \\ V_2^e \\ V_3^e \end{bmatrix}, \qquad (15)$$

$$\text{and } \left[K^e \right] = \begin{bmatrix} K_{11}^e & K_{12}^e & K_{13}^e \\ K_{21}^e & K_{22}^e & K_{23}^e \\ K_{31}^e & K_{32}^e & K_{33}^e \end{bmatrix} \qquad (16)$$

is the element coefficient matrix.

The matrix element K_{ij}^e of the coefficient matrix may be regarded as the coupling between nodes i and j. Its value is obtained from equations (7) and (13).

2.3 Assembling of All Elements

Having considered a typical element, all such elements in the solution region are assembled. The energy associated with the assemblage of elements is

$$F = \sum_{e=1}^{N} F_e = \frac{1}{2} \, \varepsilon \, [V]^t \, [K] \, [V], \qquad (17)$$

$$\text{where} \quad [V] = \begin{bmatrix} V_1 \\ V_2 \\ . \\ . \\ V_n \end{bmatrix}, \qquad (18)$$

and where N is the number of elements and n is the number of nodes and [K] is called global coefficient matrix [2] with the following properties:

1) It is symmetric.
2) $K_{ij} = 0$ if no coupling exists between nodes i and j, so [K] is sparse.
3) It is singular.

3. SOLVING THE RESULTING EQUATIONS

Laplace equation is satisfied when the total energy in the solution region is minimum i.e.,

$$\frac{\partial F}{\partial V_1} = \frac{\partial F}{\partial V_2} = \ldots\ldots\ldots = \frac{\partial F}{\partial V_n} = 0 \qquad (19)$$

or $$\frac{\partial F}{\partial V_k} = 0 \quad K = 1, 2, ... n . \qquad (20)$$

In general $\frac{\partial F}{\partial V_k} = 0$ leads to $\sum_{k,i=1}^{n} V_i \; K_{ik} = 0$, (21)

where n is the number of nodes in the mesh. Writing equation (21) for all nodes we obtain a set of simultaneous equations from which the solution of $[V]_t = [V_1, V_2, ….. , V_n]$ can be found by the method of iteration. As node m is a mesh with n nodes

$$V_m = -\frac{1}{K_{mm}} \sum_{i=1, i \neq m}^{n} V_i \; K_{mi} \quad , \qquad (22)$$

where node m is a free node. Since $K_{mi} = 0$ if node m is not directly connected to node i. Only nodes that are directly linked to node m contribute to V_m in equation (22) can be iteratively applied to all the free nodes where the value of the potential is to be found. The global coefficient matrix was obtained with the help of computer implementation using MATLAB package.

4. THE CHARACTERISTIC IMPEDANCE Zo

The characteristic impedance Z_0 is obtained as follows

$$Z_0 = 1/uC \qquad (23)$$

where $$u = u_o \sqrt{\frac{Co}{C}} = \frac{u_o}{\sqrt{\varepsilon_{eff}}} \qquad (24)$$

$$\varepsilon_{eff} = C/Co \quad , \qquad (25)$$

where u_0 is speed of light in free space, ε_{eff} is the effective dielectric constant, C = Capacitance of the cell with the dielectric of relative permittivity ε_{r2} below the septum, and Co the capacitance of the cell without the dielectric below the septum (i.e) ($\varepsilon_{r2} = \varepsilon_0$). Thus to find Z_0 for an inhomogeneous medium requires calculation of capacitance / unit length of the structure with and without the dielectric substrate below the septum. If Vo is the potential difference between the inner and the outer conductors, then,

$$C = 2Q/Vo \qquad (26)$$

where Q is the charge / unit length. The factor 2 is included since only half of the domain was considered for the analysis. To find Q, Gauss's law is applied [4] to the closed path J enclosing the septum, as shown in Figure (3),

$$Q = \oint D.dl = \oint \varepsilon \frac{\partial V}{\partial n} . dl \qquad (27)$$

$$Q = \varepsilon\left(\frac{V_a - V_b}{\Delta y}\right)\Delta x + \varepsilon\left(\frac{V_c - V_d}{\Delta y}\right)\Delta x + \varepsilon\left(\frac{V_u - V_w}{\Delta x}\right)\Delta y + \varepsilon\left(\frac{V_y - V_z}{\Delta x}\right)\Delta y + ... \qquad (28)$$

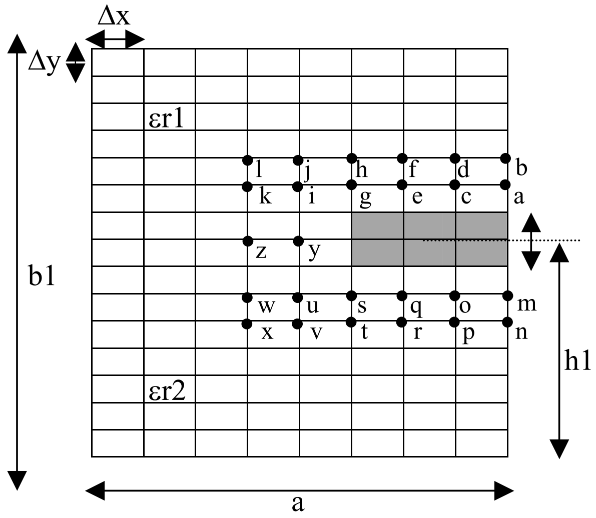

Figure 3. Illustrating path to find Q.

Since Δx = Δy, $Q = \varepsilon_0 \sum \varepsilon_{ri} V_i$ for nodes i on external rectangle b,d,f...r, p,n with corners (such 1 and x) not counted. $Q = - \varepsilon_0 \sum \varepsilon_{ri} V_i$ for nodes i on inner rectangle a, c, e, ...q,o,m with corners (such as i and u) counted twice where V_i and ε_{ri} are the potential and dielectric constant at ith node. If i is on the dielectric interface $\varepsilon_{ri} = (\varepsilon_{r1} + \varepsilon_{r2}) / 2$. Also if i is on the line of symmetry Vi = Vi/2 to avoid V_i twice in equation (28) [4]

$$Co = Q_0 / V_0 , \qquad (29)$$

where Q_0 is obtained by removing the dielectric and finding V_i at the free nodes and then using (31) with ε_{ri} = 1 at all nodes. Once Q and Q_0 are calculated C, Co and Z_0 are obtained, $Z_0 = \frac{1}{uo\sqrt{CC_0}}$, (30)

where $u_0 = 3 \times 10^8$ m/sec.

5. RESULTS AND DISCUSSIONS

Uniform Cross section of the TEM cell for two dimensions 2a/b1=1 and 2a/b1=2 and septum thickness t/b1=0.1 is considered for the impedance analysis. Table 1 gives the impedance values (Z_0) of Symmetric TEM cell computed by FEM and its comparison with other methods. The impedance values obtained by FEM are found to be in good agreement with those published by other authors. Tables 2 and 3 gives Z_0 values of asymmetric TEM cell for various vertical offset position of septum for homogeneous and for inhomogeneous dielectric inside the cell.

It is observed that maximum impedance is achieved when the septum is placed at the center of the TEM cell. Offsetting the septum vertically decreases Z_0 of the cell. (Figures 4 and 5). The variation of Z_0 for different dielectric constants ($2.1 < \varepsilon_{r2} < 9.9$) below septum.is shown in Figures 6 to 10. It is shown in figures 8 to 10 the variation of Z_0 with the width of the septum. Effective permittivity of the cell is presented in Tables 2 and 3.It is observed that presence of a different dielectric (other than air) below the septum decreases the value of Z_0.So by proper choice of ε_{r2} and the width of the septum desired values of Z_0 can be obtained by suitably offsetting the septum (to lesser height) so that bigger equipments can be tested.

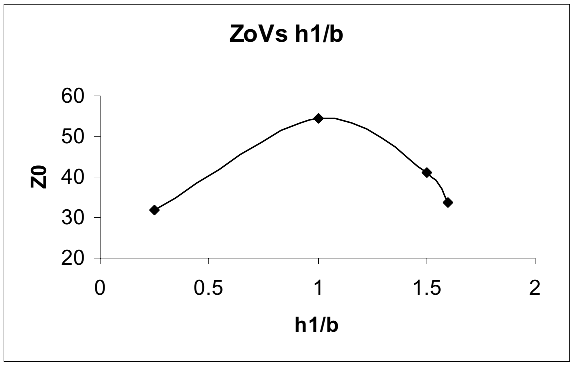

Figure 4. Z_0 versus h1/b.

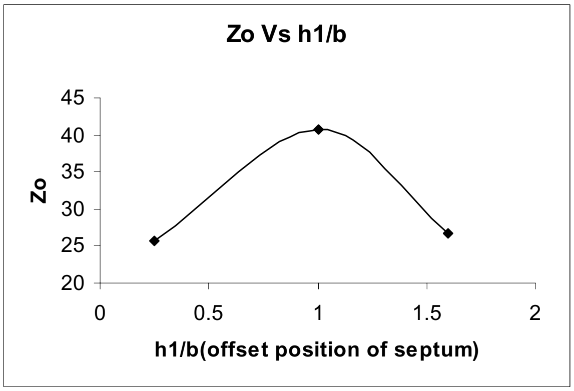

Figure 5. Z_0 versus h1/b.

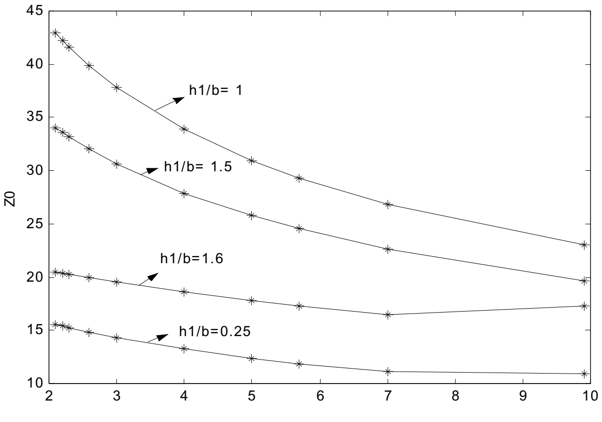

Figure 6. Relative dielectric constant below septum.

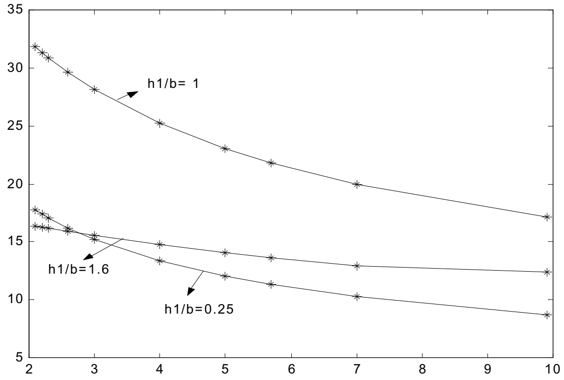

Figure 7. Relative dielectric constant below spectrum.

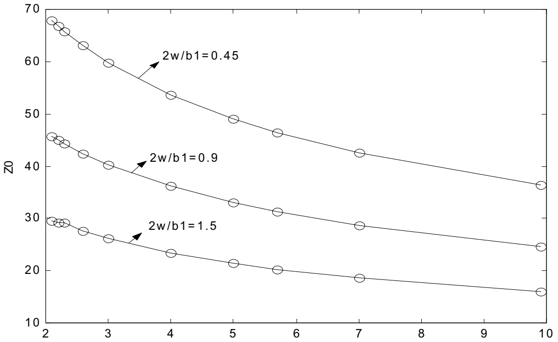

Figure 8. Relative dielectric constant below septum.

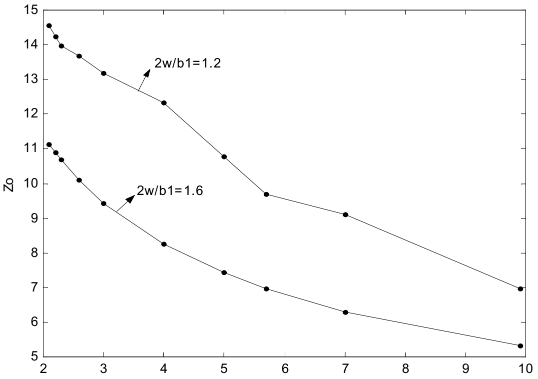

Figure 9. Relative dielectric constant below septum.

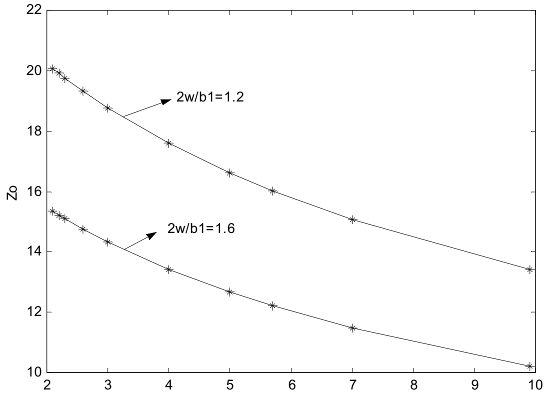

Figure 10. Relative dielectric constant below septum.

Table 1. COMPARISON OF Z_0 VALUES (t/b1=0.1) $\varepsilon r_{1=}\ \varepsilon r_2=1$

Dimension		FEM	Chen expression [5]	Cruzen & graver [6]	Metcalf [7]	Getsinger [8]
2a/b1	2w/b1	Z_0	Z_0	Z_0	Z_0	Z_0
1	0.8	45.2	44.7	40.9	40.5	40.9
1	0.7	55.6	57.4	55.3	54.7	55.2
2	1.8	26.6	29.3	27.7	27.7	27.6
2	1.5	36.5	38.7	38.0	38.3	38.1
2	0.9	58.9	58.6	58.6	58.7	58.6
2	0.5	87.9	86.7	86.5	85.9	87.3

Table 2. Z_0 VALUES OF TEM CELL WITH INHOMOGENEOUS DIELECTRIC (2a/b1=1 & t/b1=0.1) $\varepsilon r_{1=}\ 1$

2a/b1	**w/a**	**h1/b**	$\varepsilon_{r1}=\varepsilon_{r2}$ **Z_0**		**Relative Dielectric constant below septum (εr_2)**									
					2.1	**2.2**	**2.3**	**2.6**	**3**	**4**	**5**	**5.7**	**7**	**9.9**
1	0.8	0.25	25.76	Z_0	17.75	17.4	17.07	16.19	15.21	13.36	12.059	11.34	10.298	8.73
				Eps_eff	1.79	1.86	1.94	2.15	2.44	3.16	3.88	4.39	5.32	5.71
1	0.8	1	40.66	Z_0	31.83	31.34	30.88	29.59	28.11	25.197	23.04	21.82	19.99	17.15
				Eps_eff	1.53	1.57	1.62	1.77	1.96	2.44	2.91	3.25	3.87	5.26
1	0.8	1.6	26.71	Z_0	16.35	16.25	16.15	15.87	15.52	14.73	14.05	13.63	12.93	12.39
				Eps_eff	2.47	2.5	2.53	2.62	2.75	3.05	3.35	3.56	3.95	3.69
1	0.65	0.25	32.01	Z_0	15.55	15.4	15.25	14.84	14.33	13.26	12.397	11.89	11.08	10.92
				Eps_eff	3.72	3.799	3.87	4.1	4.39	5.12	5.86	6.38	7.33	7.56
1	0.65	1	54.27	Z_0	42.93	42.26	41.62	39.87	37.84	33.88	30.95	29.296	26.82	22.99
				Eps_eff	1.54	1.59	1.64	1.79	1.98	2.47	2.96	3.31	3.94	5.37
1	0.65	1.5	41.17	Z_0	34.03	33.61	33.19	32.04	30.68	27.91	25.78	24.54	22.66	19.65
				Eps_eff	1.39	1.43	1.46	1.57	1.71	2.07	2.43	2.68	3.14	4.18
1	0.65	1.6	33.54	Z_0	20.52	20.41	20.296	19.97	19.55	18.62	17.81	17.30	16.46	17.32
				Eps_eff	2.51	2.54	2.57	2.66	2.77	3.05	3.33	3.54	3.91	3.53

Table 3. Z0 VALUES OF TEM CELL WITH INHOMOGENEOUS DIELECTRIC (2a/b1=2 & t/b1=0.1) $\varepsilon_{r1}=1$

2a/b1	**2w/b1**	**w/a**	**h1/b**	$\varepsilon_{r1}=\varepsilon_{r2}$ **Z_0**		**Relative Dielectric constant below septum**									
						2.1	**2.2**	**2.3**	**2.6**	**3**	**4**	**5**	**5.7**	**7**	**9.9**
2	1.5	0.75	1	37.57	Z_0	29.6	29.15	29.12	27.52	26.14	23.44	21.43	20.29	18.59	15.95
					Eps_eff	1.53	1.57	1.62	1.76	1.96	2.43	2.91	3.25	3.87	5.25
2	0.9	0.45	1	58.36	Z_0	45.64	44.95	44.28	42.45	40.32	36.15	33.05	31.3	28.68	24.61
					Eps_eff	1.52	1.57	1.62	1.76	1.95	2.43	2.91	3.24	3.86	5.25
2	0.45	0.225	1	86.2	Z_0	67.84	66.797	65.798	63.05	59.87	53.65	49.03	46.43	42.52	36.47
					Eps_eff	1.53	1.58	1.63	1.77	1.97	2.45	2.93	3.27	3.897	5.298
2	1.2	0.6	0.25	20.0973	Z_0	14.55	14.24	13.96	13.69	13.19	12.34	10.78	9.69	9.097	6.96
					Eps_eff	1.91	1.99	2.07	2.16	2.32	2.65	3.48	4.3	4.88	8.35
2	1.6	0.8	0.25	15.36	Z_0	11.13	10.896	10.68	10.09	9.44	8.25	7.42	6.96	6.3	5.32
					Eps_eff	1.91	1.99	2.07	2.32	2.65	3.47	4.29	4.87	5.94	8.32
2	1.2	0.6	1.6	22.09	Z_0	20.07	19.92	19.76	19.32	18.78	17.60	16.62	16.02	15.06	13.43
					Eps_eff	1.21	1	1.25	1.31	1.38	1.58	1.77	1.9	2.15	2.71
2	1.6	0.8	1.6	16.91	Z_0	15.34	15.22	15.1	14.76	14.34	13.42	12.66	12.2	11.47	10.21
					Eps_eff	1.22	1.24	1.25	1.31	1.39	1.59	1.78	1.92	2.18	2.74

REFERENCE

[1] M. L. Crawford: ‘Generation of standard EM fields using TEM transmission lines’, *IEEE Trans. MTT*, Vol. MTT-31, pp. 149-154, 1983.

[2] J. N. Reddy: ‘An introduction to the finite element method’, Second edition, *Mc-Graw hill international edition*, 1993.

[3] P. P. Silvester: ‘R.L.Ferrari: ‘Finite elements for electrical engineers’, second edition, *Cambridge university press*, 1990.

[4] M. N. Sadiku, A. Z. Makki, Lawrence, ‘A further introduction to finite element analysis of Electromagnetic problems’, *IEEE Trans. Education,* Vol.34, No. 4, pp. 322-329, Nov. 1991.

[5] T. S. Chen, ‘Determination of the capacitance, inductance, and characteristic impedance of rectangular lines, ‘*IRE Trans. MTT. Vol. MTT-8*, pp. 510-519, Sept. 1960.

[6] O. R. Cruzen and R.V.Garver, ‘Characteristic impedance of rectangular transmission lines *‘IEEE Trans. MTT. Vol. MTT-12*, pp. 488-495, Sept. 1964.

[7] M. S. Metcalf, ‘Characteristic impedance of rectangular transmission lines’, *Proc. Inst. Elect. Eng.,* Vol. 112, pp. 2033-2039, Nov. 1965.

[8] W. T. Getsinger, ’Coupled rectangular bars between parallel plates’, *IRE Trans. MTT. Vol. MTT-10*, pp. 65-72, Jan. 1962.

[9] H. Guckel “Characteristic Impedances of Generalized Rectangular Transmission Lines”, *IEEE Trans. MTT. Vol. MTT-12*, pp. 270-274, December 1964.

[10] Z. Pantic and R. Mittra, ’Quasi-TEM analysis of microwave transmission lines by FEM’, *IEEE trans. MTT, Vol. MTT-34,* November 1986.

[11] M. N. O. Sadiku “Numerical Techniques in Electromagnetics,” *CRC press,* 1992.

[12] L. D. Kovach, ‘Boundary value problems’, *Addison Wesley,* pp. 355-379, 1984.

AUTOMATIC CALCULATION OF BAND DIAGRAMS OF PHOTONIC CRYSTALS USING THE MULTIPLE MULTIPOLE METHOD

Jasmin Smajic, Christian Hafner, Daniel Erni
Laboratory for Electromagnetic Fields and Microwave Electronics
Swiss Federal Institute of Technology
ETH-Zentrum, Gloriastrasse 35, CH-8092 Zürich, Switzerland
E-mail: jsmajic@ifh.ee.ethz.ch

ABSTRACT – In the framework of photonic crystal's band structure calculations, we present a novel way – based on several advanced techniques for searching and tracing eigenvalues with the multiple multipole program – to compute these diagrams automatically, efficiently, and with a high accuracy. Finally, we validate the results for some well known test cases.

***Keywords* – band diagram; multiple multipole program; photonic crystal; eigenvalue analysis.**

I. INTRODUCTION

PHOTONIC Crystals (PhCs) were proposed in 1987 by E. Yablonovitch [1] at the University of California, as an optical counterpart to semiconductors, i.e., PhCs should provide a photonic bandgap in the same way that a semiconductor possesses an electronic bandgap. In fact, PhCs are rarely found in nature. Exceptions are opals and butterfly wings. However, thanks to nano-technology it has become possible to fabricate artificial PhCs in the last decade. These PhCs essentially consist of a periodic assembly of dielectric scatterers, i.e., there is a strong link to the well-known structures of grating theory. One of the important differences between PhCs and semiconductors is the size of the unit cell. For a semiconductor, one has a 3D grid consisting of identical atoms, i.e., the lattice constant in all three directions of the crystal is in the order of the diameter of an atom, whereas the cell size of a PhC is in the order of half an optical wavelength, i.e., much larger. From this fact, one expects that the Photonic Integrated Circuits (PICs) based on PhC concept must be much larger than the traditional semiconductor ICs. But – because of the macroscopic size of the PhC's unit cell – one has much more freedom in introducing and fabricating defects in a PhC than in a semiconductor. Note that a semiconductor becomes interesting from the technological point of view only when a few impurities or defects are introduced and the same holds for PhCs. Doping traditional semiconductors is a rather statistical way of introducing defect atoms in a semiconductor and therefore, the building blocks of semiconductor are relatively large blocks of material with a specific doping. These blocks obviously consist of many atoms. When designing a "doped" PhC, one can precisely position and fabricate all defects with a high degree of freedom – at least it is expected that this can be done in the near future [2].

Although the variety of PhC structures that might be fabricated one day seems to be almost infinite and although many interesting structures were already proposed (various types of waveguides, sharp bends in waveguides without any reflection, couplers, resonators, etc.) or even fabricated on a prototype level, one currently cannot say what kind of PhC structures will be favored. At the moment, one can neither know the materials that are best suited for PhCs – it is well known that a large dielectric contrast is required for obtaining a bandgap, which somehow limits the materials that may be used, but there is no unique choice at all – nor what kind of geometry (2D crystals or 3D crystals [3]-[5], symmetry, shape of the scatterers) is most appropriate. Thus, there is a strong need for theoretical investigations and simulations of potential structures. The first step of such investigations consists in the computation of the band diagrams of perfect PhCs without any defects. The goal is to find structures that may easily be fabricated and exhibit a broad band gap, i.e., a frequency range where no electromagnetic waves are allowed to propagate within the crystal. In order to find the band gap, one must compute the band diagram of the lowest order modes of the PhC. This is essentially an eigenvalue problem that exhibits several special cases that may cause difficult numerical problems, especially when one is designing a procedure for the automatic, efficient, accurate, and reliable computation of the complete band diagrams for arbitrary structures.

Currently, the most frequently used approach is the Plane Wave Method (PWM) that mainly approximates the electromagnetic field by a superposition of plane waves [6]-[10]. It is well known, that this method has a problematic convergence [11]-[13],[10]. Other methods that were used for PhCs are the Finite Difference Time Domain (FDTD) [14], [15], the transfer matrix method [16], the Finite Element Method (FEM) [17], and the Boundary Element Method (BEM) [18]. In the following, we apply the latest version of the Multiple Multipole Program (MMP) [19] implemented in the MaX-1 software [20].

In order to obtain efficient, reliable, and accurate results, we carefully analyze the numerical problems that may occur and introduce several new techniques. For reasons of simplicity we focus on the 2D case.

1054-4887 © 2004 ACES

The remainder of the paper is organized as follows: A commonly used representation of PhCs in terms of their band diagram is elucidated in Section II. In Section III we briefly explain the core of our photonic crystal calculations, when MMP is considered. The proper framework of the eigenvalue search is reported in Section IV, whereas in Section V a successful automation of such search procedure is proposed. A validation of our band structure calculation by means of various test examples is given in Section VI. And finally, we conclude this contribution with a short summary in Section VII.

II. DEFINITION OF THE BAND DIAGRAM

As an introductory example let us consider the simple case of a 2D PhC consisting of dielectric rods arranged in a square lattice and embedded in, e.g., air. For periodic structures it is possible to apply some fundamental theorems from solid state physics. The original lattice for this crystal is given on the left hand side of Fig. 1. For the dielectric constant we can write $\varepsilon(\vec r) = \varepsilon(\vec r + \vec R)$ where $\vec R$ is one of the original lattice vectors. According to Bloch's theorem [6], [7] for the modal field inside the crystal we write

$$\vec E = \vec E_{\vec k n}(\vec r) = \vec u_{\vec k n}(\vec r) \cdot e^{i\vec k \vec r}\ , \tag{1}$$

$$\vec u_{\vec k n}(\vec r) = \vec u_{\vec k n}(\vec r + \vec R)\,. \tag{2}$$

Note that (1) holds not only for the electric but also for the magnetic field. Bloch's theorem may be proven in classical electrodynamics [6]. Important consequences of this theorem are [6], [7]

1. $e^{i\vec k\cdot\vec R} = 1$, i.e., $\vec k \cdot \vec R = N \cdot 2\pi$, where N is an integer – the wave vector space (reciprocal space) is discrete,
2. $\vec E_{\vec k,n}(\vec r) = \vec E_{\vec k+\vec G,n}(\vec r)$, i.e., the reciprocal space is periodic. $\vec G$ is one of the reciprocal lattice vectors.

This allows us to define the so-called reciprocal lattice space, spanned by the reciprocal lattice vectors. We first define the original lattice vectors as follows

$$\vec R = \eta_1 \vec e_1 + \eta_2 \vec e_2 + \eta_3 \vec e_3 \tag{3}$$

where $\vec e_1$, $\vec e_2$, $\vec e_3$ are three independent lattice vectors and η_1, η_2, η_3 are integer numbers. Note that $\vec e_3$ is missing in 2D crystals. Similarly, we write for the primitive reciprocal lattice vectors

$$\vec G = \kappa_1 \vec f_1 + \kappa_2 \vec f_2 + \kappa_3 \vec f_3\,. \tag{4}$$

If we want to construct the reciprocal lattice, we can use [7]

$$\vec f_1 = 2\pi \frac{\vec e_2 \times \vec e_3}{\vec e_1 \cdot (\vec e_2 \times \vec e_3)},\quad \vec f_2 = 2\pi \frac{\vec e_3 \times \vec e_1}{\vec e_1 \cdot (\vec e_2 \times \vec e_3)},\quad \vec f_3 = 2\pi \frac{\vec e_1 \times \vec e_2}{\vec e_1 \cdot (\vec e_2 \times \vec e_3)}\,.$$

These equations are derived from the definition of the reciprocal lattice vector space. For 2D crystals (cylindrical geometry), the vector $\vec f_3$ is omitted and the vector $\vec e_3$ is the unit vector $\vec e_z$ along the cylinder axis.

From the equations above, we can conclude that the discrete translational symmetry of a photonic crystal leads to the fact that modes with the wave vector $\vec k$ and modes with the wave vector $\vec k + \vec G$ are identical, i.e., we have periodicity also in the reciprocal space. A special representation of the primitive cell for this periodicity is called the first Brillouin zone (1^{st} BZ). It can be defined as a zone around any lattice point in the reciprocal space with points that are closer to this lattice point than to any other lattice point.

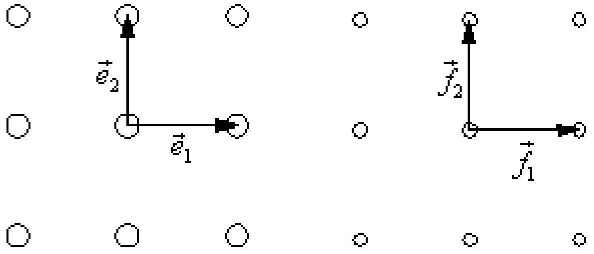

Fig. 1: The original (left) and reciprocal (right) lattice for a 2D photonic crystal (square lattice). Construction details for reciprocal lattice are given in the text.

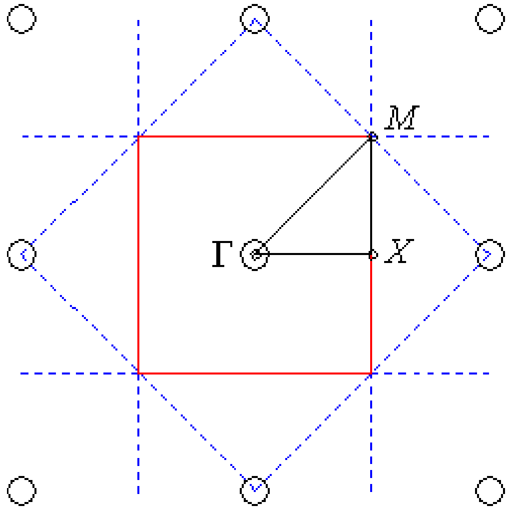

Fig. 2: Construction of the 1^{st} Brillouin zone (solid square), its irreducible part (triangle Γ-X-M) and characteristic points for band structure computation (Γ, X, and M).

The Brillouin zone construction (using Bragg's planes – dashed lines) for the square lattice is shown in Fig. 2. Because of the high degree of symmetry, we need to analyze only a small part of the 1^{st} BZ. This part is called the *irreducible BZ* (IBZ), [6], [7]. In the case of periodic structures, it is sufficient to perform the modal field analysis in the area of the IBZ. As illustrated in Fig. 2 the IBZ for a square lattice is a triangle with the corners Γ, X, and M. Since the maxima and minima of the eigenvalues (resonance frequencies) are supposed to be on the borders of the IBZ, it is sufficient to trace the eigenvalues along the sides of the IBZ in order to get the photonic bandgaps. Therefore, the standard band diagram consists of three sections: Γ–X, X–M, and M–Γ (see Fig. 5). For other lattices, the procedure is essentially the same [21],

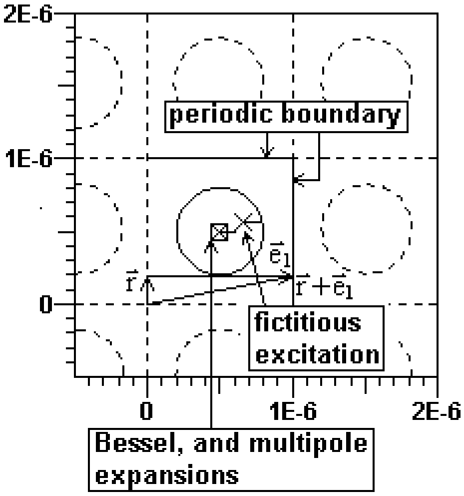

Fig. 3: The unit cell of the photonic crystal with dielectric rods arranged on a square lattice.

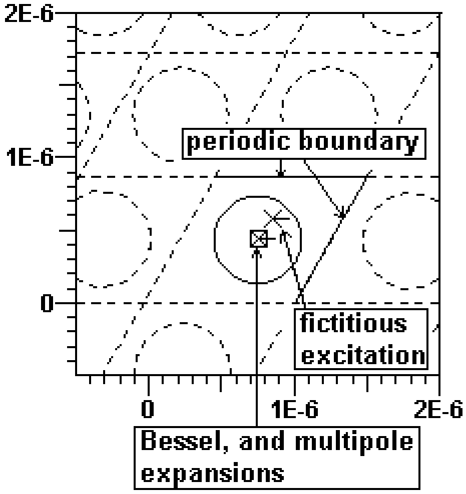

Fig. 4: The unit cell of the photonic crystal with dielectric rods arranged on a hexagonal lattice.

[22]. Assume that an arbitrary point in the reciprocal space is considered. This point essentially defines a wave vector. For the periodicity of (3) we then obtain for the field in the original space

$$\vec{F}(\vec{r}+\vec{R})=\vec{F}(\vec{r})\cdot e^{i\,\vec{k}\cdot\vec{R}}=\vec{F}(\vec{r})\cdot e^{i\,(C_1\,\eta_1\,|\vec{e}_1|+C_2\,\eta_2\,|\vec{e}_2|)} \tag{5}$$

where *F* stands for the electric as well as for the magnetic field. In the MMP implementation of the periodic boundary problem C_1, C_2 are parameters that characterize the point in the reciprocal lattice space. As a consequence, it is sufficient to know the field in a unit cell (as an equivalent representation of the primitive cell) of the original space. Let us call this the original cell. Note that neither the shape nor the location of the original cell is unique, but for both the square and the hexagonal lattice we may simply use quadrangular original cells as shown in Figs. 3 and 4.

For the square lattice, the relation between the periodic constants (C_1, C_2) and the position in the IBZ is very straight forward, i.e., these are the Cartesian components (C_x, C_y) of the wave vector $\vec{k}$. For the hexagonal lattice, the situation is a bit more complicated [23]-[25].

III. THE MMP SOLUTION OF PERIODIC PROBLEMS WITH FICTITIOUS BOUNDARIES

Any software for computing band diagrams must handle both eigenvalue problems and periodic structures. The MMP implementation of MaX-1 contains a simple concept for handling arbitrary periodic structures: First, the structure is subdivided into cells by an appropriate grid of fictitious boundaries (dashed lines in Fig. 3 and Fig. 4). Assume that the field in one of the infinitely many cells is known, then, the field in all other cells is easily obtained from the periodicity conditions (5), i.e., the Floquet theorem [7].

The geometric shape of the original cell depends on the crystallographic structure (i.e. the crystal symmetry), but it is not unique for a given crystallographic structure at all, because the fictitious boundaries we have introduced, are quite ambiguous. For example, in Fig. 3 we used straight lines between the circular rods. We could replace these lines by curved, periodic lines and we could move these lines to any other position in space. Since we will impose so-called periodic boundary conditions along the fictitious boundaries of the original cell, we have to minimize the numerical problems when we select the fictitious boundaries in such a way that the electromagnetic field along them is as well behaved as possible. Therefore, straight lines in the middle between neighbor rods are most reasonable when the rods are circular or rectangular. When the geometric shape of the rods is more complicated, it may be advantageous to use curved lines.

Once, the original cell is isolated by introducing fictitious boundaries, we can derive boundary conditions for the field along them. In 2D PhCs, the original cell is bounded by two pairs of parallel lines. For example, when $\vec{r}$ is a point on the left border of the original cell in Fig. 3, $\vec{r}+\vec{e}_1$ is the corresponding point on the right border, where $\vec{e}_1$ corresponds to one of the primitive lattice vectors. Because of the periodicity, we obtain from (5)

$$\vec{F}(\vec{r}+\vec{e}_1)=\vec{F}(\vec{r})\cdot e^{i\,(C_1\,|\vec{e}_1|)}\,. \tag{5'}$$

This condition holds for both the electric and the magnetic field in every point along the right boundary of the original cell. We call this the periodic boundary condition that is imposed on the right border of the original cell. Similarly, we can introduce a periodic boundary condition for the upper border.

Having defined the original cell and its periodic boundary conditions, one has to set up the MMP model of the scattering body in the lattice point: We approximate the field in each domain by a superposition of multipole expansions and sometimes by additional, analytic solutions of Maxwell's equations (in the frequency domain). The amplitudes or parameters of the resulting series expansions are then computed with the generalized point matching technique, i.e., by minimizing a weighted error function defined along all natural and fictitious boundaries. For example, for the simple geometry in Fig. 4 we use the following expansions

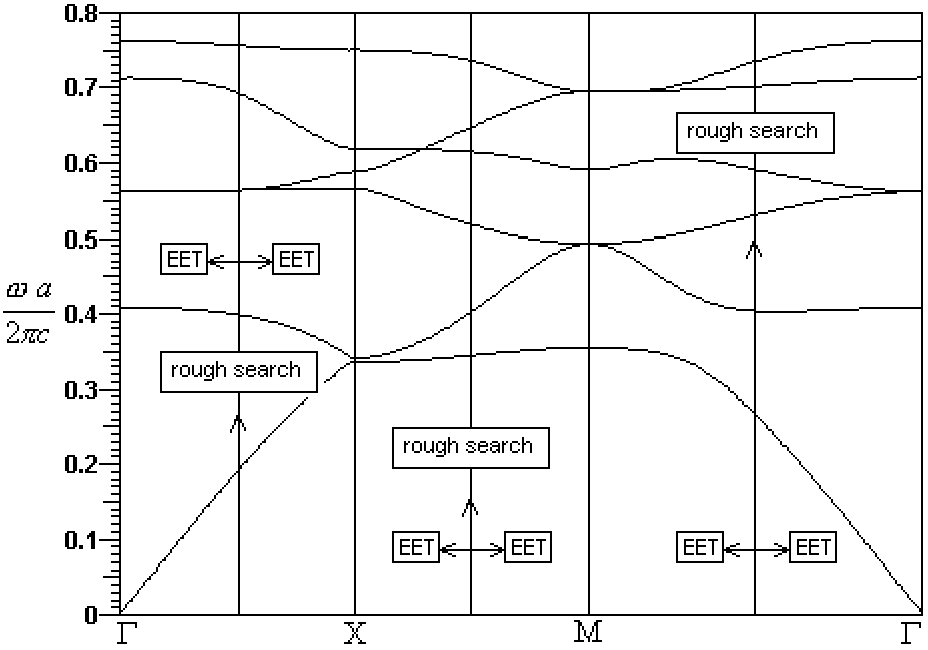

Fig. 5: The band diagram of the photonic crystal with dielectric rods on a square lattice (for H-polarization).The algorithms used within the eigenvalue search procedure are labeled correspondingly.

$$E_z = \sum_{n=0}^{N} A_n^E J_n(\kappa r)\cos(n\varphi) + B_n^E J_n(\kappa r)\sin(n\varphi)\,, \tag{6}$$

$$H_z = \sum_{n=0}^{N} A_n^H J_n(\kappa r)\cos(n\varphi) + B_n^H J_n(\kappa r)\sin(n\varphi)\,, \tag{7}$$

$$E_z = \sum_{n=0}^{N} C_n^E H_n^1(\kappa r)\cos(n\varphi) + D_n^E H_n^1(\kappa r)\sin(n\varphi)\,, \tag{8}$$

$$H_z = \sum_{n=0}^{N} C_n^H H_n^1(\kappa r)\cos(n\varphi) + D_n^H H_n^1(\kappa r)\sin(n\varphi)\,, \tag{9}$$

where J_n is Bessel function of order n, H_n^1 is Hankel function of first kind and order n, κ is transverse propagation constant and (r,φ) are polar coordinates with respect to the origin at the position of the corresponding expansion. Expansion (6) (Bessel expansion) is used in the case of E-polarization and expansion (7) is used in the case of H-polarization. These Bessel expansions are used for the domain inside of the dielectric rod because these functions have no singularity at origin. Furthermore, these expansions are sufficient because the domain is simply connected. The background domain is not simply connected, because it contains a hole. Therefore, we need at least two different expansions, namely a multipole expansion (8) or (9) and Bessel expansion (6) or (7). Note that the moltipole expansion essentially accounts for the field scattered at the inner boundary, whereas the Bessel expansion accounts for the outer, ficitious boundaries. This means that the Bessel expansion simulates the field that comes from all rods outside the original cell. According to Vekua [24], our set of expansions is complete in the sense that the error of the field is below an arbitrarily small value ε provided that the highest orders are big enough and provided that the amplitudes (A, B, C, D in (6)-(9)) are computed correctly.

IV. THE MMP-MAS EIGENVALUE SOLVER

For obtaining the band diagram of a PhC, it is necessary to solve an eigenvalue problem, because there is no excitation like in scattering problems. This means that we only obtain non-trivial solutions (i.e. frequencies) for an arbitrary point of the IBZ (i.e., for a given set of complex values C_1, C_2). Thus, we essentially have a periodic resonator problem to solve. The search of resonance frequencies in the MMP code MaX-1 is somehow different from many other numerical methods because MMP uses a full rectangular system matrix obtained from the generalized point matching technique. For such type of matrix it is very demanding to obtain accurate results while avoiding problems with the condition number [25]. Note that condition number problems are especially crucial when one is solving eigenvalue problems. If this is not properly done, one can obtain a "noisy" behavior near the eigenvalues and this can heavily disturb the numerical eigenvalue search procedures. However, the standard MMP eigenvalue search procedure first defines a real valued, positive eigenvalue search function

$$\eta(e) = \frac{\|E(e)\|^2}{A^2(e)} \tag{10}$$

where e is the eigenvalue (i.e. the resonance frequency), E is the weighted residual, and A is an amplitude that may be retrieved from any field component in a specific test point (or an integral over some field profile). For the band gap computation, it is most reasonable to define A^2 as the total electromagnetic energy within the original cell. According to (10) the desired eigenvalues are characterized by the minima of the search function η. Analyzing the shape of η near the minima provides additional information on the accuracy of the solution.

Although more reliable results are obtained when the amplitude is defined by an appropriate integral, the definition in one or a few test points is sufficient for most cases. Since the numerical intergration may be time-consuming, one usually prefers the simpler test point method. However, it is important to note that the definition of the search function is not unique. By defining different search functions, one can gain even more intrinsic information providing a good error estimation and for validation purposes. As depicted in Fig. 6, even for a single model (fixed amplitude definition and fixed multipole expansion), one can address the different minima of the same eigenvalue search functions simply by rearranging the columns of the MMP matrix. In fact, in the Givens update algorithm [25], which was used for solving the MMP matrix equation, the last expansion somehow plays the role of an excitation. When it happens that the spatial symmetry of such excitation is not contained in the symmetry of the searched eigenmode, this mode will not be "excited", hence, the corresponding minimum of the eigen-value search function is suppressed. Although, it may be desirable to suppress some modes in applications where not all modes must be considered, this is usually inconvenient for the automatic computation of the complete band structure. We therefore look for an alternative technique.

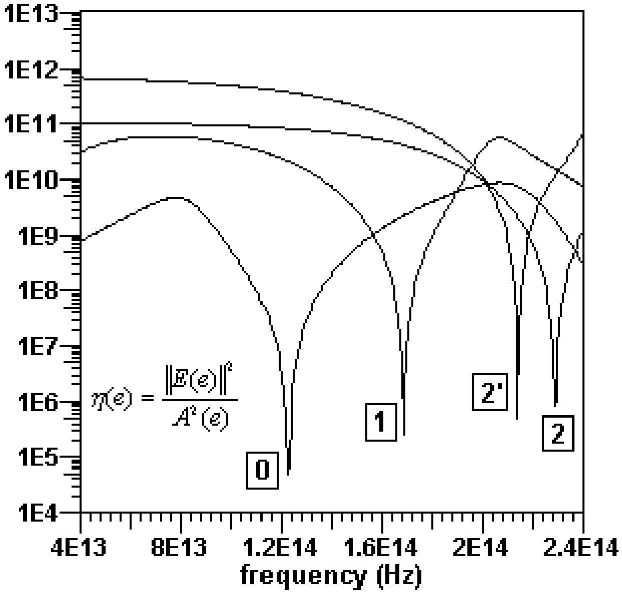

Fig. 6: The behavior of the eigenvalue search function (in the Γ point) of one single model with four different “last” expansions (the order of the last expansion is labelled in the figure).

Remember that we have introduced fictitious boundaries for handling the periodic problem. Similarly, we now can introduce a fictitious excitation that is defined in such a way that all modes are excited (Fig. 7). This concept mimics the measurement of resonance frequencies, where one always needs an excitation of the resonator and a test point (or port) where the signal is measured. By sweeping the frequency of the exitation, the peaks of the amplitude *A* in the test point can be readily assigned to the resonance frequencies of the different modes. This procedure was first introduced by the Method of Auxiliary Sources (MAS) [26] and a similar method was used by Sakoda [27]. Finally, the method was adapted to MMP by Moreno [28]. MAS uses eigenvalue search functions μ such as the energy density A^2 at the test point are used. The eigenvalues are then obtained from the maxima of μ. The analysis of μ near the maxima has yielded a strange "double peak" phenomenon that disturbs the numerical search procedure. The standard MMP-MAS eigenvalue solver searches for minima of the eigenvalue search function $\eta = 1/\mu = 1/A^2$, i.e., one obtains "twin minima" instead of double peaks, as shown in Fig. 8. The "double peak" phenomenon and the "twin minima" are caused by a very sharp peak of the residual *E* at the correct eigenvalue position. Note that this peak is not obtained in the standard MMP approach without fictitous excitations. Of course, the residual peak may also be used for defining the eigenvalues. Since

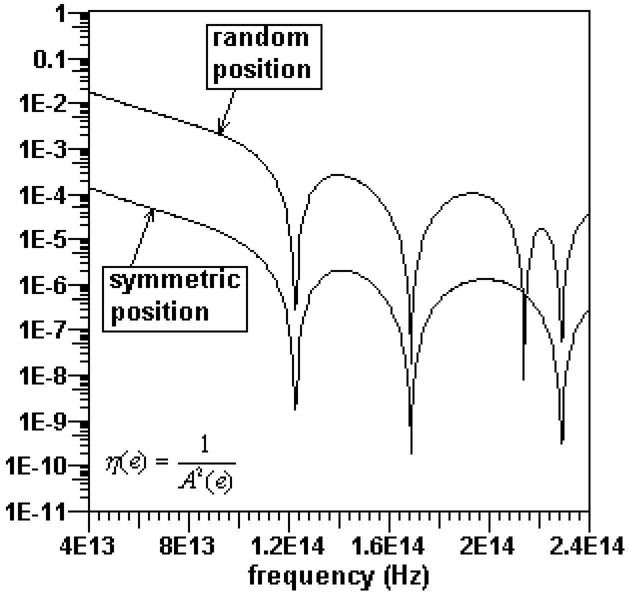

Fig. 7: The behavior of the eigenvalue search function (for a k-vector in the Γ point) using the fictitious excitation in a random and symmetric position respectively.

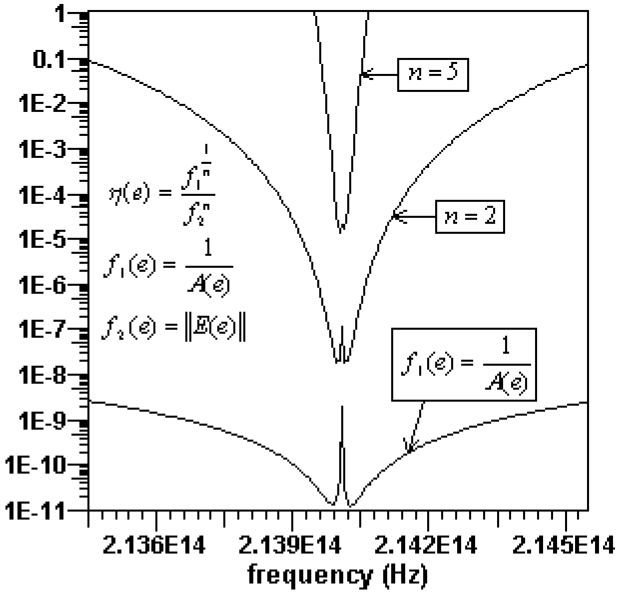

Fig. 8: The “twin minima” phenomenon, behavior of the eigenvalue search function within the eigenvalue search procedure using a randomly located fictitious excitation.

these peaks are extremely sharp, it is very likely that one of the eigenvalues is missed by the rough search routine that searches for all eigenvalues. In order to overcome these problems, one can define more complicated eigenvalue search functions η as proposed in Fig. 8. This allows one to suppress the double peak phenomenon. Unfortunately, one may encounter numerical underflow problems in some applications. Therefore, the current MaX-1 eigenvalue solvers uses three different "competing" eigenvalue search functions: 1) A complicated one with user-definable exponent *n*, 2) the inverse of the amplitude, and 3) the proper residual. Using all of these three functions, the code is capable to detect the correct locations of the eigenvalues. An alternative to overcome the twin minima problems is the introduction of "fictitious losses" that smoothen the resulting search function η.

Since one often considers a broad frequency range, it is not reasonable to find the eigenvalues by plotting the eigenvalue search function over the entire range with a very high resolution. It is much more efficient to subdivide the search process into two steps: 1) Rough detection of all eigenvalues and 2) fine search, i.e., accurate computation of the eigenvalues. The first step seems to be trivial as soon as the problems mentioned above have been solved. The second step requires a fast minimum search procedure for real functions. The algorithm used in MaX-1 is mainly based on a parabolic interpolation because the search function near the minima is usually almost parabolic – provided that the double peak phenomenon has been removed.

Having a closer look to typical band diagrams (Fig. 3), we see different situations which can cause problems for both the rough search and the fine search. Mainly at the Γ and the M point we usually observe degenerate modes. Furthermore, we have areas with almost degenerate modes and points where different lines seem to cross each other, where the modes are (accidentally) degenerated. When the rough search is performed to degenerate points, it usually cannot detect all modes involved. Even if the search procedure is started in a close vicinity to such degeneracies, it will be too time-consuming to iterate into all eigenmodes. In order to overcome these problems, it is reasonable to start a rough search in a domain where all eigenvalues could be easily tracked down (e.g. the interval between Γ and X in the band diagram of Fig. 5). Once this has been done, one can trace each eigenvalue by moving a small step either to the left or right side within the band diagram, and

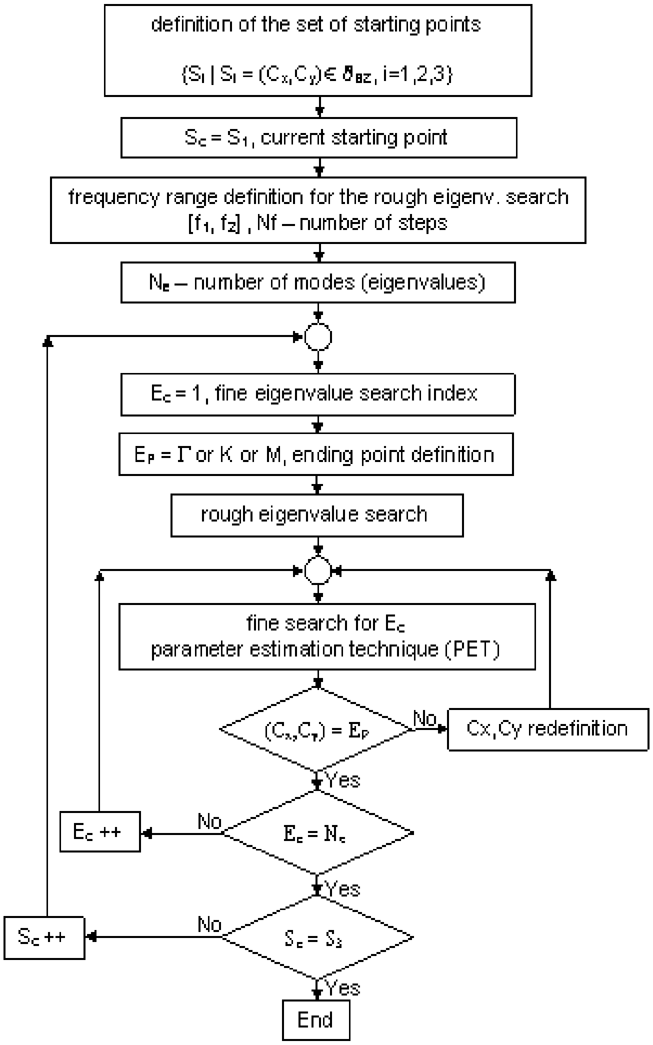

Fig. 9: The algorithm for the band structure computation using MMP.

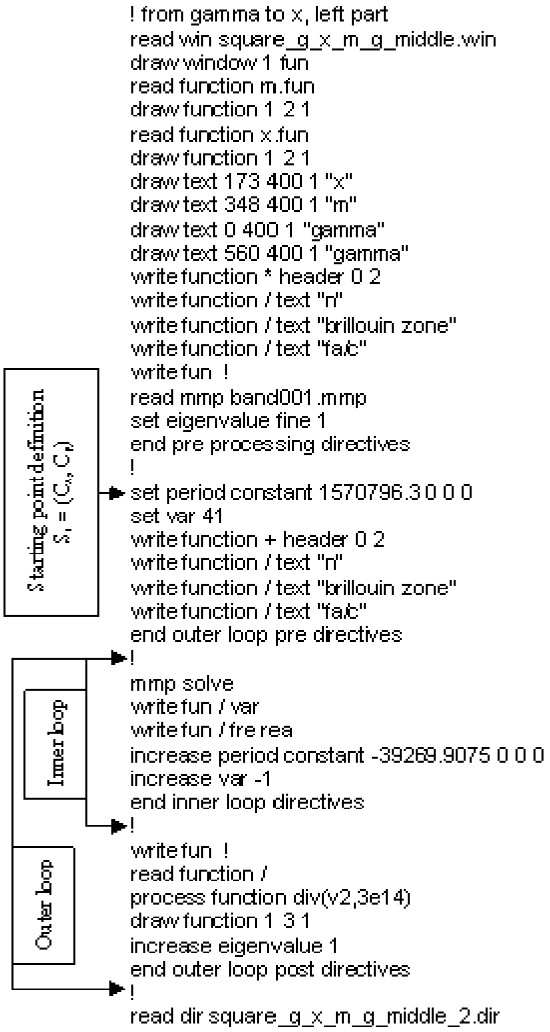

```
! from gamma to x, left part
read win square_g_x_m_g_middle.win
draw window 1 fun
read function m.fun
draw function 1 2 1
read function x.fun
draw function 1 2 1
draw text 173 400 1 "x"
draw text 348 400 1 "m"
draw text 0 400 1 "gamma"
draw text 560 400 1 "gamma"
write function * header 0 2
write function / text "n"
write function / text "brillouin zone"
write function / text "fa/c"
write fun !
read mmp band001.mmp
set eigenvalue fine 1
end pre processing directives
!
set period constant 1570796.3 0 0 0
set var 41
write function + header 0 2
write function / text "n"
write function / text "brillouin zone"
write function / text "fa/c"
end outer loop pre directives
!
mmp solve
write fun / var
write fun / fre rea
increase period constant -39269.9075 0 0 0
increase var -1
end inner loop directives
!
write fun !
read function /
process function div(v2,3e14)
draw function 1 3 1
increase eigenvalue 1
end outer loop post directives
!
read dir square_g_x_m_g_middle_2.dir
```

Fig. 10: The algorithm for band diagram computation written in the MaX-1 script language.

TABLE I
CONVERGENCE CHARACTERISTICS, COMPUTATION FOR 1^{ST} AND 6^{TH} EIGENFREQUENCY AT X POINT OF IBZ

Number of unknowns	Eigenfrequency 1			Eigenfrequency 6		
	Frequency (Hz)	Error (%)	Field mismatch. (%)	Frequency (Hz)	Error (%)	Field mismatch. (%)
20	1.0223585e14	1.473	9.620748e-0	2.3465308e14	4.194	2.306028e+1
36	1.0095955e14	0.206	4.204639e-0	2.2567438e14	0.207	4.449937e+0
52	1.0078338e14	0.032	0.288115e-0	2.2512072e14	0.039	0.824365e-0
94	1.0074678e14	0.005	4.465747e-2	2.2519421e14	0.006	0.128581e-0
164	1.0075153e14	0.000	4.729721e-7	2.2520785e14	0.000	3.551224e-6

repeating this procedure until the border of the diagram is reached. For each such step, only a fine search must be performed. Depending on 1) the desired accuracy, 2) the step size, and 3) special properties of the model, several iterations are required. The number of iterations could be drastically reduced when using the Eigenvalue Estimation Technique (EET) implemented in MaX-1 [19]. This technique uses the information of previous eigenvalue solutions for the extrapolation of the current eigenvalue's search interval. Typically, 4–12 iterations per step are sufficient for obtaining an eigenvalue with a high precision. For example, for tracing the first mode in Fig. 3, 280 search steps were performed and 5 iterations per step were required in the average.

V. AUTOMATIC EIGENVALUE SEARCH

Referring to e.g. Fig. 5 a standard band diagram consists of three different intervals corresponding to the three sides of the IBZ. When the rough search is started somewhere in the middle of such an interval (e.g. in the area between Γ and X in the band diagram), it must be repeated three times. After each rough search the fine search must be repeated for each obtained eigenvalue and, finally, the fine search routine must run for each eigenvalue once towards the left and once towards the right side of the band diagram, as depicted in Fig. 5. MaX-1 contains a script language that allows one to define complicated procedures such as the search procedure mentioned above. The set of MaX-1 directives for the automatic generation of a band diagram from the point in the middle between Γ and X to the Γ point, is given in Fig. 10, and the complete algorithm for this procedure is given in Fig. 9. It is obvious that the algorithm is not simple and the overall procedure relies on fast computer resources.

VI. NUMERICAL VERIFICATION

We have applied MMP to various PhC lattices. Internal tests show excellent convergence. Therefore high accuracy may easily be obtained. Table I shows the MMP estimate of the mismatching errors along the boundary for the model outlined

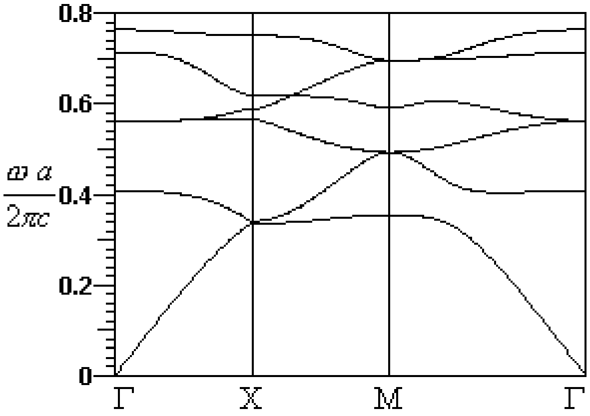

Fig. 11: The band diagram of the photonic crystal with dielectric rods and square lattice, H-polarization, the first 6 modes.

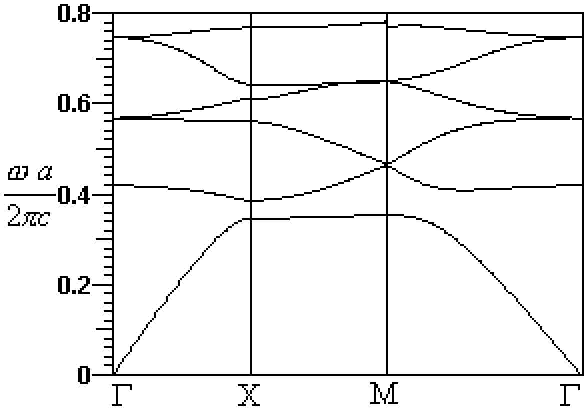

Fig. 13: The band diagram of the photonic crystal with dielectric rods and hexagonal lattice, H-polarization, the first 6 modes.

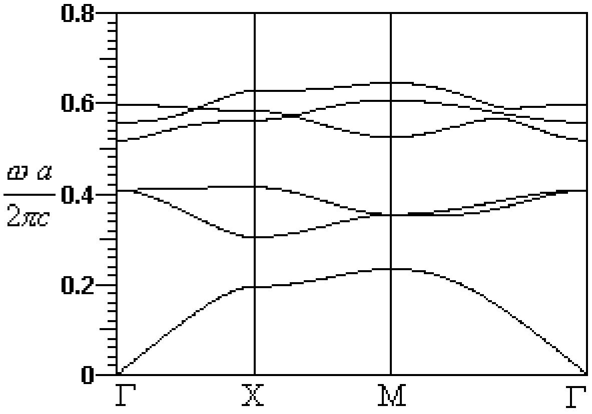

Fig. 12: The band diagram of the photonic crystal with dielectric rods and square lattice, E-polarization, the first 6 modes.

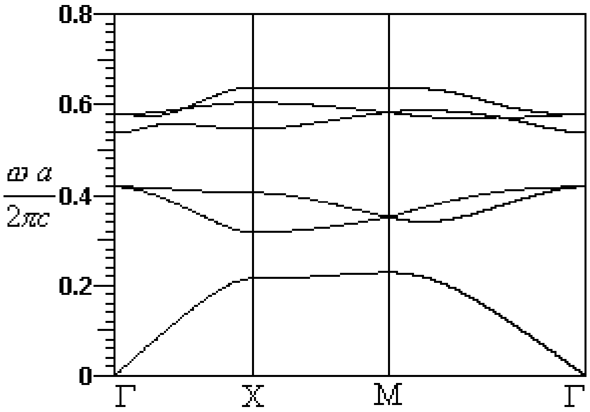

Fig. 14: The band diagram of the photonic crystal with dielectric rods and hexagonal lattice, E-polarization, the first 6 modes.

in Fig. 3 with different maximum orders of the multipoles and Bessel expansions, i.e., with different numbers of unknowns. Note that the computation time typically is proportional to the cube of the number of unknowns because we use a brute-force full matrix solver (Givens update scheme). Despite of this, the computation time remains reasonably short because the matrices obviously are much smaller than the matrices used in other methods. For example Fig. 11 was obtained with 3 rough-search routines, 100 frequency steps each. The total number of 1656 plotted points required were then computed with 8280 MMP evaluations of η, i.e. approximately 5 iterations per point in the diagram were performed. The total calculation time was 40 minutes on a Pentium 4, 2GHz. Because of the excellent convergence, we also can estimate the accuracy of the eigenvalues by comparing them with a very accurate MMP model. As one can see from Table I, one only obtains one more digit when doubling the number of unknowns.

In order to validate this algorithm, several calculations were performed and results were compared with the results of MPB package developed at the MIT [29]. For the PhC with square lattice and dielectric rods (Fig. 3), a band diagram calculation was performed for different field polarizations and the results are given in Fig. 11 (H-polarization) and Fig. 12 (E-polarization). The results for the hexagonal lattice case (Fig. 4), are depicted in Fig. 13 (H-polarization) and Fig. 14 (E-polarization). These two types of PhC rely on the same lattice data: A dielectric rod with radius $r = 0.3a$ and a dielectric constant of $\varepsilon = 11.56$, the lattice is embedded in air and the lattice constant is $a = 10^{-6}(m)$. From Figs. 11–14 we deduce a perfect agreement with the MPB results documented in [29].

VII. CONCLUSION

We have presented an efficient method for band structure calculation for 2D dielectric PhCs. In this framework a fully automatic algorithm was developed and evaluated along several examples. The eigenvalue searching procedure in the frequency domain has been performed using a fictitious excitation. Optimal eigenvalue search functions have been found while evaluating the total eigenvalue spectrum for k-values at three preferable points on the IBZ. The three resulting sets of eigenvalues are evolved into a full band diagram using a highly efficient Eigenvalue Estimation Technique (EET). The overall algorithm performs photonic band diagram calculations at a very high level of accuracy and at reasonable computational costs. This algorithm is easily extendable for applications involving localized defect mode analysis [30], various PhC defect waveguide types (supercell approach [31]) and photonic waveguide discontinuities [31], as well.

ACKNOWLEDGMENT

This work was supported by the Swiss National Science Foundation in the framework of the project NFP-2000-065102.01/1 and the research initiative NCCR Quantum Photonics.

REFERENCES

[1] E. Yablanovich, "Inhibited spontaneous emission in solid-state physics and electronics", *Phys. Rev. Lett.*, **58**, pp. 2059-2062, 1987.

[2] J. Mills, "Photonic crystals head toward the marketplace", Nov. 2002, http://optics.org/articles/ole/7/11/1/1 ,

[3] K. Busch, S. John, "Liquid-crystal photonic-band-gap materials: the tunable electromagnetic vacuum", *Phys. Rev. Letters,* **83**, pp. 967-970, 1990.

[4] A. Figotin, Y. A. Godin, "two-dimensional tunable photonic crystals", *Phys. Rev. B*, **57**, pp. 2841-2848, 1998.

[5] R. L. Sutherland, V. P. Tondiglia, L. V. Natarajan, S. Chandra, "Switchable orthorombic F photonic crystals formed by holographic polymerization-induced phase separation of liquid crystal", Optics Express, **10**, pp. 1074-1082, 2002.

[6] K. Sakoda, "Optical Properties of Photonic Crystals",Springer, Berlin, 2001.

[7] J. D. Joannopoulos, R. D. Meade, J. N. Winn, "Molding the Flow of Light", Princeton University Press, 1995.

[8] K. M. Ho, C. T. Chan, and, C. M. Soukolis, "Existance of a Photonic Gap in Periodic Dielectric Structures", *Phys. Rev. Lett.,* **65**, pp. 3152-3155, 1990.

[9] S. G. Johnson, and J. D. Joannopoulos, "Block-iterative frequency-domain methods for Maxwell's equations in a planewave basis", *Opt. Express,* **8**, pp. 173-190, 2001.

[10] R. D. Meade, A. M. Rappe, K. D. Brommer, J. D. Joannopoulos, and O. L. Alerhand, "Accurate theoretical analysis of photonic band-gap materials", *Phys. Rev. B*, **48**, pp. 8434-8437, 1993.

[11] H. S. Söuzüer, J. W. Haus, and R. Inguva, "Photonic bands: Convergence problems with the plane-wave method", *Phys. Rev. B*, **45**, pp. 13962-13972, 1992.

[12] D. Hermann, M. Frank, K. Busch and P. Wölfle, "Photonic band structure computations", *Opt. Express,* **8**, pp. 167-172, 2001.

[13] K. Ohtaka, T. Ueta, and K. Amemiya, "Calculation of photonic bands using vector cylindrical waves and reflectivity of light for an array of dielectric rods", *Phys. Rev B*, **57**, pp. 2550-2568, 1998.

[14] C. T. Chan, Q. L. Yu, and K. M. Ho, "Order-N spectral method for electromagnetic waves", *Phys. Rev B,* **51**, pp. 16 635-16 642, 1995.

[15] M. Qui and S. He, "A non-orthogonal finite-difference time-domain method for computing the band structure of a two-dimensional photonic crystal with dielectric and metallic inclusions", *J. Appl. Phys.*, **87**, pp. 8268-8275, 2000.

[16] J. B. Pendry and A. MacKinnon, "Calculation of Photon Dispersion Relations", *Phys. Rev. Lett.,* **69**, pp. 2772-2775, 1992.

[17] W. Axmann and P. Kuchment, "An efficient finite element method for computing spectra of photonic and acoustic band-gap materials", *J. Comput. Phys.,* **150**, pp. 468-481, 1999.

[18] P. A. Knipp, and T. L. Reinecke, "Boundary-element calculations of electromagnetic band-structure of photonic crystals", *Physica E,* **2**, pp. 920-924, 1998.

[19] Ch. Hafner, "Post-modern Electromagnetics Using Intelligent MaXwell Solvers", John Wiley & Sons, 1999.

[20] Ch. Hafner, "MaX-1: A visual electromagnetics platform", John Wiley & Sons, 1998.

[21] P. R. Villeneuve and M. Piche, "Photonic band gaps in two-dimensional square and hexagonal lattices", *Phys. Rev. B*, **46**, pp. 4969-4972, 1992.

[22] M. Plihal and A. A. Maradudin, "Photonic band structure of two-dimensional systems: the triangular lattice", *Phys. Rev. B,* **44**, pp. 8565-8571, 1991.

[23] Ch. Hafner, J. Smajic, The Computational Optics Group Web Page (IFH, ETH Zurich), http://alphard.ethz.ch/.

[24] I. N. Vekua, "New methods for solving elliptic equations", North-Holland, Amsterdam, 1967.

[25] G. H. Golub and C. F. Van Loan, "Matrix Computations", John Hopkins University Press, Baltimore, 1996.

[26] F. G. Bogdanov, D. D. Karkashadze, and R. S. Zaridze, in "Generalized Multipole Techniques for Electromagnetic and Light Scattering", edited by T. Wriedt, pp. 143-172, Elsevier, Amsterdam, 1999.

[27] K. Sakoda, N. Kawai, T. Ito, A. Chutinan, S. Noda, T. Mitsuyu, and K. Hirao, "Photonic bands of metallic systems. I. Principle of calculation and accuracy", *Phys. Rev. B*, **64**, pp. 045116, 2001.

[28] E. Moreno, D. Erni and Ch. Hafner, "Band structure computations of metallic photonic crystals with the multiple multipole method", *Phys. Rev. B,* **65**, pp. 155120: 1-10, 2002.

[29] S. G. Johnson and J. D. Joannopoulos, The MIT Photonic-Bands Package home page, http://ab-initio.mit.edu/mpb/ .

[30] R. D. Meade, K.l D. Brommer, A. M. Rappe and J. D. Joannopoulos, "Photonic band states in periodic dielectric materials", *Phys. Rev. B,* **44**, pp. 13 772 – 13 774, 1991.

[31] E. Moreno, D. Erni and Ch. Hafner, "Modeling of discontinuities in photonic crystal waveguides with the multiple multipole method", *Phys. Rev. B,* **66**, pp. 036618, 2002.

Jasmin Smajic was born in Tuzla, Bosnia and Herzegovina, in 1971. He received a Dipl. El.-Ing. degree from Faculty of Electrical Engineering, Tuzla in 1996. Since 1996 he has been working at the Faculty of Electrical Engineering in Tuzla on numerical calculation of electromagnetic field, numerical mathematics and optimization. He got a M.Sc. degree in 1998 from the Faculty of Electrical Engineering and Computing in Zagreb, Croatia, for the analysis of magnetic field in non-linear material. He received a Ph.D. in 2001 from Faculty of Electrical Engineering and Computing in Zagreb, Croatia, for numerical calculation of time-varying field in non-linear material and electrical machine design optimization. Since 2002 he is a postdoctoral research fellow in the Computational Optics group of the Laboratory for Electromagnetic Fields and Microwave Electronics at the ETH Zurich. His current research interest includes numerical field calculation and design optimization of photonic crystal devices.

Christian Hafner was born in Zurich, Switzerland, in 1952. He received a Dipl. El.-Ing. Degree, Doctoral Degree, and Venia Legendi from Swiss Federal Institute of Technology (ETH), Zürich in 1975, 1980, and 1987 respectively. In 1999 he was given the title of Professor.

Since 1976 he has been working at the ETH on the development of methods for computational electromagnetics and for optimization problems. He has developed the Multiple Multipole Program (MMP), the MaX-1 package, the Generalized Genetic Programming (GGP) code, and various optimization codes. He worked on various applications (electrostatics, EM scattering, antenna, waveguides and waveguide discontinuities, gratings, chiral media, etc.). His current focus is on photonic crystals, microstructured optical fibers, and Scanning Nearfield Optical Microscoes (SNOM). In 1990 he obtained the second prize of the Seymour Cray avard for scientific computing and in 2001 he has been awarded the 2000 Outstanding Journal Paper Award by the Applied Computational Electromagnetics Society. He is member of the Electromagnetics Academy.

Daniel Erni was born in Lugano, Switzerland, in 1961. He received an El.-Ing. HTL degree from Interkantonales Technikum Rapperswil HTL in 1986, and a Dipl. El.-Ing. degree from Swiss Federal Institute of Technology (ETH), Zürich in 1990, both in electrical engineering. Since 1990 he has been working at the Laboratory for Electromagnetic Fields and Microwave Electronics (ETH) on nonlinear wave propagation, laser diode modeling (multi-section DFB and DBR lasers, VCSELs), computational electro-magnetics and on the design of non-periodic optical waveguide gratings e.g. by means of evolutionary algorithms. He got a Ph.D. degree in 1996 for the investigation of non-periodic waveguide gratings and non-periodic coupled cavity laser concepts. His current research interests includes highly multimode optical signal transmission in optical interconnects (i.e. in optical backplanes with extremely large waveguide cross sections) as well as alternative waveguiding concepts for dense integrated optical devices like e.g. photonic crystal devices, couplers and WDM filter structures. In 2001 he has been awarded the 2000 Outstanding Journal Paper Award by the Applied Computational Electromagnetics Society for a contribution on the application of evolutionary optimization algorithms in computational optics. Dr. Erni is the head of the Communication Photonics Group at ETH Zurich (www.photonics.ee.ethz.ch). He is also a member of the Swiss Physical Society (SPS), of the German Physical Society (DPG), of the Optical Society of America (OSA), and of the IEEE.

Thin Wire Representation of the Vertical Conductor in Surge Simulation

Md. Osman Goni, Eiji Kaneko, Hideomi Takahashi

Abstract— **Simulation of very fast surge phenomena in a three-dimensional (3-D) structure requires a method based on Maxwell's equations, such as the FDTD (finite difference time domain) method or the MoM (method of moments), because circuit-equation-based methods cannot handle the phenomena. This paper describes a method of thin wire representation of the vertical conductor system for the FDTD method which is suitable for the 3-D surge simulation. The thin wire representation is indispensable to simulate electromagnetic surges on wires or steel frames of which the radius is smaller than a discretized space step used in the FDTD simulation. A general surge analysis program named VSTL (Virtual Surge Test Lab.) based on the Maxwell equations formulated by the FDTD method is used to simulate the surge phenomena of a vertical conductor, including the effects of ground plane and without ground plane. By use of the Maxwell equations, VSTL is inherently able to take into account the three-dimensional geometrical features of a simulated structure unlike EMTP-type circuit-based transient programs. Comparisons between calculated results by the FDTD method, theoretical results and computed results by the NEC-2 (Numerical Electromagnetic Code) based on the MoM are presented to show the accuracy of the thin wire representation.**

Keywords— **FDTD method, Maxwell equations, thin wire, surge analysis, Numerical electromagnetic field analysis, vertical conductor.**

I. INTRODUCTION

CONVENTIONAL surge problems have successfully been solved by circuit theory, where transmission lines consisting of wires parallel to the earth surface are modeled by distributed-parameter circuit elements and the other components by lumped-parameter circuit elements [1]. The distributed-parameter circuit theory assumes plane-wave propagation that is a reasonable and accurate approximation for the transmission lines, and this assumption enables handling of the electromagnetic wave propagation within the circuit theory. On the other hand, very fast surge phenomena in a three-dimensional (3-D) structure, which includes surge propagation in a transmission tower and in a tall building, cannot be approximated by plane-wave propagation. Thus, those phenomena cannot be dealt with by circuit theory but need to be solved by Maxwell's equation as an electromagnetic field problem. Nowadays, the surge propagation in a transmission tower needs to be analyzed for economical insulation design. Furthermore, in a tall building, it is also important to assess the interference of lightning surges with information devices inside the building.

The processing speed and the memory capacity of computers have rapidly been progressing, and the FDTD (finite difference time domain) method that solves the Maxwell's equations by the method of difference becomes a practical choice in the field of antenna analysis [2], [3]. At present, even a personal computer can be used for FDTD analysis, and these circumstances caused the authors to analyze vertical conductor surge response based on the FDTD method.

This paper describes the surge analysis program named VSTL (Virtual Surge Test Lab.) based on the FDTD method. VSTL has been developed by Noda *et al.* from scratch at CRIEPI since late 1999. and continuous development is being carried out. VSTL is one of the registered programs of CRIEPI which are available to Japanese electric power utilities and to non-profitable research groups in the world. The FDTD method divides the space of interest into cubic cells and directly calculates the electric and magnetic fields of the cells by discretizing the Maxwell equations, where the derivatives with respect to time and space are replaced by a numerical difference. Updating the procedure at each time step gives the transient solution of electric and magnetic fields. By use of the FDTD method, the developed program VSTL is inherently able to take into account the geometrical features of a simulated structure, unlike EMTP-type circuit-based transient programs. Thus, the program is advantageous to solve both of the following problem types:

(i) surge propagation on a three-dimensional circuit (3-D skeleton structure);

(ii) surge propagation inside a three-dimensional imperfectly conducting medium such as earth soil.

The MoM (method of moments) also numerically solves the Maxwell Equations [4], and the NEC-2 (Numerical Electromagnetic Code)is a well-known program based on MoM [5]. Although MoM efficiently solves the type (i) problems, it cannot solve the type (ii) ones except very simple cases, because the handing of three-dimensional current distribution in a imperfectly conducting medium is complicated [6]. On the other hand, FDTD is inherently able to solve both problem types efficiently. One weak point of FDTD is the treatment of a thin wire. Thus, a field correction method to accurately treat the radius of the thin wire is proposed in [7] and implemented in VSTL. This paper proposes a method to accurately represent the thin wire for the single vertical conductor in the FDTD simulation ("thin wire" is defined as a conductive wire of which the radius is smaller than the size of a discretized cell). Then, surge simulation results using NEC-2 for the thin wire representation of a vertical conductor are also presented.

One of the authors derived the formula of surge

1054-4887 © 2004 ACES

impedance with a ground plane: $Z = 60\{ln(2\sqrt{2}h/r_0) - 1.983\}\,(\Omega)$ and without a ground plane: $Z = 60\{ln(2\sqrt{2}h/r_0) - 1.540\}\,(\Omega)$ [8]. The theoretical formula of surge impedance with the ground plane is very close to the well known experimental formula of Hara *et al.* [9]. The theoretical values of surge impedance at $t = 2h/c$ agree satisfactorily with the experimental and computed results using NEC-2 [10], [11]. Finally, this paper shows the comparisons between the theoretical results and simulation results of surge impedance with ground plane and without ground plane, based on the FDTD method and NEC-2.

II. **ALGORITHM**

In the analysis of VSTL, the analysis space is defined as a rectangular-parallelepiped space. Arbitrary number of thin wire conductors, rectangular-parallelepiped conductors, and localized voltage and current sources are arbitrarily placed in the analysis space, and transient electric and magnetic fields are calculated. The bottom of the analysis space can be defined as an imperfectly-conducting medium such as earth, and each boundary of the analysis space can independently be defined as a perfectly-conducting plane or an absorbing plane. The waveform of a localized voltage or current at an arbitrary position is outputted as specified.

A. ***FDTD Formulation***

There exist several different formulations of FDTD method. In order to precisely describe the proposed method of thin wire representation, the formulation used in this paper is briefly reviewed here. Assuming neither anisotropic nor dispersive medium in the space of interest, the Maxwell equations in Cartesian coordinates are

$$\nabla \times \boldsymbol{E} = -\mu \frac{\partial \boldsymbol{H}}{\partial t}, \qquad \nabla \times \boldsymbol{H} = \epsilon \frac{\partial \boldsymbol{E}}{\partial t} + \sigma \boldsymbol{E}, \qquad (1)$$

$$\nabla \cdot \boldsymbol{E} = \frac{\rho}{\epsilon}, \quad \text{and} \quad \nabla \cdot \boldsymbol{H} = 0. \qquad (2)$$

where

$\boldsymbol{E}$ electric field;
$\boldsymbol{H}$ magnetic field;
ρ charge density;
ϵ permittivity;
μ permeability;
σ conductivity.

Discretizing the analysis space by a small length Δs in all the directions, the space is filled with cubes of which the sides are Δs, and each cube is called a *cell*. Assume that the number of divisions of the analysis space along the x coordinate is N_x, along the y coordinate N_y, and along the z coordinate N_z. The analysis space is given by the following range,

$$x = i\Delta s, (0 \le i \le N_x), \quad y = j\Delta s, (0 \le j \le N_y),$$
$$z = k\Delta s, (0 \le k \le N_z). \qquad (3)$$

Equation (1) includes derivatives with respect to position x, y, z, and time t. In the FDTD formulation, representing values of electric and magnetic fields in a cell is shown in Fig. 1, and this yields the replacement of the derivatives with respect to x, y, and z in (1) with the following central difference,

$$\frac{\partial f(x)}{\partial x} \cong \frac{f(x + \Delta x/2) - f(x - \Delta x/2)}{\Delta s}. \qquad (4)$$

In the above equation, f is a component of $\boldsymbol{E}$ or $\boldsymbol{H}$, and the same equation is valid also for y and z. The same central difference shown in the following equation replaces the derivatives with respect to time in (1), assuming that electric fields are calculated at time steps $t = n\Delta t\,(n = 0, 1, \cdots)$ and magnetic fields at $t = (n + 1/2)\Delta t\,(n = 0, 1, \cdots)$ by turns,

$$\frac{\partial f(t)}{\partial t} \cong \frac{f(t + \Delta t/2) - f(t - \Delta t/2)}{\Delta t}. \qquad (5)$$

Applying (4) and (5) to (1) yields the following difference equations (e.g. $E^n{}_x(i + 1/2, j, k)$ represents x component electric field at position $x = (i + 1/2)\Delta s$, $y = j\Delta s$, $z = k\Delta s$, and at time $t = n\Delta t$, and the other components are expressed in the same manner),

$$\begin{aligned} E_x^n(i+\tfrac{1}{2},j,k) &= K_1 E_x^{n-1}(i+\tfrac{1}{2},j,k) \\ &+K_2\{H_z^{n-1/2}(i+\tfrac{1}{2},j+\tfrac{1}{2},k) - H_z^{n-1/2}(i+\tfrac{1}{2},j-\tfrac{1}{2},k) \\ &-H_y^{n-1/2}(i+\tfrac{1}{2},j,k+\tfrac{1}{2}) + H_y^{n-1/2}(i+\tfrac{1}{2},j,k-\tfrac{1}{2})\} \end{aligned} \qquad (6)$$

$$\begin{aligned} E_y^n(i,j+\tfrac{1}{2},k) &= K_1 E_y^{n-1}(i,j+\tfrac{1}{2},k) \\ &+K_2\{H_x^{n-1/2}(i,j+\tfrac{1}{2},k+\tfrac{1}{2}) - H_x^{n-1/2}(i,j+\tfrac{1}{2},k-\tfrac{1}{2}) \\ &-H_z^{n-1/2}(i+\tfrac{1}{2},j+\tfrac{1}{2},k) + H_z^{n-1/2}(i-\tfrac{1}{2},j+\tfrac{1}{2},k)\} \end{aligned} \qquad (7)$$

$$\begin{aligned} E_z^n(i,j,k+\tfrac{1}{2}) &= K_1 E_z^{n-1}(i,j,k+\tfrac{1}{2}) \\ &+K_2\{H_y^{n-1/2}(i+\tfrac{1}{2},j,k+\tfrac{1}{2}) - H_y^{n-1/2}(i-\tfrac{1}{2},j,k+\tfrac{1}{2}) \\ &-H_x^{n-1/2}(i,j+\tfrac{1}{2},k+\tfrac{1}{2}) + H_x^{n-1/2}(i,j-\tfrac{1}{2},k+\tfrac{1}{2})\} \end{aligned} \qquad (8)$$

$$\begin{aligned} H_x^{n+1/2}(i,j+\tfrac{1}{2},k+\tfrac{1}{2}) &= H_x^{n-1/2}(i,j+\tfrac{1}{2},k+\tfrac{1}{2}) \\ &+K_3\{-E_z^n(i,j+1,k+\tfrac{1}{2}) + E_z^n(i,j,k+\tfrac{1}{2}) \\ &+E_y^n(i,j+\tfrac{1}{2},k+1) - E_y^n(i,j+\tfrac{1}{2},k)\} \end{aligned} \qquad (9)$$

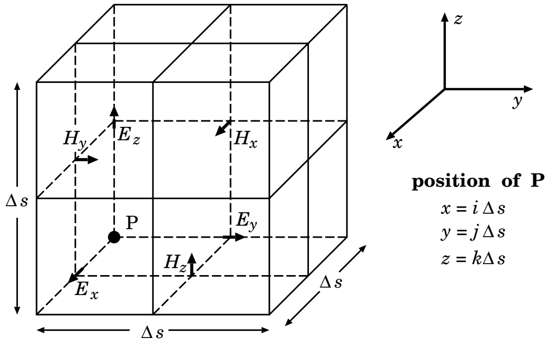

Fig. 1. Configuration of electric and magnetic fields in cell.

$$H_y^{n+1/2}(i+\frac{1}{2},j,k+\frac{1}{2}) = H_y^{n-1/2}(i+\frac{1}{2},j,k+\frac{1}{2}) \\ +K_3\{-E_x^n(i+\frac{1}{2},j,k+1)+E_x^n(i+\frac{1}{2},j,k) \\ +E_z^n(i+1,j,k+\frac{1}{2})-E_z^n(i,j,k+\frac{1}{2})\} \qquad (10)$$

$$H_z^{n+1/2}(i+\frac{1}{2},j+\frac{1}{2},k) = H_z^{n-1/2}(i+\frac{1}{2},j+\frac{1}{2},k) \\ +K_3\{-E_y^n(i+1,j+\frac{1}{2},k)+E_y^n(i,j+\frac{1}{2},k) \\ +E_x^n(i+\frac{1}{2},j+1,k)-E_x^n(i+\frac{1}{2},j,k)\}. \qquad (11)$$

In the derivation of the above equations, an approximation $\sigma\boldsymbol{E}^{n-1/2} \cong \sigma\{\boldsymbol{E}^{n-1}+\boldsymbol{E}^n\}/2$ is used, and coefficients K_1, K_2, and K_3 are given by the following equations,

$$K_1 = \frac{1-\frac{\sigma\Delta t}{2\epsilon}}{1+\frac{\sigma\Delta t}{2\epsilon}}, \quad K_2 = \frac{\Delta t}{\epsilon\Delta s}\frac{1}{1+\frac{\sigma\Delta t}{2\epsilon}}, \quad K_3 = \frac{\Delta t}{\mu\Delta s}. \quad (12)$$

Equations (6)–(11) are the FDTD formulas of the Maxwell equations, and transient fields are obtained by calculating electric and magnetic fields alternately at time intervals $\Delta t/2$. Although (2) is not explicitly formulated, it is proven that (6)–(11) automatically satisfies (2) [2]. The general surge analysis program VSTL uses this FDTD formulation.

B. *Time Step and Space Step*

Equations (6)–(11) are considered as numerical integration, and stable integration is performed if the following condition is satisfied (Courant's condition) [2],

$$\frac{\Delta t}{\sqrt{\mu\epsilon}} \le \frac{\Delta s}{\sqrt{3}}. \qquad (13)$$

On the other hand, the grid dispersion error is minimize when the above equation is an equality. Thus, the following formula is used in all calculations in this paper to determine time step Δt by user defined space step Δs:

$$\Delta t = \Delta s\sqrt{\frac{\mu\epsilon}{3}}(1-\alpha). \qquad (14)$$

α is a small positive value specified by the user in order to prevent instability of the numerical integration due to round-off error in (6)–(11).

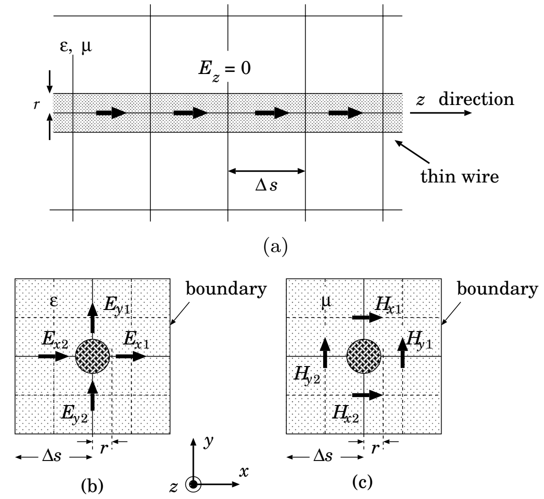

Fig. 2. Thin wire and configuration of adjacent electric and magnetic fields.

III. THIN WIRE REPRESENTATION

If the space step were chosen to be small enough to represent the shape of wire's cross section, an accurate representation would be possible. However, it requires impractical computational resources at this moment. The thin wire is defined as a conductive wire of which the radius is smaller than the size of a cell in the FDTD simulation. In antenna simulations, the thin wire is mainly used to represent an antenna element–the most important part. In surge simulations, it is also important to represent wires (phase and ground wires of a transmission/distribution line) and steel frames of a building along which surges propagate. Umashankar et al. proposed a method of thin wire representation by correcting the adjacent magnetic fields of the wire according to its radius [12], and [13] reports that the method is valid for the calculation of radiated fields by an antenna. However, the Umashankar method cannot give accurate surge impedance [14].

A. *Modification of Permittivity and Permeability*

The FDTD method of thin wire representation corrects both the adjacent electric and magnetic fields of the wire according to its radius and gives accurate surge impedance. The correction of the fields is carried out by equivalently modifying the permittivity and permeability of the adjacent cells. Fig. 2(a) shows a wire with ra-

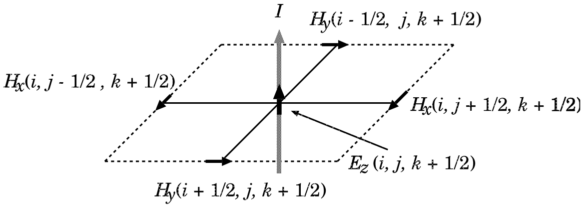

Fig. 3. Calculation of current by Ampere's Law.

dius r placed in the z direction, and the permittivity and permeability of the space are ϵ and μ. Fig. 2(b) shows the cross section of the wire with the adjacent electric fields, and Fig. 2(c) with the adjacent magnetic fields. In the FDTD method, a wire is, in principle, represented by forcing the electric fields along the center line of the wire to be zero, and E_z components are forced to be zero in this case. In order to take into account the effect of the thin wire radius r, the VSTL uses the following corrected permittivity to calculate the adjacent electric fields $E_{x1}, E_{x2}, E_{y1}, E_{y2}$ in (6)–(8),

$$\epsilon' = m\epsilon,$$

and the following corrected permeability to calculate the adjacent magnetic fields $H_{x1}, H_{x2}, H_{y1}, H_{y2}$ in (9)–(11),

$$\mu' = \mu/m,$$

where the correction factor m is given by

$$m = \frac{1.471}{\ln(\Delta s/r)}. \tag{15}$$

IV. GENERAL SURGE ANALYSIS PROGRAM

The general surge analysis program, named Virtual Surge Test Lab. (VSTL), which is based on the FDTD method and the proposed thin wire representation for the vertical conductor is briefly described in this section.

A. *Treatment of Boundaries*

Each boundary of the space of interest can independently be defined as a perfectly conducting plane or an absorbing plane. The perfectly conducting plane can easily be represented by forcing the tangential components of electric fields at the boundary to be zero. The second-order Liao's method is used to represent the absorbing plane, because it is more accurate and required less memory compared with other methods [15]. An open space can be assumed by applying the absorbing plane to all the boundaries of the space of interest.

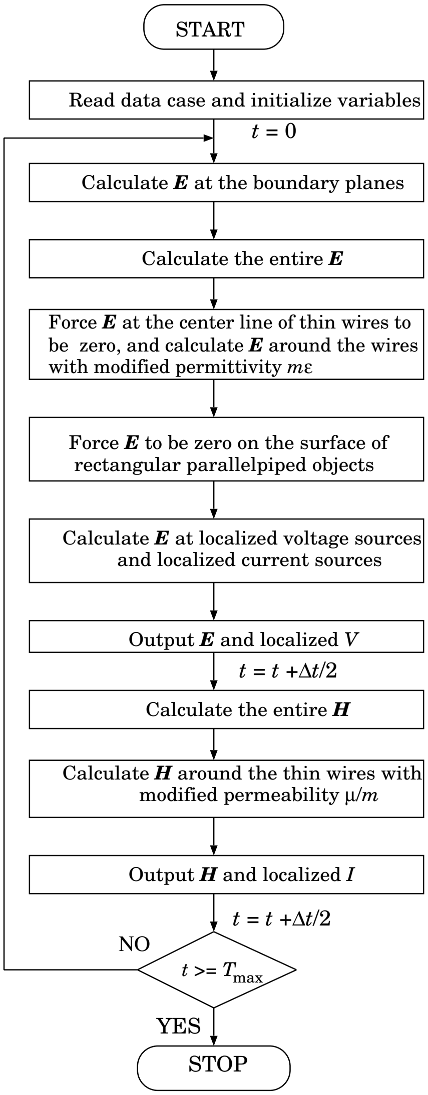

Fig. 4. Calculation procedure of VSTL.

B. *Imperfectly Conducting Earth*

The goal of the surge analysis is usually to find the solution of surge propagation in a 3-D skeleton structure above either an imperfectly or perfectly conducting earth. In the FDTD calculation, the representation of the conducting earth with resistivity ρ_e can be achieved by simply setting the value of σ in (12) to $1/\rho_e$ in the region defined as the copper plane.

C. *Rectangular-Parallelepiped Conductors*

The geometrical shape of most power equipment can be represented by a combination of several rectangular-parallelepiped objects. The rectangular-parallelepiped conductor is simply modeled by forcing the tangential electric fields on its surface to be zero.

D. *Localized Voltage and Current Sources*

Unlike the static electric fields, the transient electric fields do not satisfy $\nabla \times \boldsymbol{E} = 0$. Thus, in the analysis of transient fields, the voltage or the voltage difference does not make sense in general. But if we take notice of an electric field component of a cell, the voltage difference across a side of the cell can reasonably be defined as $V = E\Delta s$, because waves of which the wavelength is shorter than $\lambda = 2\Delta s$ do not propagate in the FDTD calculation due to the bandwidth limitation of Δs. Therefore, we can model a localized voltage source by forcing an electric field component at a specified position in a specified direction to be a specified waveform. For example, in order to place a voltage source of which the waveform is given by $V^n = V(n\Delta t)$ at $x = i\Delta s$, $y = j\Delta s$, $z = (k+1/2)\Delta s$ in the z direction, the following equation is used to force the electric field value,

$$E_z^n(i, j, k+1/2) = -\{V^n - RI^{n-1/2}\}/\Delta s, \qquad (16)$$

where R is the internal resistance of the voltage source specified by a user (it can be set to zero), and current I is given by the following equation as shown in Fig. 3,

$$\begin{aligned} I^{n-1/2} = \{ & H_x^{n-1/2}(i, j-\frac{1}{2}, k+\frac{1}{2}) \\ & -H_x^{n-1/2}(i, j+\frac{1}{2}, k+\frac{1}{2}) \\ & +H_y^{n-1/2}(i+\frac{1}{2}, j, k+\frac{1}{2}) \\ & -H_y^{n-1/2}(i-\frac{1}{2}, j, k+\frac{1}{2})\}\Delta s. \qquad (17) \end{aligned}$$

In the case of a current source, because current itself is a general quantity even in the transient fields, it can be modeled by modifying an electric field component at a specified position in a specified direction as in the following example. In order to place a current source of which the waveform is given by $I^n = I(n\Delta t)$ at $x = i\Delta s$, $y = j\Delta s$, $z = (k+1/2)\Delta s$ in the z direction, the following term is added to (8),

$$-\frac{\Delta t/\epsilon}{1+\frac{\sigma\Delta t}{2\epsilon}}\frac{I^{n-1/2}}{\Delta s^2}, \qquad \sigma = 1/(R\Delta s), \qquad (18)$$

and R is the internal resistance of the current source specified by a user.

E. *Calculation Procedure and Output*

The flow chart of the calculation procedure of VSTL is shown in Fig. 4. The output of VSTL includes the waveform of localized voltage differences and current intensities at a specified position in a specified direction. The waveform of the localized voltage difference is calculated by $V = E\Delta s$, and that of the current intensity by (17).

V. SIMULATION RESULTS OF VERTICAL CONDUCTOR

A. *With Ground Plane*

The modeling of a vertical conductor system is quite important as a basis of transmission tower modeling. A tower is approximated as a vertical cylinder having a height equal to that of the tower and a radius equal to the mean equivalent radius of the tower [16]. Fig. 5 shows a reduced-scale model of the vertical conductor system with a single cylindrical conductor of radius 5 mm. The vertical conductor is excited by a pulse generator (PG) via a current lead wire, and the tower-top voltage is defined as the voltage between the tower top and a voltage measuring wire. In the simulation with FDTD, the dimensions of the analysis space were $3.5\,\mathrm{m} \times 2.5\,\mathrm{m} \times 1.0\,\mathrm{m}$ with space step $\Delta s = 2\,\mathrm{cm}$. The time step was determined by (14) with $\alpha = 0.01$, and all the six boundaries of the cell were treated as second-order Liao's absorbing boundary. The thickness and the resistivity of the earth were set to 6 cm and $1.69 \times 10^{-8}\,\Omega\mathrm{m}$. The PG was mod-

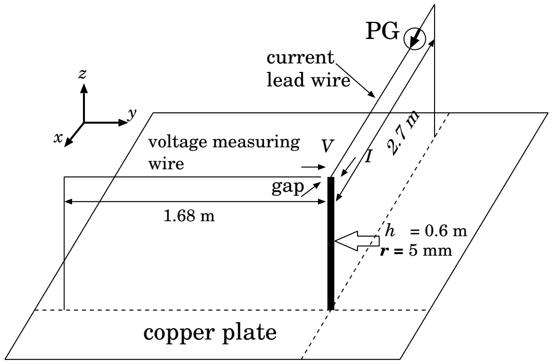

Fig. 5. Arrangement of the vertical conductor system (with ground plane).

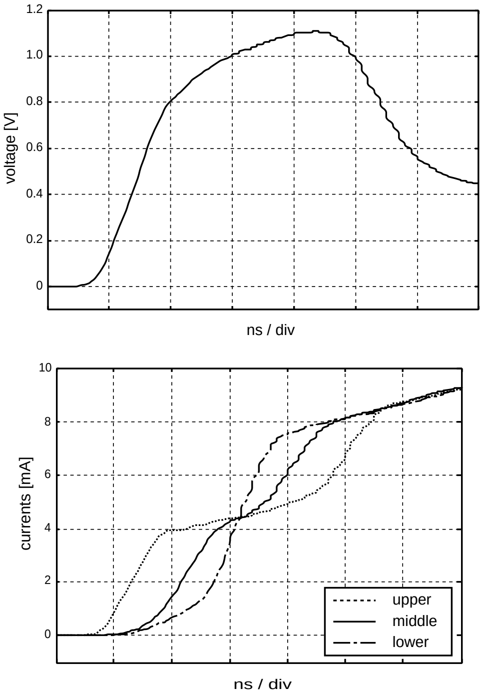

Fig. 6. Calculated waveforms of the voltage and currents (with ground plane).

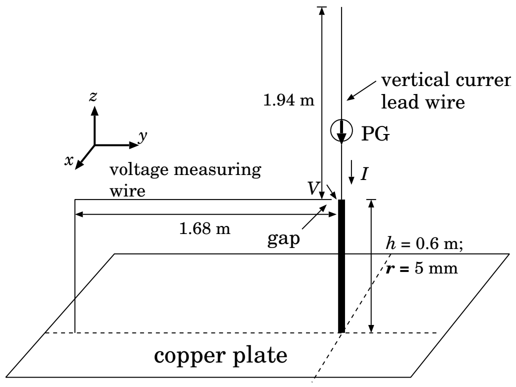

Fig. 7. Arrangement of the vertical conductor system (without ground plane).

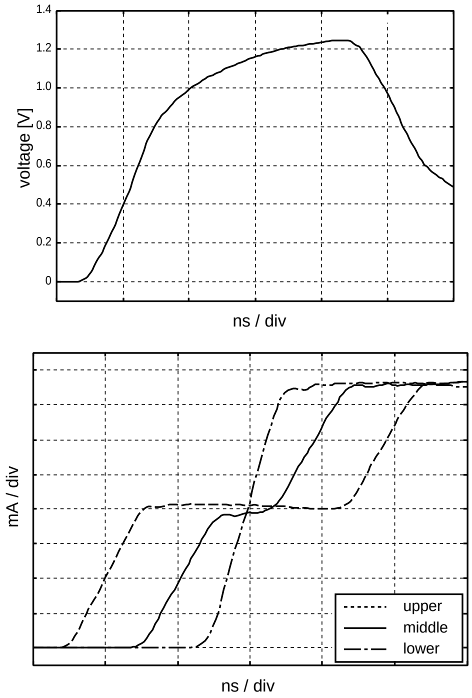

Fig. 8. Arrangement of the vertical conductor system (without ground plane).

eled by a current source, with internal resistance 0.5 kΩ. Fig. 6 shows the calculated results of voltage waveforms at the top of the vertical conductor and that of current waveforms in the different parts of it. The influence of the ground plane can be observed by realizing a small current which is induced in the vertical conductor before the actual surge current flows through it. This small magnitude of current is due to the fact that the electric field produced by the current injected in the horizontal current lead wire induces this current at the vertical conductor. The reflection phenomena of the current wave from the ground can be understood with these results.

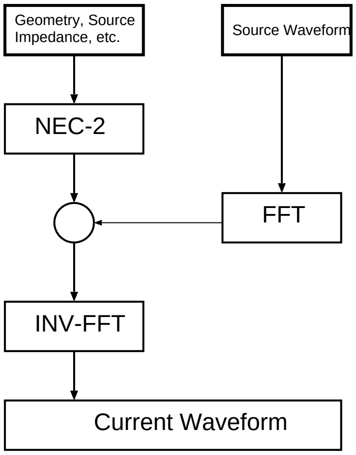

Fig. 9. Flow of the solution using NEC-2.

B. Without Ground Plane

A reduced-scale model of the vertical conductor system without ground plane is shown in Fig. 7. It is also the case of the lightning phenomena caused by the return stroke [17]. The pulse generator, in this case, is placed at the top of the vertical conductor and the current lead wire is extended vertically without connecting to the ground. The dimensions of the analysis space were $1.0\,\mathrm{m} \times 2.5\,\mathrm{m} \times 3.0\,\mathrm{m}$. All other parameters are the same as the case with the ground plane. Fig. 8 shows the waveform of conductor-top voltage and currents splitting into the vertical conductor.

C. Computation Time

It may be believed that the FDTD method is a time-consuming method. However, the progress of computers in terms of speed and memory is considerable, and even a personal computer can be used for FDTD calculations. In fact, the simulations presented in this paper were performed by a personal computer with Intel Celeron 700 MHz CPU and 192 MB RAM. Although the computation time absolutely depends on the cell size and the dimension of the analysis space, in this paper, the cell size is considered a lower value satisfying the Courant condition in order to obtain more accurate results of the surge response. Therefore, the computation time for the vertical conductor with ground plane is around 16 minutes and without ground plane is around 12 minutes.

VI. SURGE SIMULATION BY NEC-2

In this section, the NEC-2 (Numerical Electromagnetic Code) is employed for the analysis of surge response of the vertical conductor. It is a widely used three-dimensional electromagnetic modeling code based on the MoM (method of moments) [4] in the frequency domain, and is particularly effective in analyzing the electromagnetic response of antennas or other metallic structures

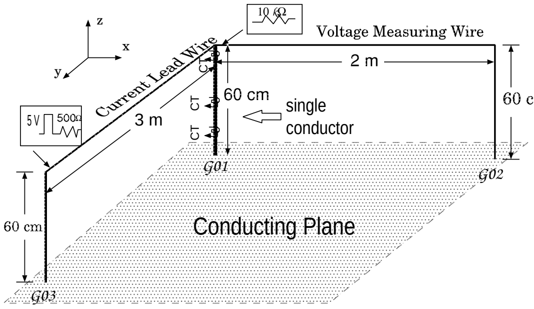

Fig. 10. Arrangement of the vertical conductor system (with ground plane).

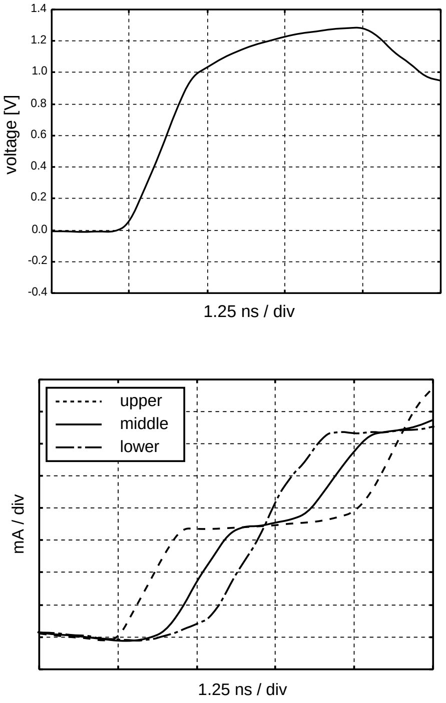

Fig. 11. Computed waveforms of voltage at the top and currents in the various parts of the vertical conductor in case with ground surface.

composed of thin wires. A vertical conductor system needs to be decomposed into thin wire elements, and the position, orientation and the radius of each element constitute the input data, along with the description of the source and frequencies to be analyzed. In the analysis, all the elements in the system are treated as perfect conductors. To solve the time-varying electromagnetic response, Fourier transform and inverse Fourier transform are used. The MoM requires that the entire structure be divided into wire segments that must be small compared to the wavelength. Once the model is defined, an excitation is imposed as a voltage source or a plane wave on one of the wire segments. The MoM approach is to determine the current on every segment due to the source and all the other currents by numerically solving the electric field integral equation. Fig. 9 shows the flow chart of the solution by NEC-2.

Fig. 10 shows the reduced-scale model of the vertical conductor system for the surge analysis using NEC-2. The arrangement of the current lead wire connected to the top of the vertical conductor with the existence of the ground plane is indicated in Fig. 10. The dimensions of the vertical conductor model are maintained the same as with the FDTD method in the previous section. A step current pulse generator having pulse voltage of 5 V in magnitude, rise-time of 1 ns and pulse width of 40 ns is used, which is meant to incorporate the influence of the induction from the lightning channel hitting the vertical conductor.

For the numerical analysis, the conductors of the system are divided into 5 cm segments. This segmentation must satisfy electrical consideration relative to the wavelength as: $0.001\lambda < \Delta L < 0.1\lambda$, where ΔL and λ are the segment length and wavelength respectively. The internal impedance of the pulse generator is 0.5 kΩ. The system of structures under analysis was postulated to be on perfectly conducting ground. Then we calculate the surge impedance, which is defined by the ratio of the instantaneous values of the voltage to the current at the moment of voltage peak.

A. *With Ground Plane*

Fig. 11 shows the simulation results by NEC-2. The influence of the reflected wave from the ground reaches the top of the conductor is observed at $t = 2h/c = 4$ ns exactly, which means that the travelling wave is propagating at the velocity of light. The computed waveforms of currents which are flowing through the vertical conductor are indicated by the mark 'CT' in Fig. 10. As the pulse generator is placed 300 cm from the vertical conductor, the current through the vertical conductor is delayed approximately 10 ns. The existence of the ground plane can also be observed in these current waveforms, where the field produced by the current injected horizontally induces currents of small magnitude before the actual surge current flows through the vertical conductor. These simulation results of currents and voltage waveforms in Fig. 11 obtained by NEC-2 are almost identical to the simulation results with the FDTD method in Fig. 6.

B. *Without Ground Plane*

A reduced-scale model of the vertical conductor system without a ground plane is indicated in Fig. 12. Here, the current lead wire is extended vertically to the top of the vertical conductor. The same PG is now used at the top without connecting to the ground. In both cases, the voltage measuring wire is stretched horizontally and connected to the ground. This termination condition does not affect the electromagnetic phenomena at the vertical conductor within 17.33 ns. All other parameters are maintained the same as the ground plane

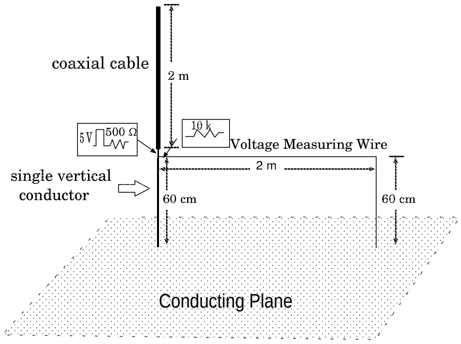

Fig. 12. Arrangement of the vertical conductor system (without ground plane).

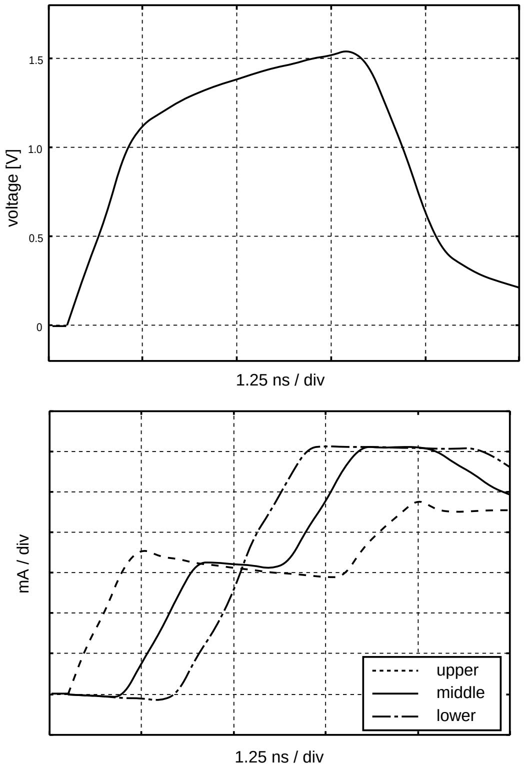

Fig. 13. Computed waveforms of voltage at the top and currents in the various parts of the vertical conductor in case with no ground surface.

case. The simulation results of voltage at the top of the vertical conductor and currents through different parts of it are shown in Fig. 13. However, in this analysis, the waveforms of current through the vertical conductor are somewhat different from the current waveforms of Fig. 11 at the starting region because of absence of the ground surface. Also, the current starts flowing instantly through the vertical conductor without being delayed.

C. *Computation Time*

Computation is carried out in the frequency range of 7.813 MHz to 4 GHz with an increment step of 7.813 MHz. This corresponds to the time range of 0 to 128 ns with 0.25 ns increments. The computation time for the output of NEC-2 block of the flow chart of Fig. 10, with a Intel Celeron 700 MHz processor with 192 MB RAM is about 56 seconds for the ground plane case and 30 seconds without ground plane case.

VII. THEORETICAL FORMULA OF SURGE IMPEDANCES

One of the author's theory is able to apply widely in case of ground surface and without ground surface. Suppose that a surge electric current is injected on the vertical conductor whose height is h and radius is r_0. Then the surge current wave is reflected at the ground of the perfect conductor and returns to the top of the vertical conductor.

Introducing the electric current reflectivity $\beta = 1$ and the magnetic field reflectivity $\gamma(\gamma_i, \gamma_r) = 0$, the theoretical formula of surge impedance which is very close to the well known experimental formula [9] is obtained as follows;

$$\begin{aligned} Z &= 60(\ln(\frac{h}{2r_0}) - \frac{1}{4}) \\ &= 60(\ln(\frac{2\sqrt{2}h}{r_0}) - 1.983). \end{aligned} \tag{19}$$

Equation (19) gives the surge impedance of the vertical conductor just after the occurrence of the reflection of the travelling wave propagating down from the top of the structure. However, if it is considered that $\beta = \gamma_i = \gamma_r = 1$, it became

$$V(t) = \frac{c\mu_0 I_0}{2\pi}\left(\ln\frac{(ct + 2r_0)}{2r_0} - \frac{ct}{2(ct + r_0)}\right).$$

The above equation can be modified by substituting $ct = 2h$, where c is the velocity of light and assuming $h \gg r_0$ as follows;

$$\begin{aligned} Z &= 60(\ln(\frac{h}{r_0}) - \frac{1}{2}) \\ &= 60(\ln(\frac{2\sqrt{2}h}{r_0}) - 1.540). \end{aligned} \tag{20}$$

On the other hand, if there is no ground, the following formula is used [18],

$$\begin{aligned} V(t) &= \int_0^{ct} (-E_i \cdot dl) \\ &= \frac{c\mu_0 I_0}{2\pi}\left(\ln\frac{(ct + 2r_0)}{2r_0} - \frac{ct}{2(ct + r_0)}\right). \end{aligned}$$

Substituting $ct = 2h$ and assuming $h \gg r_0$ in the above equation, we get

$$Z = 60(\ln(\frac{h}{r_0}) - \frac{1}{2})$$

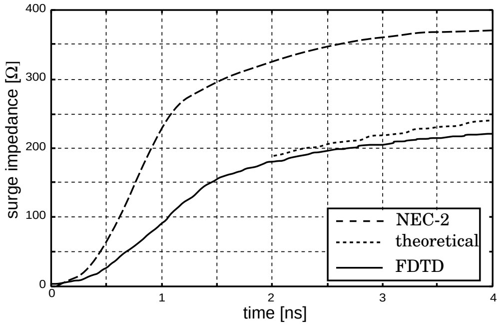

(a) With ground plane.

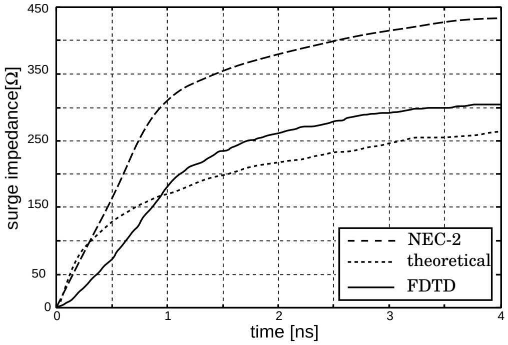

(b) Without ground plane.

Fig. 14. Surge impedance of the single vertical conductor at $0 < t \leq 2h/c$.

$$= 60(\ln(\frac{2\sqrt{2}h}{r_0}) - 1.540). \qquad (21)$$

This formula given by (21) is the same as (20). The waveforms of the surge impedances calculated from the theoretical Equations (19) and (20) with ground and without ground plane respectively, are plotted along with the simulation results by the FDTD method and the MoM in Fig. 14. However, the surge impedance values at $t \approx 2h/c$ are summarized in Table I.

TABLE I
SURGE IMPEDANCES OF THE VERTICAL CONDUCTOR AT $t \approx 2h/c$

	With ground	Without ground
NEC-2	365	434
Theoretical	232	258
FDTD	214	304

VIII. **CONCLUSIONS**

In this paper, a method of thin wire representation of a vertical conductor system with the effect of ground plane and without ground plane is described. The analysis of surge response has been carried out by the FDTD-based surge simulation code VSTL and MoM-based NEC-2. The accuracy of VSTL has been validated by comparing with NEC-2 results and theoretical values of the vertical conductor surge impedance. The bottom of the analysis space in both cases is considered as a copper plate, although in NEC-2, it was postulated to be on perfectly conducting ground. The analysis results of the surge response with the FDTD method and NEC-2 are found to be quite similar. The computation time absolutely depends on the configuration of the system structures and modeling of the wires.

Acknowledgment: The authors are very much grateful to Dr. T. Noda and S. Yokoyama for their valuable support of utilizing VSTL software for the FDTD calculation and their research contributions.

REFERENCES

[1] H. W. Dommel, "Digital computer solution of electromagnetic transients in single-and multi-phase networks," *IEEE Trans. Power App. Syst.* , vol. PAS-88, pp. 388–399, Apr.1969.

[2] K. S. Yee, "Numerical solution of initial boundary value problems involving Maxwell's equations in isotropic media," *IEEE Trans. Antennas Propagat.* , vol. AP-14, pp. 302–307, May 1966.

[3] K. S. Kunz and R. J. Luebbers, *The Finite Difference Time Domain Method for Electromagnetics*, Boca Raton, FL: CRC, 1993.

[4] R. F. Harrington, *Field Computation by Moment Methods.* New York: Macmillan, 1968.

[5] G. J. Burke and A. J. Poggio, *Numerical Electromagnetic Code (NEC)– Method of Moments*: Lawrence Livermore Laboratory, 1981.

[6] G. J. Burke and E. K. Miller, "Modeling antennas near to and penetrating a lossy interface," *IEEE Trans. Antennas Propagat.*, vol. AP-32, pp. 1040–1049, Oct. 1984.

[7] T. Noda and S. Yokoyama, "Development of a general surge analysis program based on the FDTD method," *Trans. IEE of Japan* vol. 121-B, no. 5, pp. 625–632, 2001.

[8] H. Takahashi, "A Consideration on the vertical conductor problem," *Proc. of ICEE*, pp. 635–638, 2001.

[9] T. Hara et al., "Transmission tower model for surge analysis," in *Proc. H3 IEE Japan Power and Energy Conf.*, 1991, Paper no. II-270.

[10] M. O. Goni, P. T. Cheng and H. Takahashi, "Theoretical and experimental investigations of the surge response of a vertical conductor," in *Proc. IEEE Power Engineering Soceity Int'n Conf.*, vol. 2, pp. 699–704, 2002.

[11] M. O. Goni, and H. Takahashi, "Theoretical and experimental investigations of the surge response of a vertical conductor," *The ACES Journal*, vol. 18, no. 1 pp. 41–47, Mar. 2003.

[12] K. R. Umashankar et al., "Calculation and experimental validation of induced currents on coupled wires in an arbitrary shaped cavity," *IEEE Trans. Antennas Propagat.*, vol. AP-35, pp. 1248–1248, Nov. 1987.

[13] T. Kashiwa, S. Tanaka, and I. Fukai, "Time domain analysis of Yagi-Uda antennas using the FDTD method," *IEICE Trans. Commun.* vol. J76-BII, pp 872-872, Nov. 1993.

[14] T. Noda and S. Yokoyama, "Thin wire representation in finite difference time domain surge simulation," *IEEE Trans. Power Delivery* vol. 17, no. 3, pp. 840–847, 2002.

[15] Z. P. Liao, H. L. Wong, B.-P. Yang, and Y.-F. Yuan, "A transmitting boundary for transient wave analysis," *Science sinica, Series A,* vol. 27, no. 10 pp. 1063–1063, 1984.

[16] C. A. Jordan, "Lightning computation for transmission line with ground wires," *General Electric Review,* vol. 34, pp. 180–185, 1934.

[17] Y. Baba and M. Ishii, "Numerical electromagnetic field analysis on lightning surge response of tower with shield wire," *IEEE Trans. PWRD,* vol. 15, pp. 1010–1015, no. 3, Jul. 2000.

[18] H. Takahashi, E. Kaneko, K. Yokokura, K. Nojima, T. Shiori, and I. Ohshima, "New Derivation method of the surge impedance on the tower model of a vertical conductor by the electromagnetic field theory (Part 3: Introduction of confined gauge potential and experimental analysis) "(in japanese), *Proc. of IEE of Japan*, vol. 1, pp. 229–234, 1995.

Md. Osman Goni was born in Bangladesh on February, 1971. He received his B.S. degree in electrical and electronic engineering from Bangladesh Institute of Technology, Khulna in 1993. He joined the Institute in 1994. He received M.S. degree from the University of the Ryukyus, Japan in 2001. He is currently a Ph.D. student at the University of the Ryukyus, Japan. His research interests includes electromagnetic theory, the FDTD method, MoM, NEC-2, surge analysis, vertical conductor problems, EMTP etc. He is also a student member of the IEEE, IEE of Japan and AGU.

Eiji Kaneko was born in Japan, on September 16, 1952. He received M.S. degree from Nagoya Univesity in 1977. He joined in Toshiba Corporation in April 1977 and engaged in research and development of vacuum interrupter and discharge. He received D.Eng. degree from Nagoya Univesity in 1989. He is now an associate professor of University of the Ryukyus. He has been engaged in teaching and research on electric power and energy system engineering, electromagnetic energy engineering etc. Dr. Kaneko is a member of IEEE and IEE of Japan.

Hideomi Takahashi was born in Tokyo, Japan, on November 13, 1940. He received B.S. degree from Tokyo Institute of Technology in 1963, and M.S. degree from the University of Tokyo in 1965. He joined in Toshiba Corporation and engaged in the research and development on high voltage engineering, especially vacuum interrupter and ozonizer etc. He received D.Eng. degree from the University of Tokyo in 1986. He is a professor of University of the Ryukyus. He has been engaged in teaching and research on power system engineering. Dr. Takahashi is a senior member of the IEEE and IEE of Japan.

2004 INSTITUTIONAL MEMBERS

AUSTRALIAN DEFENCE LIBRARY
Northcott Drive
Campbell, A.C.T. 2600 AUSTRALIA

BAE SOWERBY RESEARCH CTR.
FPC 267 Po Box 5
Filton, Bristol, BS134 7QW
UNITED KINGDOM

BAE SYSTEMS
W423A, Warton Aerodrome
Preston, PR41AY
UNITED KINGDOM

BAE SYSTEMS, ADV. TECH. CTR
W. Hanningfield Rd, Tech Centre Lib.
Gt. Baddow, Chelms., CM2 8HN UK

BEIJING BOOK COMPANY, INC
701 E Lindon Ave.
Linden, NJ 07036-2495

BIBLIO. FACOLTA' INGEGNERIA
Lib: Dott. Gaetana Bocc. Fiandra
Via G Duranti
Perugia, ITALY 89-06125

CULHAM EM
Bldg F5, Culham
Abingdon, Oxford, OX14 3ED UK

DARTMOUTH COLL-FELDBERG LIB
6193 Murdough Center
Hanover, NH 03755-3560

DEFENCE RESEARCH ESTAB. LIB.
3701 Carling Avenue
Ottowa, ON, K1A 0Z4 CANADA

DTIC-OCP/IBRARY
8725 John J. Kingman Rd. Ste 0944
Ft. Belvoir, VA 22060-6218

EDINBURGH DSTO
PO Box 830673
Birmingham, AL 35283-0673

ELEC. COMM. LAB LIBRARY
Hikarinooka Yokosuka Shi
Kanagawa-Ken
239-0847 MZ JAPAN

EM SOFTWARE & SYSTEMS
PO Box 1354
Stellenbosch, S. AFRICA 7599

ENGINEERING INFORMATION, INC
PO Box 543
Amsterdam, Netherlands 1000 Am

ERA TECHNOLOGY, LTD
Cleeve Rd
Leatherhead, Surrey, UK OX5 1JE

ETSE TELECOMUNICACION
Biblioteca, Campus Lagoas
Vigo, 36200 SPAIN

FANFIELD LTD
Braxted Park
Witham, Essex, CM8 3XB UK

FLORIDA INTERNATIONAL U.
10555 W. Flagler St.
ECE Dept., EAS-3983
Miami, FL 33174

GEORGIA TECH LIBRARY
225 North Avenue, NW
Atlanta, GA 30332-0001

HANGANG UNIVERSITY / IS LIB.
17 Haengdang-Dong, Seongdong KU
Seoul, S KOREA 133-791

HELSINKI UNIV. OF TECHNOLOGY
Otakaari 5-A
PO Box 3000
Espoo, FINLAND 02015 HUT

HEWLETT PACKARD
14012 NE 47TH Avenue
Vancouver, WA 89686

HRL LABS, RESEARCH LIBRARY
3011 Malibu Canyon
Malibu, CA 90265

IEE INSPEC
Acquisitions Section
Michael Faraday House
6 Hills Way
Stevenage, Herts UK SG1 2AY

IIT RESEARCH INSTITUTE
185 Admiral Cochrane Drive
Annapolis, MD 21401-7396

IND CANTABRIA
PO Box 830470
Birmingham, AL 35283

INSTITUTE FOR SCIENTIFIC INFO.
Publication Processing Dept.
3501 Market St.
Philadelphia, PA 19104-3302

INSYS LTD.
Reddings Wood, Ampthill
Bedford, MK45 2HD UK

IPS RADIO & SPACE SVC/LIBRARY
PO Box 5606
W. Chatswood, 2057 AUSTRALIA

LIBRARY of CONGRESS
Reg. Of Copyrights
Attn: 40T Deposits
Washington DC, 20559

LINDA HALL LIBRARY
5109 Cherry Street
Kansas City, MO 64110-2498

MAAS
16 Peachfield Road
Great Malvern, Worc.
WR 14 4AP UNITED KINGDOM

MISSISSIPPI STATE UNIV LIBRARY
PO Box 9570
Mississippi State, MS 39762

MIT LINCOLN LABORATORY
Periodicals Library
244 Wood Street
Lexington, MA 02420

NA KANSAI KINOKUNNA CO.
Attn: M. MIYOSHI
PO Box 36 (NDLA KANSAI)
Hongo, Tokyo, JAPAN 113-8688

NATIONAL INSTITUTE OF AIST
AIST Tsukuba Central 2-1-1-1
Umezono
Tsukuba-Shi, Ibariki
305-8568 JAPAN

NATL RADIOLOGICAL PROT. BD.
Chilton, Didcot, OXON,
OX11 0RG UK

NAVAL POSTGRADUATE SCHOOL
Attn: J. Rozdal
411 Dyer Rd./ Rm 111
Monterey, CA 93943-5101

NAVAL RESEARCH LABORATORY
C. Office, 4555 Overlook Avenue, SW
Washington, DC 20375

OVIEDO LIBRARY
LRC 04440
PO Box 830679
Birmingham, AL 35283

PENN STATE UNIVERSITY
126 Paterno Library
University Park, PA 16802-1808

PHILIPS RESEARCH LAB LIBRARY
Cross Oak Lane, Salfords
Redhill, RH1 5HA SURREY UK

QUEEN MARY & WESTFIELD
COLLEGE
Mile End Rd.
London E1 4NS UK

RENTON TECH LIBRARY/BOEING
PO BOX 3707
SEATTLE, WA 98124-2207

SOUTHWEST RESEARCH INST.
6220 Culebra Road
San Antonio, TX 78238

SWETS BLACKWELL
440 Creamery Way, Suite A
Exton, PA 19341

TAMKANG UNIVERSITY
PO Box 380470
Birmingham, AL 35283

TECHNISCHE UNIV. DELFT
Mekelweg 4, Delft, Holland, 2628 CD
NETHERLANDS

TIB & UNIV. BIB. HANNOVER
DE/5100/G1/0001
Welfengarten 1B
Hannover, GERMANY 30167

TOKYO KOKA UNIV
1404-1 Katakura-Cho
Hachioji, Tokyo, JAPAN 192-0914

UNIV OF CENTRAL FLORIDA LIB.
PO Box 162666
Orlando, FL 32816-2440

UNIV OF COLORADO LIBRARY
Campus Box 184
Boulder, CO 80309-0184

UNIVERSITY OF MISSISSIPPI
John Davis Williams Library
PO Box 1848
University, MS 38677-1848

UNIV OF MISSOURI-ROLLA LIB.
1870 Miner Circle
Rolla, MO 65409-0001

USAE ENG. RES. & DEV. CENTER
Attn: Library/Journals
72 Lyme Road
Hanover, NH 03755-1290

RUBENS VALERIO
2129 Flatbush Ave., #4000
Brooklyn, NY 11234-4336

VECTOR FIELDS, LTD
24 Bankside
Kidlington, Oxford OX51JE

ACES COPYRIGHT FORM

This form is intended for original, previously unpublished manuscripts submitted to ACES periodicals and conference publications. The signed form, appropriately completed, MUST ACCOMPANY any paper in order to be published by ACES. PLEASE READ REVERSE SIDE OF THIS FORM FOR FURTHER DETAILS.

TITLE OF PAPER:

AUTHORS(S)

PUBLICATION TITLE/DATE:

RETURN FORM TO:
Dr. Atef Z. Elsherbeni
University of Mississippi
Dept. of Electrical Engineering
Anderson Hall Box 13
University, MS 38677 USA

PART A - COPYRIGHT TRANSFER FORM

(NOTE: Company or other forms may not be substituted for this form. U.S. Government employees whose work is not subject to copyright may so certify by signing Part B below. Authors whose work is subject to Crown Copyright may sign Part C overleaf).

The undersigned, desiring to publish the above paper in a publication of ACES, hereby transfer their copyrights in the above paper to The Applied Computational Electromagnetics Society (ACES). The undersigned hereby represents and warrants that the paper is original and that he/she is the author of the paper or otherwise has the power and authority to make and execute this assignment.

Returned Rights: In return for these rights, ACES hereby grants to the above authors, and the employers for whom the work was performed, royalty-free permission to:

1. Retain all proprietary rights other than copyright, such as patent rights.
2. Reuse all or portions of the above paper in other works.
3. Reproduce, or have reproduced, the above paper for the author's personal use or for internal company use provided that (a) the source and ACES copyright are indicated, (b) the copies are not used in a way that implies ACES endorsement of a product or service of an employer, and (c) the copies per se are not offered for sale.
4. Make limited distribution of all or portions of the above paper prior to publication.
5. In the case of work performed under U.S. Government contract, ACES grants the U.S. Government royalty-free permission to reproduce all or portions of the above paper, and to authorize others to do so, for U.S. Government purposes only.

ACES Obligations: In exercising its rights under copyright, ACES will make all reasonable efforts to act in the interests of the authors and employers as well as in its own interest. In particular, ACES REQUIRES that:

1. The consent of the first-named author be sought as a condition in granting re-publication permission to others.
2. The consent of the undersigned employer be obtained as a condition in granting permission to others to reuse all or portions of the paper for promotion or marketing purposes.

In the event the above paper is not accepted and published by ACES or is withdrawn by the author(s) before acceptance by ACES, this agreement becomes null and void.

AUTHORIZED SIGNATURE	TITLE (IF NOT AUTHOR)
EMPLOYER FOR WHOM WORK WAS PERFORMED	DATE FORM SIGNED

Part B - U.S. GOVERNMENT EMPLOYEE CERTIFICATION

(NOTE: if your work was performed under Government contract but you are not a Government employee, sign transfer form above and see item 5 under Returned Rights).

This certifies that all authors of the above paper are employees of the U.S. Government and performed this work as part of their employment and that the paper is therefor not subject to U.S. copyright protection.

AUTHORIZED SIGNATURE	TITLE (IF NOT AUTHOR)
NAME OF GOVERNMENT ORGANIZATION	DATE FORM SIGNED

PART C - CROWN COPYRIGHT

(NOTE: ACES recognizes and will honor Crown Copyright as it does U.S. Copyright. It is understood that, in asserting Crown Copyright, ACES in no way diminishes its rights as publisher. Sign only if *ALL* authors are subject to Crown Copyright).

This certifies that all authors of the above Paper are subject to Crown Copyright. (Appropriate documentation and instructions regarding form of Crown Copyright notice may be attached).

AUTHORIZED SIGNATURE	TITLE OF SIGNEE
NAME OF GOVERNMENT BRANCH	DATE FORM SIGNED

Information to Authors

ACES POLICY

ACES distributes its technical publications throughout the world, and it may be necessary to translate and abstract its publications, and articles contained therein, for inclusion in various compendiums and similar publications, etc. When an article is submitted for publication by ACES, acceptance of the article implies that ACES has the rights to do all of the things it normally does with such an article.

In connection with its publishing activities, it is the policy of ACES to own the copyrights in its technical publications, and to the contributions contained therein, in order to protect the interests of ACES, its authors and their employers, and at the same time to facilitate the appropriate re-use of this material by others.

The new United States copyright law requires that the transfer of copyrights in each contribution from the author to ACES be confirmed in writing. It is therefore necessary that you execute either Part A-Copyright Transfer Form or Part B-U.S. Government Employee Certification or Part C-Crown Copyright on this sheet and return it to the Managing Editor (or person who supplied this sheet) as promptly as possible.

CLEARANCE OF PAPERS

ACES must of necessity assume that materials presented at its meetings or submitted to its publications is properly available for general dissemination to the audiences these activities are organized to serve. It is the responsibility of the authors, not ACES, to determine whether disclosure of their material requires the prior consent of other parties and if so, to obtain it. Furthermore, ACES must assume that, if an author uses within his/her article previously published and/or copyrighted material that permission has been obtained for such use and that any required credit lines, copyright notices, etc. are duly noted.

AUTHOR/COMPANY RIGHTS

If you are employed and you prepared your paper as a part of your job, the rights to your paper initially rest with your employer. In that case, when you sign the copyright form, we assume you are authorized to do so by your employer and that your employer has consented to all of the terms and conditions of this form. If not, it should be signed by someone so authorized.

NOTE RE RETURNED RIGHTS: Just as ACES now requires a signed copyright transfer form in order to do “business as usual”, it is the intent of this form to return rights to the author and employer so that they too may do “business as usual”. If further clarification is required, please contact: The Managing Editor, R. W. Adler, Naval Postgraduate School, Code EC/AB, Monterey, CA, 93943, USA (408)656-2352.

Please note that, although authors are permitted to re-use all or portions of their ACES copyrighted material in other works, this does not include granting third party requests for reprinting, republishing, or other types of re-use.

JOINT AUTHORSHIP

For jointly authored papers, only one signature is required, but we assume all authors have been advised and have consented to the terms of this form.

U.S. GOVERNMENT EMPLOYEES

Authors who are U.S. Government employees are not required to sign the Copyright Transfer Form (Part A), but any co-authors outside the Government are.

Part B of the form is to be used instead of Part A only if all authors are U.S. Government employees and prepared the paper as part of their job.

NOTE RE GOVERNMENT CONTRACT WORK: Authors whose work was performed under a U.S. Government contract but who are not Government employees are required so sign Part A-Copyright Transfer Form. However, item 5 of the form returns reproduction rights to the U. S. Government when required, even though ACES copyright policy is in effect with respect to the reuse of material by the general public.

APPLIED COMPUTATIONAL ELECTROMAGNETICS SOCIETY JOURNAL
http://aces.ee.olemiss.edu

INFORMATION FOR AUTHORS

PUBLICATION CRITERIA

Each paper is required to manifest some relation to applied computational electromagnetics. **Papers may address general issues in applied computational electromagnetics, or they may focus on specific applications, techniques, codes, or computational issues.** While the following list is not exhaustive, each paper will generally relate to at least one of these areas:

1. **Code validation.** This is done using internal checks or experimental, analytical or other computational data. Measured data of potential utility to code validation efforts will also be considered for publication.

2. **Code performance analysis.** This usually involves identification of numerical accuracy or other limitations, solution convergence, numerical and physical modeling error, and parameter tradeoffs. However, it is also permissible to address issues such as ease-of-use, set-up time, run time, special outputs, or other special features.

3. **Computational studies of basic physics.** This involves using a code, algorithm, or computational technique to simulate reality in such a way that better, or new physical insight or understanding, is achieved.

4. **New computational techniques**, or new applications for existing computational techniques or codes.

5. **"Tricks of the trade"** in selecting and applying codes and techniques.

6. **New codes, algorithms, code enhancement, and code fixes.** This category is self-explanatory, but includes significant changes to existing codes, such as applicability extensions, algorithm optimization, problem correction, limitation removal, or other performance improvement. **Note: Code (or algorithm) capability descriptions are not acceptable, unless they contain sufficient technical material to justify consideration.**

7. **Code input/output issues.** This normally involves innovations in input (such as input geometry standardization, automatic mesh generation, or computer-aided design) or in output (whether it be tabular, graphical, statistical, Fourier-transformed, or otherwise signal-processed). Material dealing with input/output database management, output interpretation, or other input/output issues will also be considered for publication.

8. **Computer hardware issues.** This is the category for analysis of hardware capabilities and limitations of various types of electromagnetics computational requirements. Vector and parallel computational techniques and implementation are of particular interest.

Applications of interest include, but are not limited to, antennas (and their electromagnetic environments), networks, static fields, radar cross section, shielding, radiation hazards, biological effects, electromagnetic pulse (EMP), electromagnetic interference (EMI), electromagnetic compatibility (EMC), power transmission, charge transport, dielectric, magnetic and nonlinear materials, microwave components, MEMS technology, MMIC technology, remote sensing and geometrical and physical optics, radar and communications systems, fiber optics, plasmas, particle accelerators, generators and motors, electromagnetic wave propagation, non-destructive evaluation, eddy currents, and inverse scattering.

Techniques of interest include frequency-domain and time-domain techniques, integral equation and differential equation techniques, diffraction theories, physical optics, moment methods, finite differences and finite element techniques, modal expansions, perturbation methods, and hybrid methods. This list is not exhaustive.

A unique feature of the Journal is the publication of unsuccessful efforts in applied computational electromagnetics. Publication of such material provides a means to discuss problem areas in electromagnetic modeling. Material representing an unsuccessful application or negative results in computational electromgnetics will be considered for publication only if a reasonable expectation of success (and a reasonable effort) are reflected. Moreover, such material must represent a problem area of potential interest to the ACES membership.

Where possible and appropriate, authors are required to provide statements of quantitative accuracy for measured and/or computed data. This issue is discussed in "Accuracy & Publication: Requiring, quantitative accuracy statements to accompany data," by E. K. Miller, *ACES Newsletter*, Vol. 9, No. 3, pp. 23-29, 1994, ISBN 1056-9170.

EDITORIAL REVIEW

In order to ensure an appropriate level of quality control, papers are peer reviewed. They are reviewed both for technical correctness and for adherence to the listed guidelines regarding information content.

JOURNAL CAMERA-READY SUBMISSION DATES

March issue	deadline 8 January
July issue	deadline 20 May
November issue	deadline 20 September

Uploading an acceptable camera-ready article after the deadlines will result in a delay in publishing this article.

STYLE FOR CAMERA-READY COPY

The ACES Journal is flexible, within reason, in regard to style. However, certain requirements are in effect:

1. The paper title should NOT be placed on a separate page. The title, author(s), abstract, and (space permitting) beginning of the paper itself should all be on the first page. The title, author(s), and author affiliations should be centered (center-justified) on the first page.

2. An abstract is REQUIRED. The abstract should be a brief summary of the work described in the paper. It should state the computer codes, computational techniques, and applications discussed in the paper (as applicable) and should otherwise be usable by technical abstracting and indexing services.

3. Either British English or American English spellings may be used, provided that each word is spelled consistently throughout the paper.

4. Any commonly-accepted format for referencing is permitted, provided that internal consistency of format is maintained. As a guideline for authors who have no other preference, we recommend that references be given by author(s) name and year in the body of the paper (with alphabetical listing of all references at the end of the paper). Titles of Journals, monographs, and similar publications should be in italic font or should be underlined. Titles of papers or articles should be in quotation marks.

5. Internal consistency shall also be maintained for other elements of style, such as equation numbering. As a guideline for authors who have no other preference, we suggest that equation numbers be placed in parentheses at the right column margin.

6. The intent and meaning of all text must be clear. For authors who are NOT masters of the English language, the ACES Editorial Staff will provide assistance with grammar (subject to clarity of intent and meaning).

7. Unused space should be minimized. Sections and subsections should not normally begin on a new page.

PAPER FORMAT

The preferred format for initial submission and camera-ready manuscripts is 12 point Times Roman font, single line spacing and double column format, similar to that used here, with top, bottom, left, and right 1 inch margins. Manuscripts should be prepared on standard 8.5x11 inch paper.

Only camera-ready electronic files are accepted for publication. The term **"camera-ready" means that the material is neat, legible, and reproducible.** Full details can be found on ACES site, Journal section.

ACES reserves the right to edit any uploaded material, however, this is not generally done. It is the author(s) responsibility to provide acceptable camera-ready pdf files. Incompatible or incomplete pdf files will not be processed, and authors will be requested to re-upload a revised acceptable version.

SUBMITTAL PROCEDURE

All submissions should be uploaded to ACES server through ACES web site (http://aces.ee.olemiss.edu) by using the upload button, journal section. Only pdf files are accepted for submission. The file size should not be larger than 5MB, otherwise permission from the Editor-in-Chief should be obtained first. The Editor-in-Chief will acknowledge the electronic submission after the upload process is successfully completed.

COPYRIGHTS AND RELEASES

Each primary author must sign a copyright form and obtain a release from his/her organization vesting the copyright with ACES. Copyright forms are available at ACES, web site (http://aces.ee.olemiss.edu). To shorten the review process time, the executed copyright form should be forwarded to the Editor-in-Chief immediately after the completion of the upload (electronic submission) process. Both the author and his/her organization are allowed to use the copyrighted material freely for their own private purposes.

Permission is granted to quote short passages and reproduce figures and tables from and ACES Journal issue provided the source is cited. Copies of ACES Journal articles may be made in accordance with usage permitted by Sections 107 or 108 of the U.S. Copyright Law. This consent does not extend to other kinds of copying, such as for general distribution, for advertising or promotional purposes, for creating new collective works, or for resale. The reproduction of multiple copies and the use of articles or extracts for commercial purposes require the consent of the author and specific permission from ACES. Institutional members are allowed to copy any ACES Journal issue for their internal distribution only.

PUBLICATION CHARGES

ACES members are allowed 12 printed pages per paper without charge; non-members are allowed 8 printed pages per paper without charge. Mandatory page charges of $75 a page apply to all pages in excess of 12 for members or 8 for non-members. Voluntary page charges are requested for the free (12 or 8) pages, but are NOT mandatory or required for publication. A priority courtesy guideline, which favors members, applies to paper backlogs. Authors are entitled to 15 free reprints of their articles and must request these from the Managing Editor. Additional reprints are available to authors, and reprints available to non-authors, for a nominal fee.

ACES Journal is abstracted in INSPEC, in Engineering Index, DTIC, Science Citation Index Expanded, the Research Alert, and to Current Contents/Engineering, Computing & Technology.